From reionization
until now:
The history of the ionizing background

Phoebe R. Upton Sanderbeck

A dissertation
submitted in partial fulfillment of the
requirements for the degree of

Doctor of Philosophy

University of Washington

2018

Reading Committee:

Matthew McQuinn, Chair

Jessica Werk

Tom Quinn

Program Authorized to Offer Degree:
Astronomy

University of Washington

Abstract

From reionization until now: The history of the ionizing background

Phoebe R. Upton Sanderbeck

Chair of the Supervisory Committee:
Committee Chair Matthew McQuinn
Department of Astronomy

Ultraviolet light emitted by the first galaxies sparked the last major phase change of matter in the Universe. The bulk of gas in the Universe went from neutral to ionized, and as galaxies and quasars continued to replenish this light, the ionizing background settled in the space between these sources. This radiation background has the potential to impact structure in the Universe on larger scales than any other non-gravitational, astrophysical process. Because the ionizing background both affects and is sourced by galaxies and AGN, the properties of the ionizing background are tied to the history of cosmic star formation and supermassive black hole accretion.

Despite its astrophysical impact, the properties and evolution of the ionizing background are poorly constrained. This thesis focuses on three different aspects of the ionizing background: how the ionizing background molds the thermal history of the intergalactic medium, the nature of the extreme ultraviolet and soft X-ray background, and the impact of fluctuations of the ionizing background on the clustering of galaxies.

TABLE OF CONTENTS

LIST OF FIGURES

Figure Number Page

ACKNOWLEDGMENTS

This thesis is critically incomplete without acknowledgement of the many individuals who have impacted my trajectory these past six years.

Thank you to the former and current grad students of the UW Astronomy Department. You have been some of the dearest friends I have ever had the joy to know. The times spent singing karaoke, climbing on tables, hiking mountains, playing boardgames, laughing until we cry, and talking about life are some of the my favorite memories of the last six years. Special thank you to Kristen Garofali for being my partner-in-crime throughout the many milestones of graduate school.

Thank you to the other two members of the ”Dreamteam” of PAB B329, Diana Windemuth and Nell Byler. I always looked forward to going into the office when I had two of my dearest friends there. Thank you for always being there for me.

Thank you to the past and present postdocs in our group, Anson D’Aloisio and Vid Iršič. You have both improved my scientific process and challenged me to be better. More importantly, you have both been wonderful friends. I look forward to being career-long collaborators and lifelong friends.

Thank you to the faculty of the UW Astronomy Department. My experience in this department has been overwhelmingly positive. Thank you for the outstanding education and for setting the bar high. Special thanks to Julianne Dalcanton and Jessica Werk for the additional research support.

Thank you to my advisor, Matt McQuinn. I can’t begin to thank you for the guidance you’ve provided me these past four years. In addition to being one of the smartest and most successful people I know, you are a wonderful mentor and thoughtful teacher. Thank you for always caring about my success and helping me build the career I’ve always hoped for.

Finally, thank you to my family. Your love and support has meant everything.

DEDICATION

To my parents, Sean Upton and John Sanderbeck

Chapter 1

INTRODUCTION

"Physical sciences develop in seemingly chaotic ways, by paths that are at best dimly seen at the time, and leave traditions that may seems mysterious and even irrational. That is why the history of ideas is an important part of science, and particularly worth examining in cosmology, where the subject has evolved over several generations. The choice of where to begin has to be somewhat arbitrary, since any step in science builds on earlier ones." -P.J.E. Peebles

We live in a universe that has given us, as beings on Earth, a wealth of photons from the first 0.003 percent of its lifetime until now. As we look out to large distances, back in time, observational snapshots become more sporadic and leave many unanswered puzzles for astrophysicists and astronomers. Many of the largest questions in astrophysics rely on filling in these gaps in time and creating theoretical models for what we cannot learn directly from observations.

When considering baryonic (non-dark) matter in space, most will think first of luminous objects, such as galaxies, stars, and nebulae; or "terrestrial" objects, such as planets and moons. Surprisingly, the majority of baryonic matter in the Universe lies in the space between the dense and luminous galaxies. The story of how these galaxies formed is dependent on the evolution of the matter between galaxies and the light that permeates this space. Everything from star formation, supermassive blackhole (SMBH) formation, and cosmic structure in general is dependent on the evolution of the network of matter we call the intergalactic medium (IGM).

In the broadest terms, the goal of this thesis is to advance the theoretical framework of the interaction between light and matter between the luminous objects in the Universe. The following chapters describe theoretical models

1.1 Cosmological framework

1.1.1 ΛCDM

Much of the work presented in this thesis is based on an assumption of a ΛCDM cosmological model. ΛCDM has been the primary cosmological paradigm since the turn of the 21st century, after the measurement of the acceleration of the Universe's expansion in 1998. This acceleration fits into the Λ component of ΛCDM, where Λ refers to the cosmological constant, possibly from vacuum energy that dominates the energy density of the Universe at $z \lesssim 1$. ΛCDM has grown to encompass the idea of inflation, an epoch following the Big Bang when the Universe expanded exponentially due to a scalar field. Though the modern concept inflation was concocted as a mechanism to explain the absence of magnetic monopoles in the Universe, it was soon realized that it could also explain many other cosmological problems. For instance, it can explain why the Universe appears isotropic and homogenous at scales where there could not have been causal contact and why the Universe appears to be spatially flat. While neither dark energy nor inflation are the focus of the following chapters, their effects are not irrelevant to the physics we aim to constrain. For instance, whether or not inflation was sourced by a single scalar field or multiple fields determines whether primordial non-Gaussianity can be detected, a possibility we discuss in Chapter 4.

The most important part of this framework that is pertinent to the following work is the idea that baryonic matter traces an underlying network of dark matter which largely shapes the large-scale gravitational terrain. Since the mid-1980s, simulations and observations have tended to favor the cold dark matter (CDM) model where dark matter is collision-less, dissipation-less, and was not at all relativistic at the epoch of matter-radiation equality ($z \sim 3400$). Despite some discrepancies at small scales, the statistical properties of the large scale structure in the Universe can be reproduced remarkably well by CDM models. It is upon this dark matter network that the baryonic matter in the Universe is connected, through galaxies and the intergalactic medium.

1.1.2 Recombination

Around 400,000 years after the Big Bang ($z \sim 1100$), the radiation leftover from the mass annihilations of matter and antimatter decoupled from the Universe's baryonic matter and created the cosmic microwave background (CMB). This decoupling was the result of an adiabatically cooling universe causing the ionized gas particles, mostly free protons and electrons (though also a small fraction of nuclei from helium and other slightly heavier elements) to combine and form neutral atoms. This prevented the soon-to-be CMB photons from further interacting with and scattering off of free electrons. After this epoch, known as recombination, the photons of the CMB free-streamed through the universe, rarely interacting with matter, allowing us to observe light from a time before galaxies or stars. This light has now been exceedingly well studied and has been one of the best observational tools for cosmologists.

The large-scale structure we see around us in our ~ 14 Gyr-old Universe was seeded by small perturbations in the density field at very early times, seen as the small anisotropies in the CMB. These small gravitational instabilities grew and collapsed into small halos, which then collectively combined to form larger halos that eventually became the galaxies observed today.

1.1.3 Dark ages

The lack of observational information from the span of time between the formation of the cosmic microwave background and the first galaxies is known as the cosmic dark ages. This nomenclature can be taken literally at the point when CMB photons redshift out of the optical. During this time, the universe was mostly filled with neutral, primordial gas that was no longer coupled to CMB photons. As the Universe expanded during this time, the gas cooled adiabatically, ultimately leaving this gas at just tens of Kelvin just prior to the onset of the first galaxies. During this time, dark matter was collapsing into halos, and the gravitational landscape coaxed this gas into the clumpy and filamentary structure we now know as the intergalactic medium.

1.2 Reionization and beyond

1.2.1 The intergalactic medium

While the astrophysics involved in galaxy formation and evolution is stochastic and convoluted, for the most part, the physics governing the low-density IGM is simple and well-understood. Today, the IGM is ionized, diffuse, mostly primordial gas that traces the underlying dark matter structure. It is the reserve of baryonic matter from which galaxies get their gas, as well as a network that connects them. The matter in the low-density IGM interacts with itself and photons through atomic processes that are well-established and able to be modeled analytically. Note, the physics becomes more complicated at low redshifts ($z \lesssim 1$), when some of the gas becomes shock heated, or at high densities, where proximity to galaxies can influence the state of intergalactic gas.

Observing direct emissions from the $z < 6$ IGM is essentially impossible because its gas is too diffuse and ionized. Observations instead rely on background sources to illuminate the IGM via indirect spectroscopic observations (see Section 1.2.5), and eventually, the high redshift IGM ($z \gtrsim 6$) may be revealed through redshifted 21-cm observations (see Section 1.2.7). Because there is little ambiguity in the physics of the IGM, these observations constrain both cosmology and the properties of the sources that produce the ionizing background.

1.2.2 The first luminous sources

Before the first luminous sources began to form, the perturbations in the baryonic matter were nearly linear. Once nonlinear structure and the first stars and galaxies began to form, astrophysics became influential and the formation of complex structure became harder to describe with analytic models. Because significant populations of the first stars and galaxies are not directly accessible with the current generation of telescopes, such as the Hubble Space Telescope (HST), inferences about this time are often based on numerical studies, analytic estimates, and searches for remnants of this time in the Milky Way.

The first stars were formed at the densest peaks of the matter distribution where gas was able to cool efficiently and form molecular hydrogen. While the first stars formed likely around $z \sim 65$

(Naoz et al., 2006), the first galaxies did not become ubiquitous until several million years later. The first generation of stars (Population III stars) enriched the gas in protohalos, which then formed the first dwarf galaxies. The stars in these first dwarf galaxies were likely Population II stars, as the enhanced metal budget allowed lower mass and longer-living stars to form.

Telescopes that are coming online in the next decade will change the game for the study of early sources, specifically, the James Webb Space Telescope (JWST), which should produce observations of higher redshift galaxies that have yet to be detected. With JWST, and other upcoming telescopes, such as WFIRST and LSST, we are entering a new era of study of early source populations.

1.2.3 Reionization

As the first luminous sources turned on, the epoch of reionization began. These sources began to emit ultraviolet (UV) photons that started the process of reionizing the neutral hydrogen surrounding them. The earliest ionizing sources, likely isolated groups of Population III stars, were not effective in ionizing gas out to great distances from their host halos. It wasn't until a critical mass of ionizing sources, in the form of early galaxies, tuned on, that reionization started making headway.

The reionization of hydrogen in the IGM was the last major phase change of the Universe's matter. Prior to recombination and after Big Bang nucleosynthesis, the matter in the Universe was ionized; then recombination became the penultimate phase change. Finally, reionization occurred, though not instantaneously, as reionization was a patchy, extended process.

As galaxies became more common, growing ionization bubbles surrounding UV-emitting sources began to overlap and the IGM became a patchwork of different ionization states. Eventually, the ionized regions expanded to fill the IGM, and reionization completed, leaving the gas indefinitely ionized. Figure 1.2.3 shows an illustrative simulated example from Zaroubi (2013) of how reionization could have occurred, with the color scale representing the brightness temperature of neutral hydrogen (see Section 1.2.7), which scales with neutral hydrogen density.

Not only did reionization change the phase of IGM gas, but the temperature also underwent a significant shift. As the gas in the IGM was exposed to ionizing radiation in bulk, any excess energy held by a photon above the ionization potential was carried away by the newly freed electron, causing the formerly cold IGM to be heated to tens of thousands of degrees Kelvin. This changed the landscape for subsequent galaxy formation, as hotter gas was more pressure supported and less likely to be accreted onto a halo. This suppressed the formation of dwarf galaxies.

In recent years, there has been moderate debate about the nature of sources that drove reionization. While the majority of the literature regards early galaxies as the main perpetrators, e.g. Shapiro et al. 1994; Madau et al. 1999, the possibility of faint AGN being the fundamental contributors has been raised by some (Madau & Haardt, 2015). Because the quasar luminosity function drops off steeply at $z > 3$, an AGN-driven reionization would have to be sourced by faint AGN. The field's view of whether necessary populations of these objects at high redshifts exist is contentious, yet many follow up studies have been unable to reproduce quasar luminosity function with the same slope at high redshift. Certain measurements of the temperature of the IGM (see Section 1.2.6) also cast doubt on a quasar-driven reionization, as a signature temperature peak thought to be caused by the ubiquity of quasars can be found at $z \sim 3$ (D'Aloisio et al., 2017).

When and how reionization happened is still uncertain. The nature of the sources that drive reionization, when they turn on, and how photons escape into the IGM are unsettled problems. Despite these uncertainties, there is ample evidence that reionization was completed around $z \sim 6$ from the lack of total absorption at these redshifts of Lyman continuum photons in the spectra of quasars (Fan et al., 2006; Robertson et al., 2010; Komatsu et al., 2011; Planck Collaboration et al., 2015).

While the reionization of hydrogen[1] is marked by the first mass production of ionizing photons, likely by the earliest stars and galaxies, the increase of AGN at later times gave rise to a second reionization event, the reionization of the second electron of helium, henceforth known as He II reionization. The ionization potential of He II is four times that of hydrogen, and photons of this energy must come from highly energetic sources, most notably, quasars. Though galaxies do

---

[1] as well as the first electron of helium

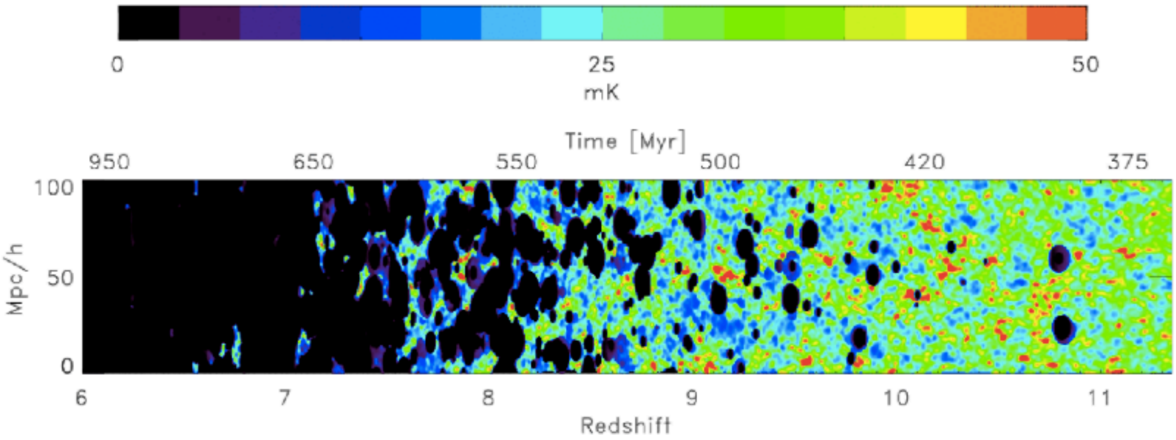

Figure 1.1: Theoretical reionization scenario shown with mock 21cm observations from Zaroubi (2013).

produce photons some at ~ 4 Ryd, it is likely they will be absorbed before reaching the IGM. The completion of He II reionization is believed to be at $z \approx 2.8$ based on the He II Lyman α forest (see Section 1.2.5) and IGM temperature (see Section 1.2.6).

1.2.4 The ionizing background

Following reionization, the IGM supported a background of ionizing photons that were continually replenished by galaxies and quasars. Thus through reionization, the ionizing background was born. The ionizing background has the potential to impact structure in the Universe on larger scales than any other non-gravitational, astrophysical process. After reionization, the photons of the ionizing background can travel considerable fractions of the Hubble distance, and, with their ability to disassemble neutral hydrogen and alter the cooling rates of ions, they can modulate the properties of extragalactic sources. Because the ionizing background both affects and is sourced by luminous structure in the universe, the properties of the ionizing background are inevitably tied to the history of cosmic star formation and supermassive black hole accretion.

Constraining the properties of the ionizing background relies on empirical understandings of its sources and sinks. The difficult nature of studying how many ionizing photons make it out of galaxies provokes much of the uncertainty in current models. Often, ionizing background models assume what fraction of ionizing photons make it out of the galaxy and into the IGM (colloquially known as the escape fraction) that is tuned to match photoionization rates derived from the Lyman α forest. Both empirically and theoretically, the escape fraction is poorly constrained. Empirically, observers have found wildly different escape fractions from galaxies at the same redshift. Observing the very low redshift escape fraction has been unsuccessful (no detections of Lyman continuum photons at $z \sim 0$) and at high redshift, the significantly higher neutral hydrogen opacity makes the escape fraction impossible to constrain. Theoretically, it is unclear how Lyman continuum photons from massive stars are attenuated by the ISM and other intervening gas. Until simulations can confidently capture the physics of the ISM and CGM, escape fractions derived from numerical simulations must be taken with skepticism.

Much of astrophysics and astronomy relies on ionizing background models. Such models are used in most all calculations of the ionization state of photoionized gas in the IGM and CGM, and they are used to set the ionization state of gas in cosmological simulations, which shapes the rate at which gas in simulations cools. Because they are so frequently used, previous models of the ionizing background, such as Haardt & Madau (1996), Haardt & Madau (2001), Faucher-Giguère et al. (2009), and Haardt & Madau (2012), are some of the most cited papers in astronomy. Figure 1.2.4 shows a frequently-used ionizing background model from Haardt & Madau (2012). The black curves show the models with contributions from both galaxies and quasars, while the red curves show "quasar-only" models. The two main spectral features in these models, more notable at higher redshifts, represent the absorption of He II at 4 Rydbergs and the absorption of H I at 1 Rydberg, respectively.

Though the cross section for ionization sharply decreases above the ionization potential, the ionizing background refers to the range of photon energies from the ultraviolet, through the X-ray. This means that empirical constraints of the ionizing background come from a patchwork of different observations from different types of telescopes. While ultraviolet and X-ray observations of ionizing sources are numerous, directly observing extragalactic sources in the extreme ultravi-

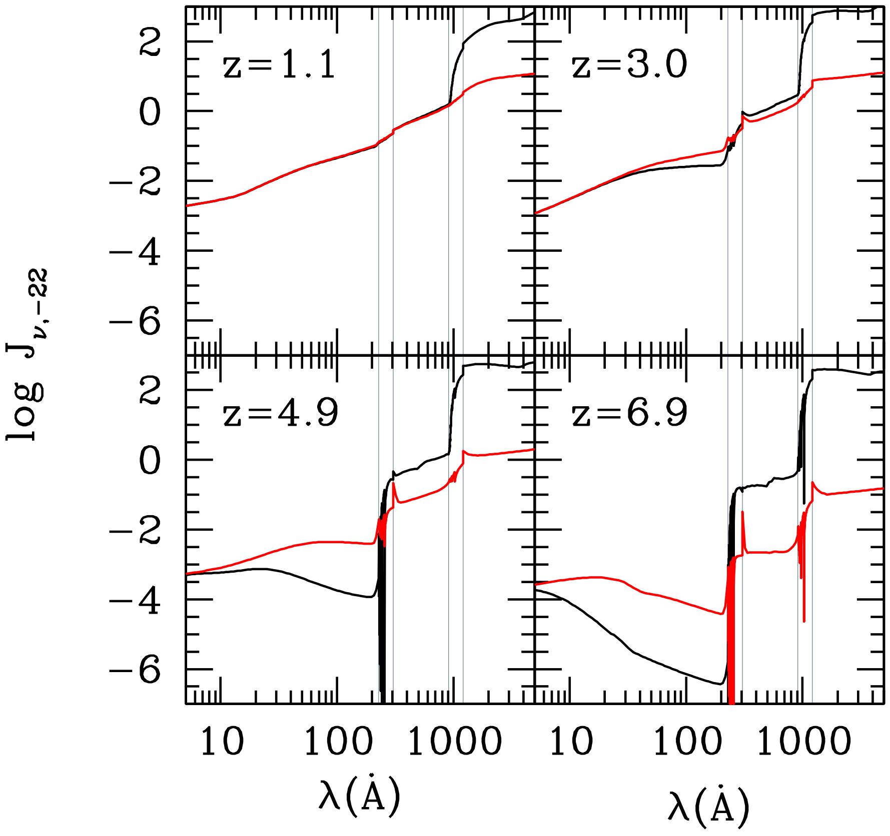

Figure 1.2: Ionizing background model of Haardt & Madau (2012) between redshifts of 1.1 and 6.9. The black curves are models with contributions from galaxies and quasars and the red curves are "quasar-only" models.

olet is nearly impossible. This is because the Galaxy efficiently absorbs extragalactic extreme UV before it reaches our solar neighborhood. The extreme UV is where many atomic transitions to ground Rydberg states of ions, and therefore cooling emissions, lie. Thus this piece of the ionizing background is crucial to the physics of the circumgalactic medium (see Section 1.2.9), the interface between galaxies and the IGM.

The lack of observations in the extreme UV impedes the ability to infer physical conditions of diffuse astrophysical gas from observable ionic lines because this part of the background often guides the important ionic ratios. Because of the uncertainty in this band, models of the ionizing background are limited by large error bars in the extreme UV until more detailed models of the sources that contribute, and a better understanding of the H I column density distribution. Chapter 3 presents models of the extreme UV background, their uncertainties, and the individual sources that contribute to this band.

1.2.5 The Lyman α forest

Because quasars are brighter than the most luminous of (non-active) galaxies, the detection of high-redshift quasars preceded those of other extragalactic sources. Once the first significantly redshifted quasars were detected, it was soon theorized that the imprint of the IGM may be found in the spectra of these distant sources as absorption lines from the residual neutral hydrogen that was pooled in the more dense intergalactic clouds or filaments (Gunn & Peterson, 1965; Scheuer, 1965). Due to the large cross-section of Lyman α absorption, only a minuscule amount of neutral hydrogen needs to be present to create this absorption feature. If too much neutral hydrogen were present (i.e. before reionization is completed), the line would saturate, producing what is known as a Gunn-Peterson trough that eliminates the detail found in the post-reionization forest. After reionization, the small fraction of neutral hydrogen remaining in the IGM can produce unsaturated absorption lines that encode information about the physical state of the intergalactic gas.

As a quasar's light travels through the IGM, light blueward of the rest-frame hydrogen Lyman α line (1216Å) redshifts into this resonance and will be absorbed if there is neutral hydrogen present. This creates a forest of absorption lines that mark the intergalactic structure intersecting the line-of-sight between the quasar and telescope. An example of this is shown in the bottom panel of Figure 1.2.5. The two panels in this figure illustrate the comparison between a quasar spectra with a conspicuous Lyman α forest (bottom panel) and one without (top panel).

Conditions for observing the Lyman α forest are ideal at redshifts between approximately $z \sim 2$ and $z \sim 5$, during the matter-dominated phase of the Universe. This represents a post-reionization era in which the light has traveled a sufficient distance to capture a vast swath of forest and has redshifted out of the UV and into the optical. Coincidentally, during this phase, the physical conditions of the IGM such as the ionization state and density are optimal for analyzing gas around the cosmic mean density.

When high-resolution echelle spectrographs on large telescopes (e.g., HIRES on the Keck, UVES on the Very Large Telescope) started collecting data more than two decades ago, the resolved Lyman α forest became one of the best observational tools to study the IGM. It was approximately within the same decade that high-resolution CDM simulations began to produce mock Lyman α forest that agreed remarkably well with the newly resolved observations, affirming models of large-scale structure and CDM.

Perhaps the most ubiquitously used Lyman α forest statistic is the power spectrum of the line-of-sight flux. At small scales, the power spectrum can constrain pressure smoothing of the gas from the thermal state of the IGM, and at the largest scales, the distribution of matter and the cosmology. The consistency of the Lyman α flux power spectrum with simulations using a ΛCDM framework have corroborated the basic models of the IGM as well as the concordance of cosmological parameters.

1.2.6 The thermal history of the IGM

The statistical properties of the Lyman α forest can reveal temperature information about intergalactic gas because the width of absorption lines are tied to thermal properties of the absorbers. The simplest way to untangle the temperature of the IGM from the Lyman α forest is to assume that the widths of the narrowest of absorption features are fully determined by thermal broadening. More statistically rigorous ways of disentangling the temperature involve using flux curvature

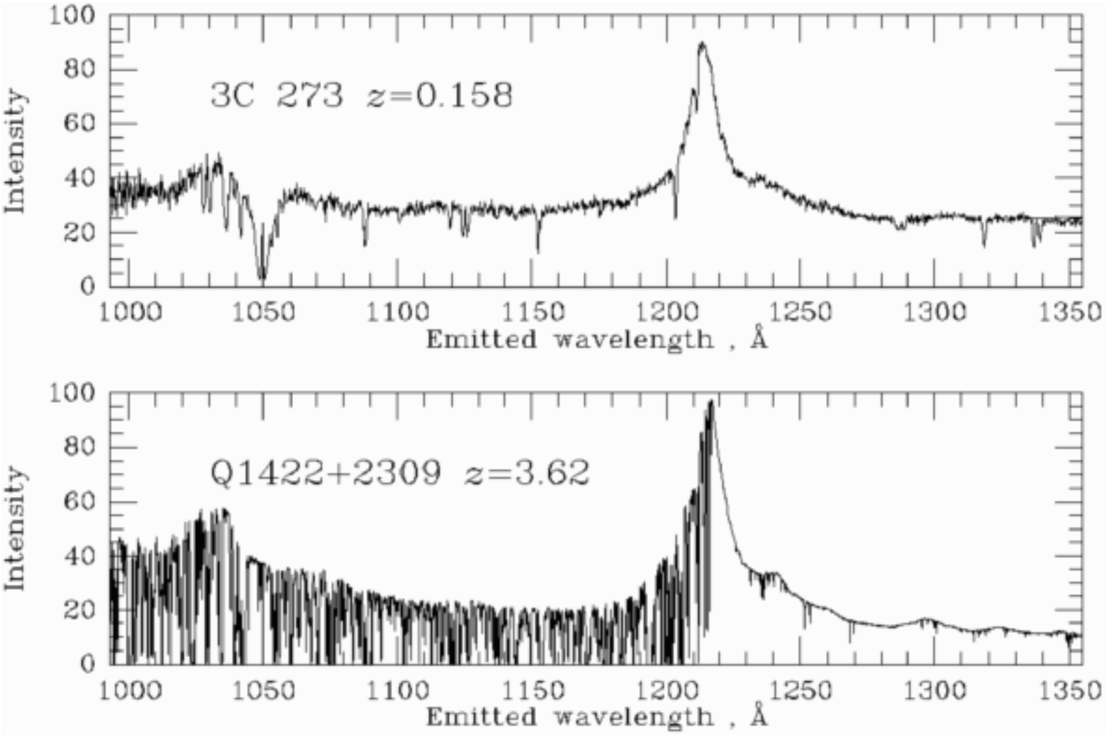

Figure 1.3: Top panel: $z \sim 0.2$ smooth quasar spectrum lacking apparent Lyman α forest absorption. Bottom panel: $z \sim 3.6$ quasar with an examplary Lyman α forest. Credit to Bill Keel.

statistics (Becker et al., 2011; Boera et al., 2014), the power spectrum (Hiss et al., 2017), and wavelet filters (Lidz et al., 2010; Lidz & Malloy, 2014).

Because reionization modulates the temperature of the IGM by tens of thousands of degrees, understanding the thermal history of the intergalactic medium can reveal the nature of reionization and properties of the sources that drove reionization. Chapter 2 explores the impact of different reionization scenarios on the thermal state of the IGM and uses temperature measurements to constrain the possible impact of previously neglected heating processes.

1.2.7 21cm observations of neutral hydrogen

When a neutral hydrogen atom undergoes a transition of its electron spin alignment, it emits a photon with a wavelength of $\lambda \sim 21$ cm. This is a forbidden transition with a transition rate of approximately 3×10^{-15} s^{-1}, hence a lifetime of on the order of $\sim 10^7$ years. While the abundance of neutral hydrogen before and during reionization causes the Lyman α forest to saturate, the rareness of the 21-cm transition prevents the line from a similar fate. While technically more difficult to observe than the Lyman α forest due to messy foregrounds and incredibly small signal, the 21-cm line is less restricted by redshift constraints and can illuminate the dark ages and reionization.

Though it has been realized for several decades that neutral hydrogen in the high-redshift Universe could be mapped via the redshifted 21-cm line, it hasn't been until the last couple decades that technology has allowed for the instrumentation to become a reality. In the coming decades, observations of neutral hydrogen via new low-frequency radio surveys will be crucial in furthering direct observations of the epoch of reionization and bringing in the first direct observations of the dark ages. Detangling the signals from these eras involves challenging foreground modeling and subtraction, so much effort is going into detailed modeling of these foregrounds with both theoretical and observational efforts.

The power spectrum of redshifted 21-cm emission from intensity mapping surveys will carry the imprint of both astrophysics and cosmology. Prior to reionization, this power spectrum should follow the dark matter power spectrum, but once reionization starts changing the ionization structure of hydrogen, the power spectrum will show the influence of the astrophysics of the ionizing background and ionizing sources. The details of reionization are found in the cross-correlation of galaxy clustering and ionized structure and auto-correlation of ionized structure (Morales & Wyithe, 2010) and the size of ionized regions shapes the 21cm power spectrum by washing out structure at small scales, and moving power to greater scales as ionized regions expand (Furlanetto et al., 2004). Despite the current challenges of 21cm science, the potential observations would open up many new avenues of high redshift astrophysics and answer many of the field's most studied questions, and hence, there is a great effort by the community to push forward.

1.2.8 Fluctuations in the ionizing background

Many ionizing background models rely on the assumption that the metagalactic ionizing background settles into a state of approximate spatial uniformity, as the mean free path of ionizing photons in the IGM greatly increasing after reionization such that every location in the IGM sees a large number of sources. While this is an adequate assumption for much of astrophysics, we are in an age of precision cosmology that relies on understanding the properties of large-scale structure to a sub-percent level. Effects of fluctuations in the ionizing background sourced by galaxies and quasars could have measurable effects on large scale structure (LSS) and modeling these effects could constrain the properties of the sources, such as the fraction of the ionizing background that owes to quasars versus galaxies.

Upcoming 21-cm intensity mapping surveys, Lyman α emitter surveys, and more generally, galaxy surveys may reveal signatures of background fluctuations. This, unless well-understood, could hinder the intended precision cosmology with some of these surveys. Chapter 4 presents calculations that aim to predict the effects that ionizing background fluctuations may have on these surveys.

1.2.9 The circumgalactic medium

The conception of the circumgalactic medium (CGM) was formulated over several decades, initially envisioned as a "galactic corona". In the middle of the 20th century, observations of hot stars in the outskirts of the galactic disk were found to have curious spectral signatures of sodium and calcium-II (Münch & Zirin, 1961) that indicated the presence of $\sim 10^6$ K gas at these extreme galactic latitudes (Spitzer, 1956). It was later found that many absorption features in quasar spectra had signatures of enriched CGM gas, such as damped Lyman α lines and metal lines such as C IV (Chen et al., 1998; Lanzetta et al., 1995).

It wasn't until the early 21st century, when larger surveys such as SDSS came online, that renewed interest in the CGM was born out of the realization that certain properties of galaxies could not be reconciled with the paradigm of ”closed-box” galaxy formation and evolution. There seemed to be a dearth of baryonic matter in galaxies compared to theoretical predictions, the metal budget in galaxies seemed to be lacking, and it was unclear how galaxies sustained or ceased their star formation. These issues all are linked to how galaxies get their gas, where nearby gas resides, how gas is recycled, and how gas is expelled. In other words, these are problems related to our understanding of the CGM.

Not only is the CGM the interface between galaxies and their source of baryonic matter, the CGM has a comparable amount of matter to the galaxy itself. The physics of the gas of the CGM is strikingly more complicated than that in the IGM, as it is multiphase and structurally diverse. The gas in the CGM is often categorized into cold, warm, and hot phases, with varying kinematics in each phase. Figure 1.2.9 shows a cartoon model of the CGM from Tumlinson et al. (2017), with a rudimentary representation of the main dynamic features. The physics of the inflows and outflows of the CGM is the key to understanding galaxy evolution, such as how star formation is regulated in galaxies and what makes a galaxy quiescent. Because we are not at a point where simulations can confidently capture the detailed structure of the CGM (and nor do we know exactly what this structure is), observations of the CGM are crucial for understanding galaxy evolution and for exposing the gaseous highway in and out of the galaxy.

Like the IGM, the CGM is observationally probed most effectively through quasar spectra. Absorption lines in the spectra of bright background objects are sensitive down to low column densities. When the sightline of a quasar intersects a galactic halo, a multitude of lines from metals and high column densities of hydrogen ($N_{\rm HI} \gtrsim 10^{15}$ cm^{-2}) will clue observers into the presence of

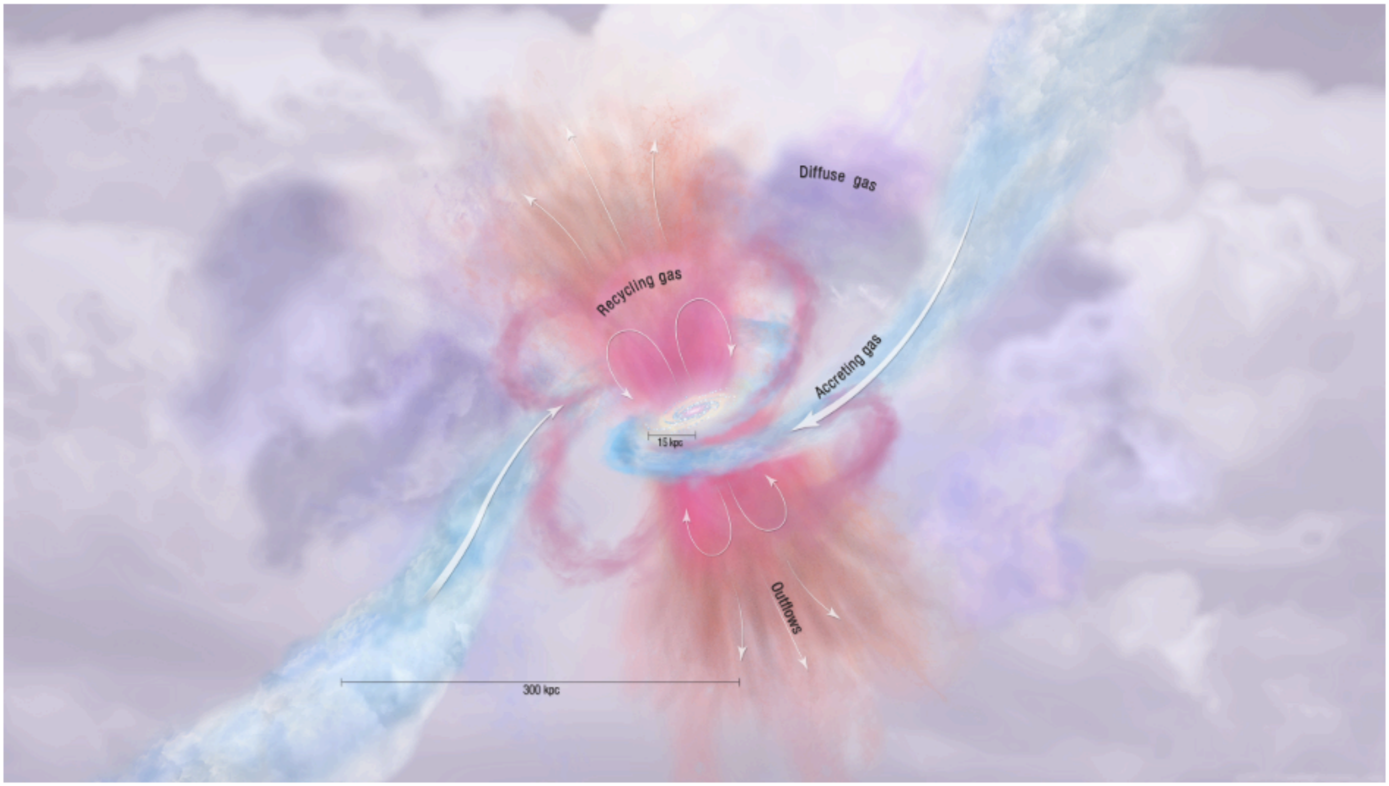

Figure 1.4: Cartoon model of the CGM from Tumlinson et al. (2017), which qualitatively illustrates the different gas kinematics.

CGM gas. Physical properties of the CGM are derived from ion lines that probe particular phases of gas dependent on the ionization potential. The energy of these ionization potentials classify these ions into low ($\lesssim 40$ eV), intermediate ($40 \lesssim E_{\rm ion} \lesssim 100$ eV), and high ions (> 100 eV), that probe cool/dense to hot/diffuse gas respectively. Despite the advantages of quasar absorption line studies, the CGM is also studied through emission line studies, stacking analyses, and host galaxy spectroscopy.

The photoionization state of the CGM is intimately tied to the details of the ionizing background. Specifically, the extreme UV and soft X-ray regime affect the cooling rates of circumgalactic gas. Chapter 3 discusses how the uncertainty in the ionizing background at energies where important CGM ionic transitions fall can affect the interpretation of physical properties of the

CGM.

1.2.10 Outline of the following chapters

Our understanding of how matter in the Universe evolves and forms structure is incomplete without comprehension of the physics of the the IGM, CGM, and the ionizing background. Importantly, the astrophysical processes of these three entities are intertwined and dependent on each other. The following chapters address many of the open questions surrounding the IGM; CGM; ionizing background and reionization; and by proxy, galaxy formation and evolution.

Specifically, this work aims to answer the following: How and when did reionization happen? Which sources contribute to the ionizing background? How does the ionizing background affect physical properties of the CGM? How might the ability to do precision cosmology with surveys be contaminated by fluctuations in this background?

Chapter 2 describes models of the thermal history of the IGM after reionization. Chapter 3 presents models of the extreme ultraviolet and soft X-ray bands and how these models relate to properties of the CGM. Chapter 4 investigates the effect of ionizing background fluctuations on the large-scale clustering of galaxies. Finally, Chapter 5 concludes with a summary of the results presented and a discussion of future work.

Chapter 2

THE THERMAL HISTORY OF THE INTERGALACTIC MEDIUM AFTER REIONIZATION

This article has been accepted for publication in Monthly Notices of the Royal Astronomical Society Published by Oxford University Press on behalf of the Royal Astronomical Society (Upton Sanderbeck et al., 2016).

Recent years have brought more precise temperature measurements of the low-density intergalactic medium (IGM). These new measurements constrain the processes that heated the IGM, such as the reionization of H I and of He II. We present a semi-analytical model for the thermal history of the IGM that follows the photoheating history of primordial gas. Our model adopts a multi-zone approach that, compared to previous models, more accurately captures the inhomogeneous heating and cooling of the IGM during patchy reionization. We compare our model with recent temperature measurements spanning $z = 1.6 - 4.8$, finding that these measurements are consistent with scenarios in which the He II was reionized at $z = 3 - 4$ by quasars. Significantly longer duration or higher redshift He II reionization scenarios are ruled out by the measurements. For hydrogen reionization, we find that only low redshift and high temperature scenarios are excluded. For example, a model in which the IGM was heated to $30,000$ K when an ionization front passed, and with hydrogen reionization occurring over $6 < z < 9$, is ruled out. Finally, we place constraints on how much heating could owe to TeV blazars, cosmic rays, and other nonstandard mechanisms. We find that by $z = 2$ a maximum of 1 eV of additional heat could be injected per baryon over standard photoheating-only models, with this limit becoming $\lesssim 0.5$ eV at $z > 3$.

2.1 Introduction

When the ultraviolet photons from the first galaxies reionized the neutral hydrogen in the Universe, a process that is thought to have occurred over $z \sim 6 - 12$ (Fan et al., 2006; Komatsu et al., 2011; Robertson et al., 2010; Planck Collaboration et al., 2015), the intergalactic medium (IGM) was significantly heated from likely hundreds of degrees to $\sim 10^4$ K by the excess energy above 1 Rydberg from each photoionization. After the reionization of hydrogen and the first electron of helium, the next and last heating event of unshocked gas is thought to have been the reionization of the second electron of helium, likely by quasars' ionizing emissions at $z \approx 3 - 4$ (Reimers et al., 1997; Theuns et al., 2002a; McQuinn et al., 2009). After each reionization event, the evolution of the IGM temperature is driven by photoionization heating of residual bound electrons, the expansion of the Universe, and by well-characterized cooling processes of primordial gas (Hui & Gnedin, 1997; Hui & Haiman, 2003). However, it is possible that other processes contributed to the thermal evolution of cosmic gas, such as heating from cosmic rays (Samui et al., 2005; Lacki, 2013), from the intergalactic absorption of blazar TeV photons (Chang et al., 2012; Puchwein et al., 2012), or from broadband intergalactic dust absorption (Inoue & Kamaya, 2008).

Hydrogen Lyα forest absorption in high-resolution, high signal-to-noise quasar spectra is the primary dataset used for measuring the temperature of the low-density IGM, having been used to place constraints over a broad range in redshift, $1.5 < z < 4.8$ (recently by Lidz et al. 2010; Becker et al. 2011; Boera et al. 2014). Temperature measurements from the Lyα forest are based on the Lyα absorption features of a colder IGM having sharper features than those of a warmer one; the spatial distribution of higher temperature gas is more extended because of higher pressures, and the absorption of hotter gas is additionally smoothed by enhanced thermal broadening. Many methods to estimate the temperature that exploit these effects have been devised, including directly fitting for the widths of Lyα forest absorption lines as a function of H I column (e.g., Schaye et al. 2000; Ricotti et al. 2000; McDonald et al. 2001; Bolton et al. 2014), measuring the exponential suppression that owes to temperature at high wavenumbers in the Lyα forest power spectrum (Zaldarriaga et al., 2001), and convolving Lyα forest spectra with wavelet (and wavelet-like) filters that return larger values for sharper features (Lidz et al., 2010; Becker et al., 2011; Theuns & Zaroubi, 2000; Theuns et al., 2002c; Zaldarriaga, 2002). Regardless of the temperature estimation method, analyses must mock observe Lyα forest spectra synthesized from cosmological hydrodynamic simulations to calibrate their temperature estimates.

There was a significant focus on measuring the IGM temperature from the Lyα forest around the the turn of the century (Schaye et al., 2000; Ricotti et al., 2000; McDonald et al., 2001). The main conclusion from these earlier measurements was that the temperature at $z \sim 3$ was too high for hydrogen reionization (and a contemporaneous full reionization of helium) to be the most recent heating event and likely implied either (1) He II reionization had occurred around $z \sim 3$ (Hui & Haiman, 2003) or (2) some non-standard heating process was operating (Samui et al., 2005). The measurements of Schaye et al. (2000) showed evidence for an increase and then decrease in temperature straddling $z \sim 3$, for which the simplest explanation is that it owes to He II reionization (Theuns et al., 2002a). However, this thermal bump was not obviously present in other contemporaneous measurements (Ricotti et al., 2000; McDonald et al., 2001; Zaldarriaga et al., 2001). In the last several years, there has been a renewed focus on temperature estimates. Of particular note, Becker et al. (2011) measured the thermal history over $2 < z < 4.8$ at a specific redshift-dependent density chosen to minimize errors, allowing for a higher precision temperature estimate. This measurement qualitatively agrees with the earlier result of Schaye et al. (2000) that showed evidence for He II reionization. The Becker et al. (2011) measurement has been complimented by a subsequent effort by Boera et al. (2014) extending temperature measurements down to $z = 1.5$.[1] The Becker et al. (2011) measurement has also been confirmed over $2 < z < 3.2$ using other techniques (Garzilli et al., 2012; Bolton et al., 2014). Furthermore, in addition to the measurements of temperature at a single density, the scaling of temperature with density has recently been constrained well at $z = 2.4$ (Rudie et al., 2012; Bolton et al., 2014), adding to previous less-certain estimates over a range of redshifts (Ricotti et al., 2000; McDonald et al., 2001; Schaye

---

[1] In addition, Bolton et al. (2012) measured the temperature in the proximity region of seven quasars at $5.8 < z < 6.4$. The special location of this measurement, likely a region where the hydrogen was reionized early on in the reionization process (Lidz et al., 2007) and where the He II was reionized by the quasar make this measurement more difficult to interpret, but see Bolton et al. (2012).

et al., 2000). Motivated by this recent spate of IGM temperature measurements, this study presents the most realistic models to date of the thermal history of the IGM in the standard scenario in which photoionization is the dominant energy source. A byproduct of these studies is bounds on other heating and cooling processes

This paper is organized as follows. Section 2.2 discusses the temperature measurements that we use to compare our models. Section 2.3 describes a model for the temperature evolution of the low-density intergalactic medium after hydrogen reionization. Section 2.4 compares this model with the highest redshift temperature measurements at $z \sim 4.5$ to constrain hydrogen reionization. Section 2.5 then discusses the thermal evolution at lower redshifts when the heating from He II reionization is likely to be important. We place constraints on non-standard heating processes in Section 2.6. All calculations assume a flat ΛCDM Universe with $h = 0.7$, $\Omega_m = 0.3$, $\Omega_b = 0.045$, and $Y_{\rm He} = 0.25$.

2.2 Temperature Measurements

We primarily compare our models with the temperature measurements of Becker et al. (2011), spanning $2.1 \leq z_{\rm em} \leq 4.8$ and of Boera et al. (2014), spanning $1.6 \leq z_{\rm em} \leq 2.8$. Like other Ly$\alpha$ forest temperature measurements, these studies used that the width of Lyα absorption features is sensitive to thermal and pressure broadening, with sharper absorption features arising from lower temperature gas. Specifically, Becker et al. (2011) and Boera et al. (2014) adopted the "curvature statistic," defined as:

$$\kappa \equiv \frac{F''}{[1 + (F')^2]^{3/2}}, \tag{2.1}$$

where F' and F'' represent the first and second derivatives of the flux with respect to the velocity along a sightline. Colder regions have higher $\langle |\kappa| \rangle$ than hotter ones. Like with the closely-related wavelet method (Theuns & Zaroubi, 2000; Lidz et al., 2010) as well as the power spectrum method (Zaldarriaga et al., 2001), the curvature method does not require fitting for individual absorption lines.

The Becker et al. (2011) and Boera et al. (2014) temperature measurements, featured in Fig-

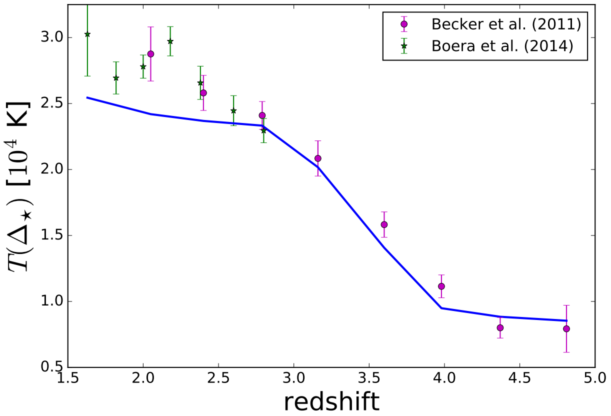

Figure 2.1: The IGM temperature at the critical densities, $\Delta_\star$, of Becker et al. (2011) and Boera et al. (2014). The solid curve corresponds to our model with He II reionization spanning $2.8 < z_{\rm rei} < 4$ (see § 2.5). The points with error bars are the measurements of Becker et al. (2011) and Boera et al. (2014). The corresponding densities of the Becker measurements are $\Delta_\star = 5.69, 4.39, 3.35, 2.62, 2.02, 1.64, 1.40, 1.23$ at $z = 2.05, 2.40, 2.79, 3.16, 3.60, 3.98, 4.37, 4.81$. The densities of the Boera measurements are $\Delta_\star = 5.13, 4.55, 4.11, 3.74, 3.39, 3.08, 2.84$ at $z = 1.63, 1.82, 2.00, 2.18, 2.38, 2.60, 2.80$.

ure 2.1, quote smaller errors than in previous IGM temperature studies. The increased precision arises from the realization in Becker et al. (2011) of a nearly one-to-one relationship between the mean curvature, $\langle|\kappa|\rangle$, and the temperature at a critical density of the Lyα forest, Δ_* (see Fig. 6 of Becker et al. 2011). (Throughout, we denote densities in units of the mean baryonic density as Δ.) This one-to-one relationship allows for scaling the measured curvature, $\langle|\kappa|\rangle$, into a measured $T(\Delta_\star)$. The physical reason for this correspondence is that the Lyα forest lines with optical depth $\tau_{\mathrm{Ly}\alpha} \sim 1$ are most sensitive to the IGM temperature, and the critical density that produces $\tau_{\mathrm{Ly}\alpha} \sim 1$ depends on redshift. Previous studies used other methods to constrain the temperature at $\Delta = 1$, T_0, and its power-law index, $\gamma - 1$, using the parameterization

$$T(\Delta) = T_0\, \Delta^{\gamma-1}. \tag{2.2}$$

This approach resulted in larger errors because the sensitivities of these methods are often greatest at densities significantly different from $\Delta = 1$. However, for this reason, the Becker et al. (2011) measurement does not directly constrain T_0, so a model for $\gamma - 1$ is needed in order to extrapolate from $T(\Delta_\star)$ to T_0.

Lastly, we note that the Becker et al. (2011) measurements agree with other attempts using different methodologies. At $z \sim 2.5$, the Becker et al. (2011) measurements are consistent with the results of Garzilli et al. (2012), which used wavelet plus the flux PDF methods, and Bolton et al. (2014), which used line-fitting methods. The Becker et al. (2011) measurements fall at just slightly lower temperatures than the earlier study of Schaye et al. (2000), but show similar trends. However, they appear to be discrepant with the measurements reported in Lidz et al. (2010). Figure 2.2 shows a compilation of T_0 and $\gamma - 1$ measurements, alongside our fiducial model with He II reionization (blue curve) and the same model but where the > 4 Ry background is set to zero such that the He II is never reionized (red curve). Both models are described in the ensuing sections. To make the comparison fair, for the Becker et al. (2011), Boera et al. (2014), and Lidz et al. (2010) data points in the top panel we take the $\gamma - 1$ values from our fiducial model. The actual measurements of $T(\Delta_*)$ from which the former two studies extrapolate, along with this theoretical model, are shown in Figure 2.1.[2]

2.3 Modeling the temperature of the IGM

2.3.1 The processes that affect the temperature

The temperature evolution of a Lagrangian fluid element is described by the following equation (Hui & Gnedin, 1997)

$$\frac{dT}{dt} = -2HT + \frac{2T}{3\,\Delta}\frac{d\Delta}{dt} - \frac{T}{n_{\rm tot}}\frac{dn_{\rm tot}}{dt} + \frac{2}{3k_B n_{\rm tot}}\frac{dQ}{dt}, \tag{2.3}$$

where H is the Hubble parameter and $n_{\rm tot}$ is the total number density of free "baryonic" particles (electrons and ions). Equation (2.3) does not include the shock heating from structure formation that heats some low density gas. We will comment on this omission later.

The first term on the right hand side of equation (2.3) accounts for adiabatic cooling due to the expansion of the Universe. At densities near the cosmic mean – densities where the temperature is measured – this expansion term tends to be the dominant coolant at $z < 6$, whereas at higher redshifts Compton cooling off of CMB photons becomes important for ionized gas.

The second term on the right hand side of equation (2.3) describes the adiabatic evolution due to collapsing overdensities and expanding voids. We model the density evolution of a gas element as a Zeldovich pancake (Zel'dovich, 1970) such that

$$\Delta(a) = \left[1 - \lambda G(a)\right]^{-1}, \tag{2.4}$$

where $G(a)$ is the growth factor (which over most redshifts considered scales as a) and λ is a parameter that is tuned to achieve a particular density at a given redshift. While much of the moderately overdense IGM that concerns us (i.e. $1 \leq \Delta \leq \Delta_*$) is well modeled by this restrictive form for $\Delta(a)$, we note that the actual thermal evolution is weakly sensitive to the history of $\Delta(a)$, as shown explicitly in McQuinn & Upton Sanderbeck (2015). We find that our results do not change if we assume different functional forms for $\Delta(a)$, such as that in spherical collapse (the approach in Furlanetto & Oh 2009).

---

[2] Lidz et al. (2010) also published estimates of T_0 that marginalize over $\gamma - 1$, resulting in larger error bars.

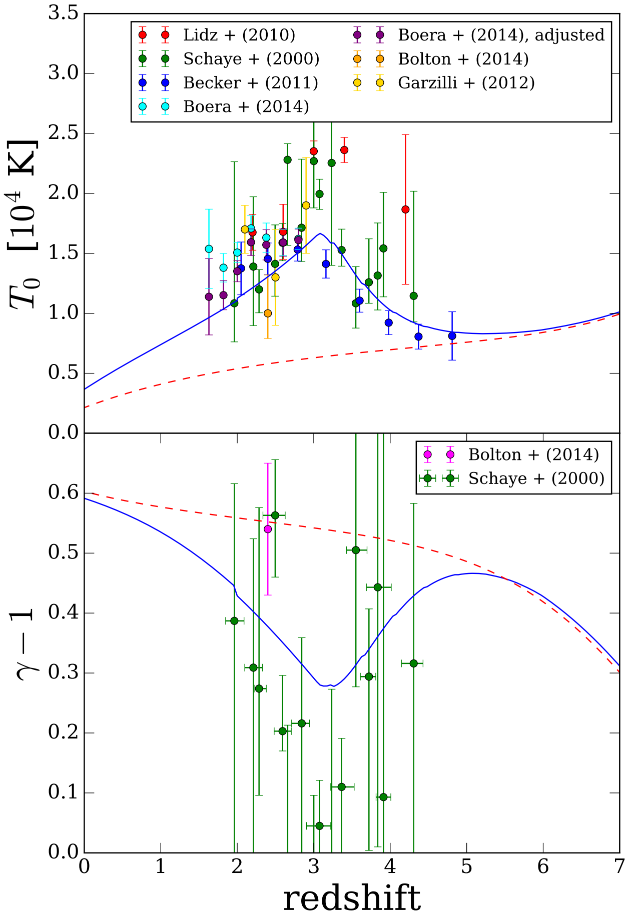

Figure 2.2: Measurements of T_0 (top panel) and $\gamma - 1$ (bottom panel) from Schaye et al. (2000), Lidz et al. (2010, fixing $\gamma - 1$ to that in our model), Garzilli et al. (2012), and Bolton et al. (2014). Also shown in the top panel is the Becker et al. (2011) and Boera et al. (2014) estimates using the $\gamma - 1$ of the blue model curve to extrapolate from their $\widehat{T}(\Delta_*)$ to T_0. The blue model curve is our fiducial heating history described in § 2.5 with $\alpha_{\rm QSO} = 1.7$ and $\alpha_{\rm bkgd} = 1.0$, whereas the red curve assumes the same parameters but sets the > 4 Ry background to zero such that the He II is never reionized.

The third term on the right hand side of equation (2.3) is relatively unimportant, accounting for the change in the number of particles in the thermal bath. This term only affects our calculations during He II reionization. We implement a 4% drop in the temperature when the He II becomes ionized to account for this term.

The fourth term on the right hand side of equation (2.3) is where all the details of our model lie, encoding all other heating and cooling processes. In standard models in which photoheating is the only heating process, the fourth term can be written as

$$\frac{dQ}{dt} = \overbrace{\sum_X \frac{dQ_{\text{photo},X}}{dt}}^{\text{heating}} + \overbrace{\frac{dQ_{\text{Compton}}}{dt} + \sum_i \sum_X R_{i,X} n_e n_X}^{\text{cooling}}, \tag{2.5}$$

where $dQ_{\text{photo},X}/dt$ is the photoheating rate of ion X, dQ_{Compton}/dt is the Compton cooling rate, and $R_{i,X}$ is the cooling rate coefficient for ion X and cooling mechanism i, including recombination cooling, free-free cooling, and collisional cooling. For the cooling terms, our calculations adopt the rate coefficients in the appendix of Hui & Gnedin (1997) as well as the free-free cooling rate of Rybicki & Lightman (1979). McQuinn & Upton Sanderbeck (2015) discusses the relative importance of these processes. For the photoheating term, more modeling is required.

Modeling photoheating

There are two regimes for the photoheating rate, dQ_{photo}/dt: (1) The photoheating when an ion is being reionized, and (2) the optically thin photoheating that an ion experiences thereafter. The latter post-reionization rate is given by

$$\frac{dQ_{\text{photo},X}}{dt} = n_X \int_{\nu_X}^{\infty} \frac{d\nu}{h\nu} 4\pi J_\nu \sigma_X(\nu) \times [h\nu - h\nu_X], \tag{2.6}$$

$$\approx \frac{h\,\nu_X}{\gamma_X - 1 + \alpha} \alpha_{A,X} n_{\tilde{X}} n_e, \tag{2.7}$$

where $\alpha_{A,X}$ is the CASE A recombination coefficient associated with the transition $X\text{I} \rightarrow X$, $X \in$ $\{$ H I , He I , He II$\}$ and $\tilde{X} \in \{$H, He$\}$, ν_X is the frequency associated with the ionizing potential of species X, $\sigma_X(\nu)$ is the photoionization cross section, and γ_X is the approximate power-law index of $\sigma_X(\nu)$ for which we take values of $\{2.8,\ 1.7,\ 2.8\}$ for {H I, He I, He II}. Equation (2.7) results from the approximation of photoionization equilibrium with an ionizing background that has a power-law specific intensity of the form $J_\nu \propto \nu^{-\alpha}$, where J_ν is the average specific intensity [erg s^{-1} Hz^{-1} sr^{-1} cm^{-2}].[3]

The heating during reionization depends on when reionization processes occurred. It is thought that the reionization of H I and He I (what we will refer to as "hydrogen reionization") was driven by POPII stars. Observations of the Lyα forest suggest that this process ended by $z \approx 6$ (Fan et al., 2006; McGreer et al., 2015), with measurements of the cosmic microwave background suggesting a mean redshift for this process of $z = 8.8^{+1.7}_{-1.4}$ (Planck Collaboration et al., 2015). He II is thought to have been reionized by quasars, with observations of the He II Lyman-α forest suggesting that this process completed around $z \approx 2.8$ (McQuinn, 2009; Worseck et al., 2011; Shull et al., 2010).[4] In the standard picture, the duration of the He II reionization process depended on the emissivity of quasars, which has been well measured $z \lesssim 3$ and the constraints are improving at higher redshifts (Hopkins et al., 2007; Willott et al., 2010; Fiore et al., 2012; McGreer et al., 2013). Models of He II reionization by quasars predict that He II reionization should span a significant time interval, at least $z = 3 - 4$ (Furlanetto & Oh, 2008; McQuinn et al., 2009; Compostella et al., 2013), although recent measurements of quasar abundances suggest that an earlier timeline may be possible (Giallongo et al., 2015; Madau & Haardt, 2015). We constrain the duration of He II reionization here using its effect on the temperature.

Hydrogen and helium reionization heat the IGM with a higher rate than the optically thin photoheating rate (eqn. 2.7; e.g. Abel & Haehnelt, 1999; Trac et al., 2008; McQuinn et al., 2009). The amount of heating from these processes has been quantified by previous numerical studies. McQuinn (2012) showed that the temperature after an HI ionization front passes is unlikely to be

---

[3] Equation (2.7) also ignores photoionizations into ionization state X. This approximation is very accurate. For example, take the case of $X =$He II. Once the He I is reionized, $x_{\rm HeI} \approx 10^{-5} x_{\rm HeII}$ assuming photoionization rates relevant for He I. Thus, He II – which exists in much higher fractions ($x_{\rm HeII} \sim 10^{-2}$) – is formed primarily by recombinations from HeIII and not by photoionizations of He I, as equation (2.7) assumes.

[4] POPII stars do not produce many photons that can doubly ionize the He II. Even if there existed a non-nuclear galactic source that did produce these photons, it is unlikely that they would escape the local interstellar medium.

larger than $30,000$ K, because of collisional cooling inside the ionization front, nor smaller than $20,000$ K, confirming the analytic arguments in Miralda-Escudé & Rees (1994) that it should fall around $20,000$ K. (The exact temperature depends on the spectrum of the sources and speed of the ionization fronts.) We use these bounds in our models of hydrogen reionization discussed in Section 2.4. In contrast, during He II reionization the heating is not localized just to the ionization front. Instead, much of the heating occurs from a nearly uniform hard, $\gtrsim 200$ eV, background that has a long mean free path to be absorbed (McQuinn et al., 2009). Another difference with H I reionization is that collisional cooling is not efficient in the He II ionization fronts such that the ionizing spectrum alone determines the amount of photoheating during He II reionization (McQuinn et al., 2009). We describe a physically motivated model for the photoheating during He II reionization in Section 2.5.

2.3.2 Comparing our models with the temperature measurements

This section describes in detail how we compare our model predictions with the Becker et al. (2011) and Boera et al. (2014) measurements. We warn the reader in advance that this section is the most technical in the paper. Readers not interested in how we infer the "observed" temperature from our models can skip to the next section.

The problem this section addresses is that our models predict a distribution of temperatures at every redshift and density rather than a single temperature. Thus, we must understand how to map our models to the effective temperature Becker et al. (2011) and Boera et al. (2014) measured. In addition, even for histories with a single temperature at a given Δ (as in our models that assume an instantaneous reionization), the measured temperature would differ from the actual temperature because the Becker et al. (2011) and Boera et al. (2014) measurement technique is calibrated for a specific thermal history.[5] Handling these effects in full rigor would require running simulations that mimic the inhomogeneous photoheating rates in our models, generating mock Ly α forest skewers

---

[5] The pressure smoothing of the gas affects the measured curvature, and pressure smoothing is sensitive to the temperature over the previous dynamical time. Indeed the curvature statistic is more affected by pressure broadening than other Lyα forest temperature diagnostics (Puchwein et al., 2015).

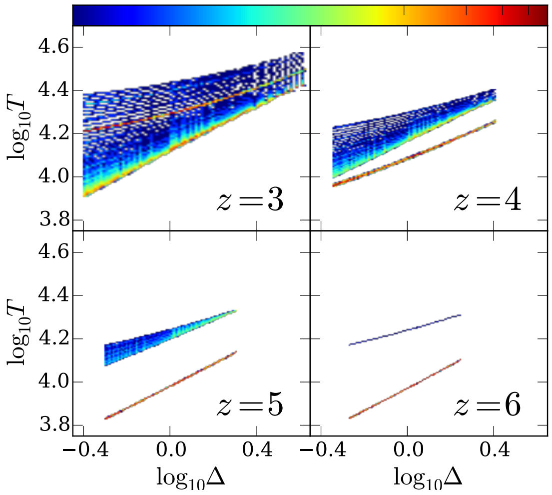

Figure 2.3: Predicted temperature distribution in a fiducial quasar reionization model described in § 2.5 that uses the Hopkins et al. (2007) emissivity history and that takes H I reionization to be instantaneous at $z = 9$. The colorbar denotes the logarithmic number of zones that fall in the pixel such that red areas have approximately two orders of magnitude times more points than dark blue. Initially almost all points fall on a single $T - \Delta$ relation. Gradually as He II reionization proceeds a distribution of temperatures develops. This development is similar to that seen in radiative transfer simulations of He II reionization (McQuinn et al., 2009). Section 2.3.2 motivates why a simple average of $T(\Delta)$ yields the effective temperature that has been measured.

from the simulations, applying the curvature statistic to them, and comparing directly to the Becker et al. (2011) and Boera et al. (2014) curvature measurement. Fortunately, running a simulation for every model that we consider is unnecessary; we show here that the Becker et al. (2011) and Boera et al. (2014) $T(\Delta_\star)$ estimates essentially measure the average $T(\Delta_\star)$ of our models.

Let us first focus on the effective temperature that the curvature statistic would measure in our models, ignoring pressure smoothing for the time being. Generally the spatial temperature fluctuations in our models have $\delta T/T < 1$, with the size of fluctuations being smaller with increasing Δ. Figure 2.3 shows the temperature-density distribution in the fiducial model described in § 2.5. The dispersion in temperature at fixed density owes to different regions being reionized at different times. Even though the dispersion looks quite large, the fractional standard deviation at Δ_*

in this model are only $\{0.14, 0.13, 0.14, 0.25\}$ at $z = \{3,\ 4,\ 5,\ 6\}$. The smallness of the standard deviation means that any weighted average of the temperature would differ from the actual mean temperature by a relatively small factor of $\sim T\langle(\delta T/T)^2\rangle$. Indeed, as an example we find that if we take the mean $T(\Delta)$ or the exponentiated mean of $\log T(\Delta)$ in our fiducial model at $z = 3$, the two values agree with astonishing accuracy, to 0.7%. Thus, the effective temperature that Lyα forest temperature measurements infer likely can be approximated by the average temperature.

To be more quantitative, we took the relation between $\langle|\kappa|\rangle$ and $T(\Delta_\star)$ measured from a suite of simulations in Becker et al. (2011). We then calculated

$$\overline{\langle|\kappa|\rangle} = \int dT_{\Delta_*} P(T_{\Delta_*})\, \langle|\kappa|\rangle(T_{\Delta_*}), \tag{2.8}$$

where $P(T_{\Delta_*})$ is the probability distribution of $T_{\Delta_*} \equiv T(\Delta_\star)$ and $\langle|\kappa|\rangle(T_{\Delta_*})$ is the mean curvature in a region with temperature T_{Δ_*}. Thus, $\overline{\langle|\kappa|\rangle}$ is the temperature-averaged curvature the Becker et al. (2011) method would infer from our models.[6] Then, we used the Becker et al. (2011) relation between $\langle|\kappa|\rangle$ and $T(\Delta_\star)$ to project $\overline{\langle|\kappa|\rangle}$ back to $T(\Delta_\star)$. Remarkably, we find that this agrees with the average of $T(\Delta_\star)$ to better than 1% at $z \sim 3$ (when the temperature fluctuations are largest) in our fiducial model. Thus, the curvature measurements constrain the average of $T(\Delta_\star)$ in our models.

Now let us focus on how to correct the temperature measurements to account for the pressure smoothing (also known as "Jeans smoothing") in our models. The biases from not having the correct pressure smoothing are most significant when the IGM is heated over a time interval much less than the free-fall timescale ($\ll H^{-1}\Delta_\star^{-1/2}$), the timescale for a sound wave to travel the Jeans' scale (the relaxation time), such as from a short He II reionization. The effect of pressure smoothing on $\langle|\kappa|\rangle$ was investigated in Becker et al. (2011). Becker et al. (2011) calibrated the relation between $T(\Delta_\star) - \langle|\kappa|\rangle$ using a suite of simulations that had relatively constant $T(\Delta_\star)$ with time, much different than the thermal histories in our models. To investigate the potential bias from these rather artificial temperature histories, Becker et al. (2011) ran two simulations where global

---

[6] This assumes that the temperature fluctuations we are modeling are coherent over much larger scales than the widths of lines in the forest.

heating was injected in a manner that emulates the heating from He II reionization (one where He II reionization spanned $\Delta z \approx 0.5$ and another with $\Delta z \approx 1$). Then, Becker et al. (2011) compared the estimated temperature from applying the $\langle|\kappa|\rangle$ estimate and then their $T(\Delta_\star) - \langle|\kappa|\rangle$ relation to the actual temperature in the simulation. They found that this resulted in a moderate bias, that when projected to $\Delta = 0$ was $\Delta T < 3000$ K, peaking near the end of He II reionization, with a smaller bias at other redshifts (see Appendix A).

Because our models have a similar duration to the He II reionization simulatations in Becker et al. (2011, Appendix A compares these histories), we correct the temperature values measured in Becker et al. (2011), $\widehat{T}(\Delta_\star)$. We multiply $\widehat{T}(\Delta_\star)$ by the amount of bias due to "Jeans smoothing" that they measure, ΔT, by the ratio of the temperature in our fiducial model, $T_{\rm fid}$, to their T15slow simulation with He II reionization, $T_{\rm T15slow}$ (because the Becker et al. 2011 simulations are at a bit higher temperatures). Namely, we correct the temperature measurements using

$$\widehat{T}(\Delta_\star)_{\rm corrected} = \widehat{T}(\Delta_\star) + \Delta T(z)\frac{T_{\rm fid}(\Delta_\star)}{T_{\rm T15slow}(\Delta_\star)}. \tag{2.9}$$

We use the T15slow He II reionization simulation of Becker et al. (2011) because it falls closest to our reionization histories (as shown in Appendix A). If we had instead used T15fast (which is shorter than in all of our models) the $\widehat{T}(\Delta_\star)_{\rm corrected}$ increase by a maximum of ≈ 2500 K, with this bias peaking at $z = 3.2$. In addition, because the Boera et al. (2014) measurement focuses on $z < 2.8$, after He II reionization in our models, the pressure smoothing correction is smaller: ≈ 1500 K at $z = 2.8$ and decreasing to < 100 K by $z = 2.0$.

Since we find that comparing the average temperature is accurate at the percent level and our pressure smoothing corrections are at most a few thousand Kelvin, our approximate way of correcting for these effects should be accurate to much better than the size of these corrections, more than sufficient for our purposes. The smallness of these corrections also justifies ignoring the coupling of these two effects. Furthermore, T_0 – the temperature at mean density – is also a more intuitive quantity than $T(\Delta_\star)$. To calculate T_0, we use the γ in our models to extrapolate both the measurements and the model to $\Delta = 0$. We fit for γ using the mean temperature and density at each redshift. This maintains the fractional difference between the measurements and model, and we find that in all of our plots it matters little which model we assume (and so we generally take the fiducial set of parameters). The model would matter if we considered models with and without a late He II reionization in the same plot, but this is never the case.

2.4 Temperature before He II reionization

Our model of the temperature of the IGM begins at the epoch of hydrogen reionization when the IGM was likely heated to $20,000 - 30,000$ K as an ionization front passed. Before He II was reionized and in the simplistic limit of an instantaneous H I (and He I) reionization, the uncertainties in the temperature can be parametrized by three numbers: the spectral index of the post-reionization ionizing background ($\alpha_{\rm bk}$), the final temperature of the IGM after hydrogen reionization ($T_{\rm rei}$), and the redshift of instantaneous hydrogen reionization ($z_{\rm rei}$). In this section, we first explore these dependencies and then turn to a more realistic model for an extended and patchy hydrogen reionization.

The top panel in Figure 2.4 shows the effect on the temperature history of the spectral index of the post-reionization ionizing background, $\alpha_{\rm bk}$, which affects the equilibrium photoheating rate after reionization. Ignoring ionizing recombination radiation, this spectral index is set by the intrinsic spectral index of the sources, α_s, and the logarithmic slope of the column-density distribution of intergalactic hydrogen absorbers, β, via the formula $\alpha_{\rm bk} \approx \alpha_s + 3(\beta - 1)$ (valid at $z \gtrsim 3$ when $\lambda_{\rm MFP,HI} \ll cH^{-1}$, where $\lambda_{\rm MFP,HI}$ is the physical mean free path of 1 Ry photons). The spectral index, α_s, is measured to be approximately 1.5 ± 0.2 if quasars dominate the ionizing background (Telfer et al., 2002; Shull et al., 2012; Lusso et al., 2015), and between 0 and 1.5 at ~ 1 Ry if it is stars (Faucher-Giguère et al., 2009; Leitherer et al., 1999; Conroy & Gunn, 2010; Bruzual & Charlot, 2003). Haardt & Madau (2012) shows a stellar population synthesis spectrum (Figure 15) where an effective slope of approximately $\alpha_s = 0.5$ appears most compatible with the population synthesis models over 1-4 Ry. In addition, $\alpha_s = 1$ was assumed in the UV background model of Faucher-Giguère et al. (2009) based on population synthesis models. However, this slope is likely hardened by things like stellar binarity (Stanway et al., 2016) and the inevitably frequency-dependent escape fraction of ionizing photons. The value of β is measured to be approximately

1.3 ± 0.2 (Songaila & Cowie, 2010), although it varies over the range of interest from steeper to flatter values (Prochaska et al., 2010; Zheng & Miralda-Escudé, 2002). In addition, direct recombination to the ground state can soften the effective spectral index that appears in the photoheating rate by ≈ 1 unit (Faucher-Giguère et al., 2009). Motivated by these values, we consider the range of $-0.5 \leq \alpha_{\rm bk} \leq 1.5$. The top panel in Figure 2.4 shows that $T(z)$ varies only by as much as $\Delta T \approx 2000$ K when we vary $\alpha_{\rm bk}$ over this large range. The insensitivity of T_0 to $\alpha_{\rm bk}$ arises because the energy per optically thin photoionization is approximately proportional to $(2 + \alpha_{\rm bk})^{-1}$, so that $-0.5 \leq \alpha_{\rm bk} \leq 1.5$ results in a factor of 2.3 variation in the photoheating rate, and at a maximum the temperature depends on the photoheating rate to the 0.6 power (McQuinn & Upton Sanderbeck, 2015).

The middle panel in Figure 2.4 investigates how the timing of hydrogen reionization affects $T_0(z)$. The three thin curves assume, simplistically, that hydrogen reionization occurred instantaneously at $z_{\rm rei} = 6, 8,$ and 9, heating the IGM to 2×10^4 K. Due to Compton cooling, the temperature of these curves decreases quickly after reionization, erasing all memory of when reionization occurred by $z \sim 4$ for the cases with $z_{\rm rei} \geq 8$. Only the $z_{\rm rei} = 6$ curve results in a significantly different prediction for T_0 at $z = 4.8$ than the highest-redshift Becker et al. 2011 measurement. (We note that $\Delta_* \approx 1.2$ for the $z = 4.8$ Becker et al. (2011) estimate and so there is little extrapolation necessary to T_0.)

The bottom panel in Figure 2.4 shows temperature histories with different initial temperatures after H I reionization, $T_{\rm rei}$. The IGM temperatures reached during reionization depend on the spectra of the sources as well as the speeds of the ionization fronts. These temperatures are likely bracketed by $18,000$ and $25,000$ K (Miralda-Escudé & Rees, 1994; McQuinn, 2012). One-dimensional radiative transfer calculations yield minimum temperatures of $\approx 18,000$ K for models in which the sources are much softer than is expected from stellar population synthesis models (McQuinn, 2012). On the other hand, radiative cooling within the ionization front becomes very efficient at temperatures $\gtrsim 25,000$ K, making it difficult to achieve temperatures much higher than this. However, for illustrative purposes we explore a broader range of temperatures in Figure 2.4, $T_{\rm rei} = 10,000 - 30,000$ K. While unrealistic, the $10,000$ K case is similar to the temperature achieved in simulations that use optically thin photoheating rates. The curves show the case of an instantaneous reionization at $z_{\rm rei} = 9$.

The curves in Figure 2.5 model the more realistic case of an extended hydrogen reionization process. To create these extended histories, we average a series of instantaneous reionization calculations at different times in different locations with reionization spanning $6 < z < 9$, $8 < z < 11$, and $6 < z < 13$. Indeed, averaging together $T(\Delta)$ from a series of instantaneous reionization calculations largely approximates how reionization is thought to have occurred; ionization fronts sweep over the Universe, ionizing and heating up different regions at different times. Afterwards, an ionized region cools via the well known physics described previously. To generate the measured $T(\Delta)$, we then average the temperature of these different histories for a given global reionization history, an approach justified in Section 2.3.2.

The top panel of Figure 2.5 shows models with post-reionization temperatures of $20,000$ K and reionization durations of $6 < z_{\rm rei} < 8$, $6 < z_{\rm rei} < 9$, and $8 < z_{\rm rei} < 11$, where the H II fraction evolves as a linear function of redshift with $x_{\rm HII} = 0$ at $z = z_{\rm rei}^{\rm max}$ and $x_{\rm HII} = 1$ at $z = z_{\rm rei}^{\rm min}$. This is a multi-phase model. The instantaneous heating is associated with ionization, so the fraction that is heated follows the ionized fraction. We also include a reionization scenario from Robertson et al. (2015) that spans $6 < z_{\rm rei} < 12$. We find that a reionization scenario ending at $z = 6$, with even a modest duration of $\Delta z = 3$, is consistent with the measurements. However, these late-ending reionization models become inconsistent with the measurements when the duration is shorter than $\Delta z \approx 2$. The bottom panel shows models with different temperatures after reionization. The dashed curves both span $6 < z_{\rm rei} < 9$, but have $T_{\rm rei} = 10,000$ and $30,000$ K, respectively. The solid curve shows a reionization scenario from D'Aloisio et al. (2015) that spans $6 < z_{\rm rei} < 13$, with $T_{\rm rei} = 30,000$ K. This model was found to generate the opacity fluctuations seen in the $z \sim 5.5$ Lyα forest (Becker et al., 2015). Though the resulting T_0 is dependent on the shape of the ionization history, in general, as long as reionization is extended, with $\Delta z \gtrsim 5$, $T_{\rm rei} = 30,000$ K is fully consistent with the Becker et al. (2011) temperature measurements at $z = 4.8$ and $T_{\rm rei} = 20,000$ K is consistent for any history with $\Delta z \gtrsim 3$.

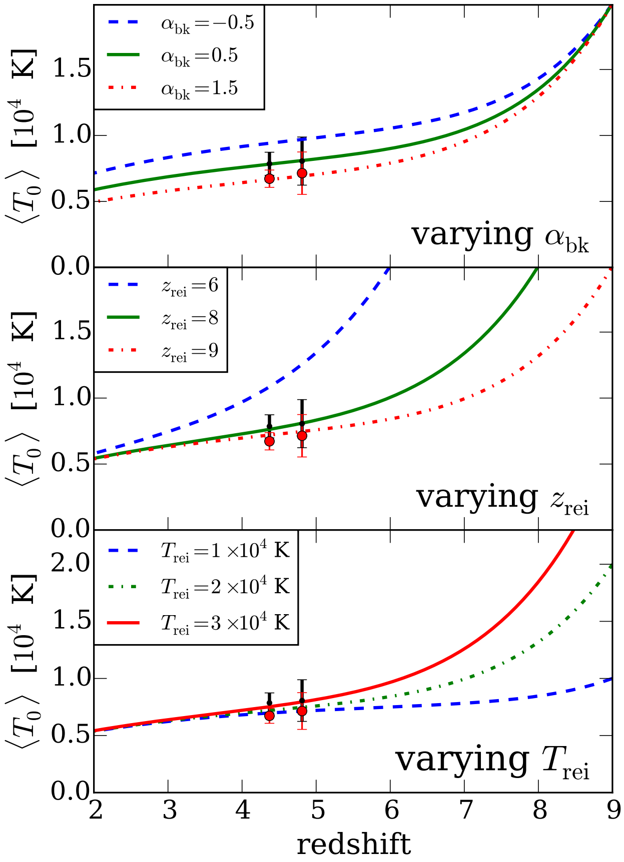

Figure 2.4: Average temperature of the IGM at the cosmic mean density in models that omit the photoheating from He II reionization and use $\alpha_{\rm bk} = 1$, $T_{\rm rei} = 20,000$ K, and $z_{\rm rei} = 9$, unless stated otherwise. *Top panel:* Models that vary the spectral index of the ionizing background over the range of $-0.5 < \alpha_{\rm bk} < 1.5$. *Middle panel:* Models that vary the redshift of instantaneous H I reionization. *Bottom panel:* Models that vary the final temperature after hydrogen reionization. The points with error bars are the two highest redshift temperature estimates of Becker et al. (2011). The red points have been corrected for pressure smoothing and the black points are uncorrected.

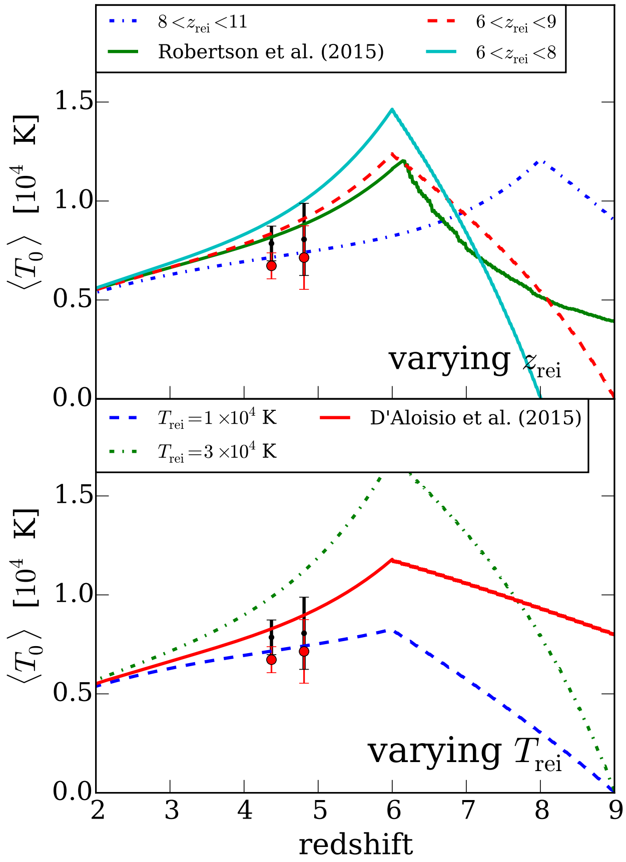

Figure 2.5: Average temperature of the IGM at the cosmic mean density in our models that use $\alpha_{\rm bk} = 1$ and omit the photoheating from He II reionization. *Top panel:* Models that vary the redshifts and durations of H I reionization with $T_{\rm rei} = 20,000$ K. The durations correspond to $6 < z_{\rm rei} < 8$, $6 < z_{\rm rei} < 9$, $8 < z_{\rm rei} < 11$, as well as the synthesis ionization history of Robertson et al. (2015). *Bottom panel:* Models that vary the final temperature after hydrogen reionization. We show two cases that have linear histories with $6 < z_{\rm rei} < 9$ and that vary the temperature after reionization between $T_{\rm rei} = 10,000$ K and $T_{\rm rei} = 30,000$ K. We also show a model with the ionization history from D'Aloisio et al. (2015, $6 < z_{\rm rei} < 13$ and $T_{\rm rei} = 30,000$ K). The points with error bars are the two highest redshift temperature estimates of Becker et al. (2011). The red points have been corrected for pressure smoothing and the black points are uncorrected.

2.5 Temperature evolution during He II *reionization*

Quasars are likely responsible for the reionization of helium, with the duration of this process shaped by their emissivity history. Indeed, the known population of quasars produce roughly the correct number of He II ionizing photons to reionize the Universe at $z \sim 3$ (Furlanetto, 2009), an epoch when observations of the He II Lyα forest strongly suggest that He II reionization was ending (McQuinn, 2009; Worseck et al., 2011; Shull et al., 2010). In addition, investigations into other sources of He II ionizing photons have found that they are unlikely to be sufficient (Furlanetto 2009, although see Miniati et al. 2004). The combinations of quasars having rather hard spectra and the potentially long mean free path of He II ionizing photons ($\lambda_{\rm MFP,HeII}$), with

$$\lambda_{\rm MFP,HeII} \approx 5\,\bar{x}_{\rm HeII}^{-1} \left(\frac{E_\gamma}{100{\rm eV}}\right)^3 \left(\frac{1+z}{4}\right)^{-2} {\rm comoving\ Mpc}, \tag{2.10}$$

where E_γ is the photon energy, results in a different structure for the photoheating that occurs during He II reionization compared to hydrogen reionization (McQuinn et al., 2009).

We model the photoheating during He II reionization with a multi-zone model that approximates the heating process found in detailed simulations (McQuinn et al., 2009). First, the lower energy photons with shorter $\lambda_{\rm MFP,HeII}$ are assumed to be consumed in producing a He III bubble around quasars, instantaneous heating the ionized gas by, on average,

$$\Delta Q_X^{\rm inst} = n_X \left(\int_{h\nu_X}^{E_{\rm max}} dE \frac{J_E}{E}\right)^{-1} \int_{h\nu_X}^{E_{\rm max}} dE (E - h\nu_X) \frac{J_E}{E}, \tag{2.11}$$

where X is the relevant species, $J_E \propto E^{-\alpha}$ is the average specific intensity that ionized the gas, $h\nu_X$ is the ionization potential of the ion (54.4 eV for He II), and $E_{\rm max}$ is the maximum energy photon that is typically absorbed in the process of making the He III bubble (i.e. $\lambda_{\rm MFP}$ less than the bubble size). Equation (2.11) makes the approximation that all photons between $h\nu_X$ and $E_{\rm max}$ are absorbed within the bubble, an approximation motivated by how strongly $\lambda_{\rm MFP}$ depends on E_γ. The gas temperature then increases by $\Delta T_{\rm inst}$ where $3/2 k_b n_{\rm tot} \Delta T_{\rm inst} = \Delta Q_{\rm inst}$ once the He III ionization front passes. For our fiducial value of $E_{\rm max}$, $\Delta T_{\rm inst}$ is approximately $\{8100, 8500, 8900\}$ K at $\alpha_{\rm QSO} = \{1.7, 1.5, 1.3\}$. Because these fronts take time to fill intergalactic space, different gas parcels experience this temperature increase at different times set by the duration of He II reionization.

The $E_\gamma > E_{\rm max}$ photons stream through the Universe with mean free paths much greater than the bubble size. While they do not contribute much to the ionization, the photoionizations from these hard photons heat the IGM in an approximately uniform manner with a rate of

$$\frac{dQ^{\rm hard}_{\rm HeII}}{dt}(z) = n_{\rm HeII}(z) \int_{E_{\rm max}}^{\infty} \frac{dE}{E}(E - E_{\rm HeII}) J_E(z) \sigma_{\rm HeII}(E). \tag{2.12}$$

Here the specific intensity of this hard background at redshift z_0 is

$$J_E(z_0) = \frac{c}{4\pi} \int_{z_0}^{\infty} dz \left| \frac{dt}{dz} \right| \frac{(1+z_0)^3}{(1+z)^3} \epsilon_E(z) e^{-\tau_{\rm HeII}(z_0,z,E)}, \tag{2.13}$$

where we parameterize the specific emissivity as $\epsilon_E = AE^{-\alpha}$ [erg $\rm s^{-1}cm^{-3}eV^{-1}$]. The normalization factor A can be solved for by requiring that the total ionizing emissivity of ionizing photons balances the number of ionizations plus recombinations:

$$\int_{E_0}^{\infty} dE \epsilon_E = \bar{n}_{\rm He} \left(\frac{d\bar{x}_{\rm HeIII}}{dt} + C_{\rm HeIII} \alpha_B \bar{x}_{\rm HeIII} \bar{n}_e \right), \tag{2.14}$$

where $\bar{x}_{\rm HeIII}$ is the instantaneous mean ionization fraction of He III, and $C_{\rm HeIII}$ is a clumping factor enhancement in the recombination rate over a homogeneous Universe with $T = 10^4$K. Both $\bar{x}_{\rm HeIII}(z)$ and $C_{\rm HeIII}$ are specified in our model. The specific intensity of this background depends on optical depth to redshift z of photons emitted at $z_{\rm em}$:

$$\begin{aligned} &\tau_{\rm HeII}(z_{\rm em}, z, E) = \\ &\int_{z_0}^{z_{\rm em}} \frac{c\, dz}{H(z)(1+z)} \sigma_{\rm HeII} \left(E \frac{1+z}{1+z_0} \right) \bar{n}_{\rm HeII}(z). \end{aligned} \tag{2.15}$$

Regions that become ionized by a local quasar will have the photoheating from the hard photon background terminated, as there are no more He II ions to ionize.

Our implementation of He II reionization is based on applying these two photoheating processes to an ensemble of gas parcels. Different gas parcels in the ensemble experience He II reionization at different times. When the first parcel becomes reionized, the remaining parcels begin to experience heating from the hard photon background. This is subsequently shut off in a parcel as soon as it becomes reionized and experiences instantaneous heating. Allowing individual regions to heat and subsequently cool separately provides a more realistic scenario than a one-zone model which implements uniform heating from a UV background (as done in Puchwein et al. 2015). In what follows, the two heating regimes are delineated by an upper limit to short mean free path photons of $E_{\rm max}^{\rm inst} = 150$ eV. We find that our results are negligibly changed by varying $E_{\rm max}^{\rm inst}$ over the plausible range of 100 to $200\,$eV with a maximum temperature variation of ~ 1500 K, corresponding to $\lambda_{\rm MFP} = 5 - 40$ comoving Mpc at $z = 3$ (eqn. 2.10).

Figure 2.3 shows the values of $T(\Delta)$ in a characteristic model at redshifts before and during He II reionization. The values of $T(\Delta)$ follow a tight power-law until He II is reionized in the first regions. These regions are then heated by $\sim$ 8000 K. As new regions become ionized, the first He III bubbles cool, introducing spread in the temperature-density relation. In addition, the hard background progressively builds up and heats the regions in which the He II has yet to be ionized. The maximum dispersion in the temperature at fixed Δ in our models is found at $z \sim 3$ when He II reionization terminates. Afterwards the IGM cools and unshocked gas is driven to a single temperature-density relation (Hui & Gnedin, 1997). The distribution in temperatures in our models is similar to that found in radiative transfer simulations of He II reionization (McQuinn et al., 2009) and Compostella et al. (2013).

In Figure 2.6 we calculate the temperature at mean density, T_0, in a simplistic model in which the global He III fraction is a linear function of redshift. This means that the He III fraction evolves as a linear function of redshift with $x_{\rm HeIII} = 0$ at $z = z_{\rm rei,HeII}^{\rm max}$ and $x_{\rm HeIII} = 1$ at $z = z_{\rm rei,HeII}^{\rm min}$. Unless otherwise noted, we assume fiducial parameters of $\alpha_{\rm QSO} = 1.7$ for the spectral index of quasars' intrinsic emission, $\alpha_{\rm bk} = 1.0$ for the spectral index of the ionizing background, $2.8 < z_{\rm rei,HeII} < 4$ for the duration of He II reionization, and $C_{\rm HeIII} = 1.5$ for the He II clumping factor (which is proportional to the recombination rate). The top panel of Figure 2.6 varies the spectral index of quasars between $\alpha_{\rm QSO} = 1.3$ and $\alpha_{\rm QSO} = 1.7$, the middle panel varies the duration of He II reionization such that reionization spans $2.8 < z_{\rm rei} < 4$ and $2.8 < z_{\rm rei} < 5$, and the bottom panel varies the clumping factor of He III gas over $1.5 \leq C_{\rm HeIII} \leq 4.5$. The range of quasar spectral indexes is motivated by the range of constraints from the stacking analyses (Telfer et al., 2002; Shull et al., 2012; Lusso et al., 2015). The range of He II reionization redshifts is motivated by the histories found in analytic calculations and simulations (Furlanetto, 2009; McQuinn et al., 2009). The range of clumping factors $C_{\rm HeIII}$ is motivated by the simulations in McQuinn (2012), in which intergalactic absorbers were exposed to a wide range of He II ionizing backgrounds. In each panel, the observational measurements (points with error bars) have been extrapolated to T_0 using this fiducial model's $T-\Delta$ relation. Most models are in striking (qualitative) agreement with the measurements. Figure 2.6 shows that the thermal history of the IGM is mildly affected by the spectral index of the quasars, and it is insensitive to changes in the clumping factor for a physically motivated range of values. However, the middle panels shows that the thermal history is very sensitive to the duration of He II reionization. The measurements of Becker et al. (2011) and Boera et al. (2014) clearly favor the case with $2.8 < z_{\rm rei,HeII} < 4$ over the case with $2.8 < z_{\rm rei,HeII} < 5$.[7]

In Figure 2.7 we adopt a reionization history that uses the fitting formula for the quasar emissivity given in Haardt & Madau (2012). This formula is based on constraints on the Hopkins et al. (2007) luminosity function. Unlike the previous models that assumed a linear-in-redshift He II reionization history, we now use this formula to self-consistently solve for the He II fraction also assuming a clumping factor to determine the recombination rate in He III regions. The top panel of Figure 2.7 varies the spectral index of the H I ionizing background between $\alpha_{\rm bk} = -0.5$ and $\alpha_{\rm bk} = 1.5$, the middle panel varies the intrinsic spectral index of quasars between $\alpha_{\rm QSO} = 1.3$ and $\alpha_{\rm QSO} = 1.7$, and the bottom panel varies the clumping factor from $C_{\rm HeIII} = 1.5$ to $C_{\rm HeIII} = 4.5$. (Increasing $C_{\rm HeIII}$ over this range delays the end of He II reionization by $\Delta z \approx 0.3$.) As before, we assume fiducial parameters of $\alpha_{\rm QSO} = 1.7$, $\alpha_{\rm bk} = 1.0$, and $C_{\rm HeIII} = 1.5$, unless otherwise noted, and the observational measurements have been extrapolated to T_0 using this fiducial model's $T-\Delta$ relation. These models with more empirically motivated He II reionization histories than the previous linear histories also show qualitative agreement with the measurements. In detail, we find the

---

[7] It should be noted that our models' predicted T_0 are slightly lower than in the HeII reionization simulations of McQuinn et al. (2009). The McQuinn et al. (2009) models predicted that the peak in T_0 falls between 16,000 and 20,000K, with the exact value depending on the run specifications (whereas our fiducial model yields a peak of approximately 15,000K). We attribute these differences to McQuinn et al.'s relatively hard choice of $\alpha_{\rm bk} = 0$, their initialization temperature at z=6 being higher than in our models (where we more consistently model the high-redshift temperature evolution), and their calculations ignoring free-free cooling (which results in a 1K difference).

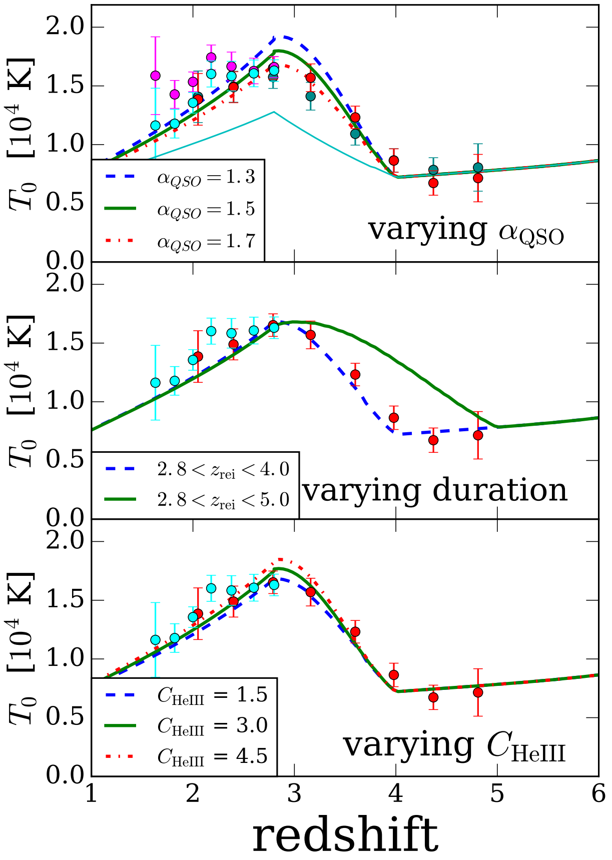

Figure 2.6: Average temperature of the IGM at the cosmic mean density for the case in which He II reionization has a He III fraction that is linear over $2.8 < z < 4.0$. Top panel: Models that vary the spectral index of quasars during He II reionization fixing $z_{\rm max,HeII} = 4.0$ and $C_{\rm HeIII} = 1.5$. The bottom thin, teal curve corresponds to a thermal history with the fiducial parameters and the hard background photons turned off. Middle panel: Models that vary the duration of He II reionization fixing $C_{\rm HeIII} = 1.5$ and $\alpha_{\rm QSO} = 1.7$. Bottom panel: The effect of varying the recombination rate, $C_{\rm HeIII}$, on the temperature during He II reionization fixing $\alpha_{\rm QSO} = 1.7$ and $z_{\rm max,HeII} = 4.0$. The points with error bars are the measurements of Becker et al. (2011) and Boera et al. (2014). In the top panel, the red Becker points have a pressure smoothing corrections and the green Becker points have no correction. The cyan Boera points have an optical depth adjustment and the magenta points do not (see Appendix 2.8). All of the plotted models assume that H I reionization instantaneously heats the IGM to $T = 20,000$ K at $z = 9$, but we show in § 2.4 that our results depend weakly on this assumption.

thermal history in this models is most sensitive to $\alpha_{\rm bk}$: The Becker et al. (2011) and Boera et al. (2014) measurements across $3 < z \lesssim 5$ favor the models with the softest spectrum of $\alpha_{\rm bk} \approx 1.5$. On the other hand, the measurements at redshifts $z \lesssim 3$ are somewhat above our fiducial thermal history (the green solid curve in all panels) and well above the $\alpha_{\rm bk} = 1.5$ dashed curve in the top panel. A hardening of the background spectrum as quasars become increasingly dominant with decreasing redshift could explain some of this trend. In addition, in the next section we address the possibility that this excess owes to heating mechanisms beyond the photoheating we have so far considered.

2.6 Non-standard heating processes

Beyond the standard processes already discussed, some have speculated additional heating mechanisms may contribute to the temperature evolution of the IGM, such as heating from cosmic rays[8] (Samui et al., 2005; Lacki, 2013), from the intergalactic absorption of blazar TeV photons[9] (Broderick et al., 2012; Chang et al., 2012; Puchwein et al., 2012), from broadband intergalactic dust absorption (Inoue & Kamaya, 2008), or from the byproducts of dark matter annihilations (Cirelli et al., 2009). Here we constrain how much heating could owe to these processes.

We first consider the excess heating that the temperature measurements allow over a model with the minimum possible amount of photoheating. In particular, to generate this minimum-photoheating model, we take our fiducial model ($T_0 = 20,000$ K and $z_{\rm rei} = 9$) with quasar and background spectral indices on the softer side of potential values, $\alpha_{\rm QSO} = 1.7$ and $\alpha_{\rm bk} = 1.0$ (see discussion in § 2.4), and with the expected recombination rate also on the low side with

---

[8] We note that cosmic rays may be more likely to pressurize rather than heat the IGM depending on their energy spectrum (Lacki, 2013). Whether they heat the IGM depends on their energy which sets their loss timescale, with losses occurring most efficiently around $\sim$ 1MeV (Samui et al., 2005) In the case where they only pressurize the IGM, they would show up in the pressure-smoothing dependence of Lyα lines but not in their thermal broadening. Lyα forest temperature measurements are sensitive to both effects, although more sensitive to the latter. Thus, constraints on the non-thermal pressurization of the IGM from $\langle|\kappa|\rangle$ measurements would likely be much weaker.

[9] The blazar TeV photons interact with radiation backgrounds, producing $e\pm$ pairs. The IGM heating is driven by streaming instabilities between the pair beam and IGM (Broderick et al., 2012). However, see Miniati & Elyiv (2013) and Sironi & Giannios (2014) for arguments why these instabilities may not occur, although we note that there is still an active debate (A. Broderick, private communication).

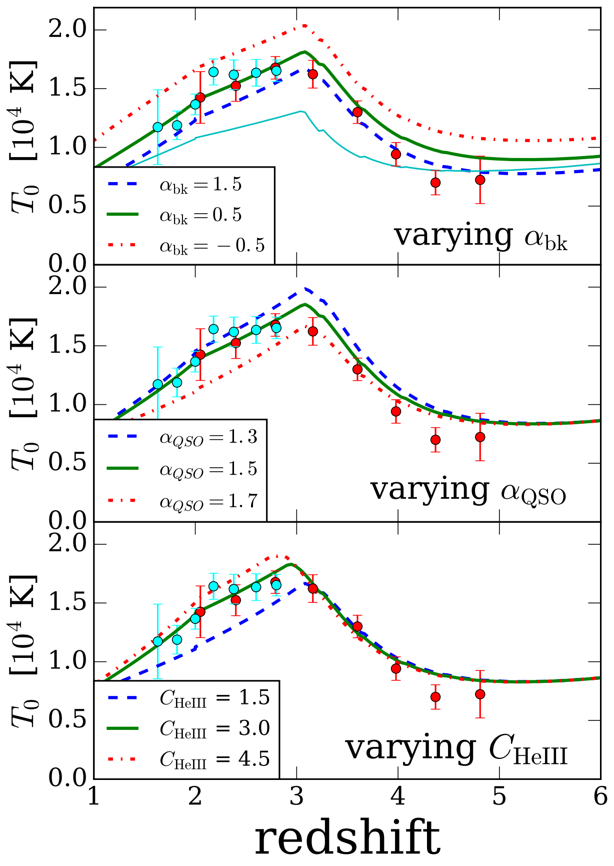

Figure 2.7: Average temperature of the IGM at the cosmic mean density for the case in which the He III fraction is determined by the quasar emissivity as calculated from the quasar luminosity function of Hopkins et al. (2007). Top panel: Models that vary the background spectral index fixing $\alpha_{\rm QSO} = 1.7$ and $C_{\rm HeIII} = 1.5$. The bottom thin, teal curve corresponds to a thermal history with the fiducial parameters and the hard background photons turned off. Middle panel: Models that vary the spectral index of quasars fixing $\alpha_{\rm bk} = 1.0$ and $C_{\rm HeIII} = 1.5$. Bottom panel: Models that vary the recombination rate through the clumping factor, fixing $\alpha_{\rm QSO} = 1.7$ and $\alpha_{\rm bk} = 1.0$. The points with error bars are the measurements of Becker et al. (2011) and Boera et al. (2014). The Becker points have a pressure smoothing corrections and the Boera points have an optical depth adjustment (See Appendix 2.8). All of the plotted models assume that H I reionization instantaneously heats the IGM to $T = 20,000$ K at $z = 9$, but we show in § 2.4 that our results depend weakly on this assumption.

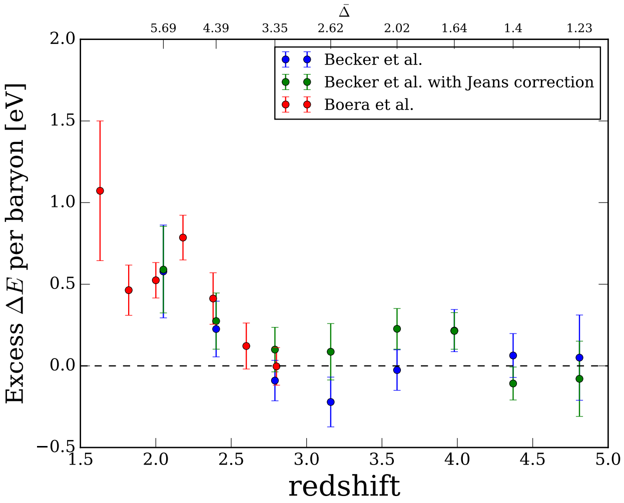

Figure 2.8: The excess energy per particle at $\Delta_\star$ between the measurements and our model with minimal photoheating. This excess provides an upper bound on the amount of energy that can be injected by different non-standard heating models.

$C_{\rm HeIII} = 1.5$. We remind the reader that the data is mostly insensitive to the details of hydrogen reionization[10], for which we assume an instantaneous reionization process with $T_{\rm rei} = 20,000$ K at $z = 9$. Figure 2.8 shows the excess energy per baryon above this minimum-photoheating model at the $\Delta_\star$ of the measurements, which are displayed on the top axis. We find that an excess energy of 1 eV per baryon between $z = 2$ and $z = 3$ can be accommodated by the Becker et al. (2011) and Boera et al. (2014) measurements. The allowed excess heating is smaller at higher redshifts.

This constraint does not account for cooling and adiabatic heating. Accounting for cooling would allow the amount of non-standard heating to be somewhat higher, especially if the heat injection were extended in time. In what follows, we model the heating as a function of time to account for cooling.

The proposed non-standard heating mechanisms would inject heat with different temporal trends and in a manner that differs in which gas densities are heated up more. With regard to

---

[10] The exception to this insensitivity is that the thermal history may impact the pressure smoothing at $z \sim 4-5$, hence the inferred temperatures.

density, the intergalactic absorption of blazar TeV photons is the most straightforward, injecting energy in a volumetric manner (Chang et al., 2012; Puchwein et al., 2012), although with a small level of spatial fluctuations (Lamberts et al., 2015). Cosmic ray heating (Samui et al., 2005; Lacki, 2013) and heating due to broadband intergalactic dust absorption (Inoue & Kamaya, 2008) are more likely to scale with density to some power as they are sourced by star forming regions within galaxies (and the cosmic rays may adjust to achieve equipartition with the gas pressure). With regard to their temporal scaling, blazar heating likely traces the history of supermassive black hole accretion, and cosmic rays and dust are more likely to trace the evolution of the star formation rate density. Conveniently, the quasar emissivity history and the evolution of the star formation rate density are largely similar, with the star formation rate density falling off more slowly at higher redshifts (where the IGM is less sensitive to additional heating anyway). Thus, a reasonable parametrization for a generic excess heating process is that it traces the quasar emissivity history and that it scales with density as Δ^n for $n \geq 0$. We consider $n = 0$ and $n = 1$ here.

Figure 2.9 adopts this parametrization, showing $T(\Delta_\star)$ for different amounts of total heat injected into the IGM that are normalized over the quasar emissivity history such that 1.0 and 3.0 additional electron volts are added per particle at $\Delta = 0$, with $\{33\%, 62\%, 90\%\}$ of the heating occurring by $z = \{4, 3, 2\}$. The top panel injects this heating in a mass-weighted manner (scaling with Δ) and the bottom a volumetric manner (no Δ dependence so the energy per particle scales as Δ^{-1}). We use the same functional form for the quasar emissivity as in Figure 2.7, and again we use the minimal-photoheating parameters $\alpha_{\rm QSO} = 1.7$, $\alpha_{\rm bk} = 1.0$, and $C_{\rm HeIII} = 1.5$. In addition, Figure 2.10 shows instead T_0 for different amounts of total heat injected into the IGM at the cosmic mean density rather than at $\Delta_\star$. The heat input is normalized such that 0.5, 1.0, 2.0, and 3.0 additional electron volts are added per particle over the entire quasar emissivity history. To extrapolate to T_0 from $T(\Delta_\star)$, we use the $T - \Delta$ relation from the model with no additional heating input.

Previously published models for blazar heating (Chang et al., 2012; Puchwein et al., 2012), cosmic ray heating (Samui et al., 2005), dust heating (Inoue & Kamaya, 2008), and dark matter annihilation heating (Cirelli et al., 2009) have forecasted heat injections at $\Delta_\star$ of more than 1 eV per particle by the lowest considered redshifts. (Blazar heating may be the least constrained by our

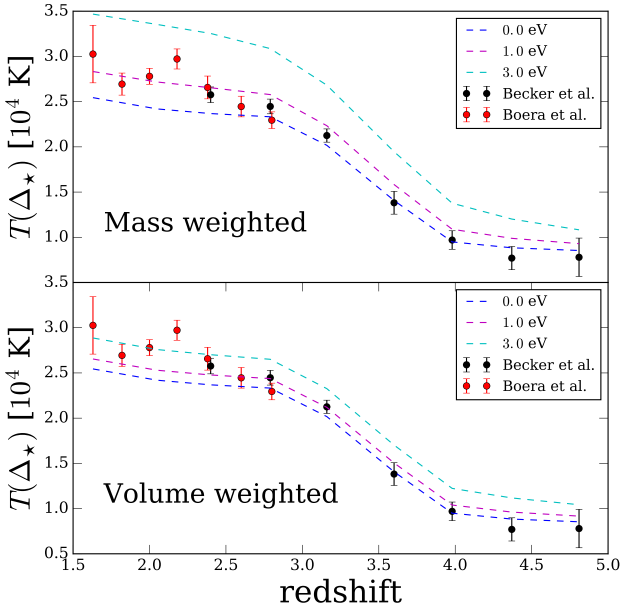

Figure 2.9: Temperature of the IGM at the densities corresponding to the Becker et al. (2011) and Boera et al. (2014) measurements with minimal photoheating and additional heat injection. This injection is normalized such that a total of either 0.0, 1.0 or 3.0 additional electron volts are added per particle at the mean density by $z = 0$ over the minimal photoheating model in a manner that traces the quasar emissivity history, a parametrization motivated in the text. The top panel shows models in which the additional heat injection is mass weighted (the injected energy per particle is the same at all Δ), and the bottom panel shows models where it is volume weighted (the injected energy per particle scales as Δ^{-1}).

analysis because it is volumetric, which only in the most extreme models of Puchwein et al. 2012 result in 1 eV per particle at $\Delta_\star$ by $z = 2$.) Thus, our limits place constraints on the parameter space of these models. However, there is not a lower bound on the heating predicted for any of these mechanisms and so our constraints do not rule out these processes contributing at the sub-eV level.

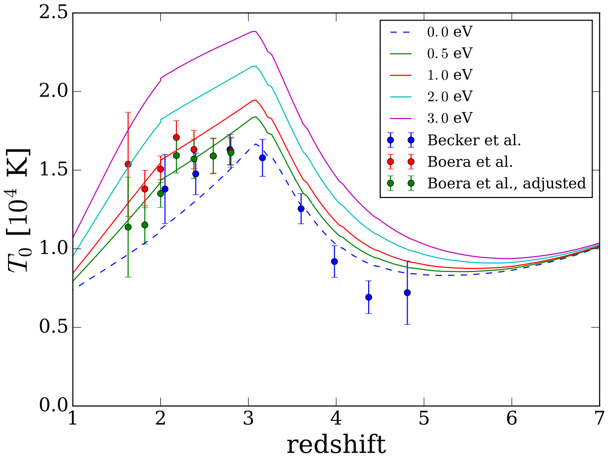

Figure 2.10: Average temperature of the IGM at the cosmic mean density in our minimal photoheating model and in models with additional heat injection. This injection is normalized such that 0.5, 1.0, 2.0, and 3.0 additional electron volts are added per particle by $z = 0$ over the minimal photoheating model in a manner that traces the quasar emissivity history, a parametrization motivated in the text.

2.7 Conclusions

The standard picture for the thermal history of the IGM is that it is shaped by two major heating events – the reionization of H I and of He II. We developed a model for the thermal history in this picture and compared it against recent observations to constrain these and other heating processes.

Regarding H I reionization, we found that, because the temperature after reionization quickly cools to an asymptotic value, even the highest redshift temperature measurements (at $z = 4.8$) are consistent with most possible H I reionization scenarios. However, we showed that the temperature measurements do rule out extreme reionization scenarios in which 1) the reionization process has a short duration with $\Delta z \lesssim 3$ and ends at $z \sim 6$ and 2) a passing ionization front heats the gas to temperatures on the hotter side of the expected range, $T_{\rm rei} \approx 30,000$ K. On the other hand, we found that an extended reionization spanning $z = 6 - 9+$ with $T_{\rm rei} = 20,000$ K – the most likely value – is not ruled out by the high-redshift temperature measurements.

In addition, we found that our models of He II reionization that follow the cannonical quasar emissivity history (e.g. Hopkins et al. 2007) are consistent with the temperature measurements. These models result in the bulk of He II reionization occurring over $z = 3 - 4$. The measurements are not consistent with He II reionization scenarios where He II reionization started $\Delta z > 0.5$ earlier than $z = 4$. For example, we found a scenario with a linear ionization history between $z = 3 - 5$ produced temperatures at $z > 4$ that are well in excess of measurements. At a lower confidence level, our models are most consistent with the $z = 3.5 - 4.8$ temperature constraints if the H I-ionizing background is on the softer side of estimates ($\alpha_{\rm bkgd} \geq 1$). By lower redshifts, temperature measurements favor the ionizing background to harden or, instead, for there to be additional heating processes.

Finally, we placed upper bounds on additional heating mechanisms such as blazar heating, heating from cosmic rays, broadband intergalactic dust absorption, and other mechanisms. At $z > 3.5$, we found that the Becker et al. (2011) measurements allow little room for additional mechanisms ($\ll 1\,$eV per baryon). On the other hand, towards lower redshifts we found an increasing excess energy per baryon beyond our minimum photoheating model, reaching a maximum excess of ≈ 1 eV per baryon at Δ_* by $z = 2$.

Previous analytic studies of the IGM temperature have been based on a one-zone approach in which reionization is modeled to be a homogeneous process. These one-zone models have been used to constrain the reionization process when compared with IGM temperature measurements (Haehnelt & Steinmetz, 1998). The one-zone models of Theuns et al. (2002b) and Hui & Haiman (2003) were used to show that the temperature measurements prefer either reionization to occur after $z \sim 10$ or a $z \sim 3 - 4$ reionization of He II. More recently, Raskutti et al. (2012) used the redshift $z \sim 6$ temperature measurements from Bolton et al. (2012) to constrain reionization in the biased regions around quasars to have occurred between $z = 6$ and $z = 12$. This redshift range is consistent with what we determine for the general IGM. In addition, Puchwein et al. (2015) modeled both hydrogen reionization and He II reionization. Puchwein et al. (2015) used the photoheating rates from the Haardt & Madau (2012) ionizing background model, supplemented with a non-equilibrium photoheating implementation for during He II reionization. The Puchwein et al. (2015) approach has the advantage that they could run cosmological simulations with these heating rates and, hence, directly compare the curvature measurements of Becker et al. (2011) and Boera et al. (2014) to those from mocks constructed using the simulations. However, their approach has the disadvantage that one-zone models do not capture how intergalactic gas is heated and cooled during and after reionization processes. We also expanded upon their work by using a range of models (e.g. instead of assuming the rigid Haardt & Madau 2012 form) to explore how uncertain inputs (such as the timing of reionization processes) affect the thermal history. Perhaps because of the more physical implementation, our models perform better at describing the Becker et al. (2011) than those in Puchwein et al. (2015) as well as earlier one-zone models.

Future improvements in the understanding of the high-redshift IGM could come from several fronts. Firstly, temperature measurements at higher redshifts would better constrain hydrogen reionization processes (Lidz & Malloy, 2014; D'Aloisio et al., 2015). Additionally, the pressure smoothing of the IGM may be measurable with close pairs of quasar sightlines (Rorai et al., 2013). Finally, the He II Lyα forest may be able to better constrain the duration of He II reionization (Worseck et al., 2014). The agreement between some recent temperatures measurements and the models presented here suggests that we are zeroing in on a concordance model for the IGM thermal history.

We would like to thank E. Boera for useful conversations and we would also like to thank G. Becker for useful comments on the text.

2.8 Apendix: Corrections to the measurements

This appendix addresses in more detail two correction factors discussed and used in Chapter 2. The first is the way we account for the pressure smoothing in our temperature histories. The second is the adjustment to the densities of the Boera et al. (2014) measurements.

2.8.1 A. Accounting for pressure smoothing

Because pressure smoothing extends the spatial distribution of hotter gas, with the smoothing depending on how far sound waves can travel, the line widths of the Lyα forest spectra are sensitive to the temperature history and not just the instantaneous temperature that thermal broadening probes. This makes the measured "temperature" sensitive to the thermal history assumed. In Becker et al. (2011) (Section 4.5), two models that mimic He II reionization (T15fast and T15slow) were used to demonstrate the bias of pressure smoothing on the inferred simulation. In particular, the bias between the curvature-method recovered temperatures (which was calibrated on artificial temperature histories) from the T15fast and T15slow runs and the actual T15fast and T15slow simulation temperatures demonstrate the degree to which pressure smoothing skews the measurements for these particular histories. Because our model with a linear reionization over $2.8 < z < 4.0$ is similar in shape to the T15slow model, we use the T15slow pressure smoothing corrections to also correct our measurements as described in § 3.2.

Figure 2.11 shows the ionization histories Becker et al. (2011) used to calibrate their curvature measurements, their Models A15-E15, as well as their T15fast and T15slow runs. We also show our models with a linear ionization history over $2.8 < z < 4.0$ (characteristic of most of the He II reionizaiton calculations), and with $\alpha_{\rm QSO} = 1.7$, $C = 1.5$, and $\alpha_{\rm bkgd} = 1.0$. The duration of this model is most similar to T15slow, motivating our correction method (see § 3.2). We also show our most extended He II reionization history with the same parameters except $2.8 < z < 5.0$, which has a longer duration that T15slow. The corrections for this case will be smaller than used in the text. In Section 2.3.2, we provide quantitative assessments of these corrections.

2.8.2 B. Optical depth adjustments to the Boera measurements

In the main body, in addition to the original Boera et al. (2014) measurements, we show a set of measurements with corresponding adjusted Δ_* that have been recalibrated to use the same evolution of mean optical depth as in Becker et al. (2011) (Boera, private communication), rather than the internal mean optical depth estimated in Boera et al. (2014). This adjustment affects the ex-

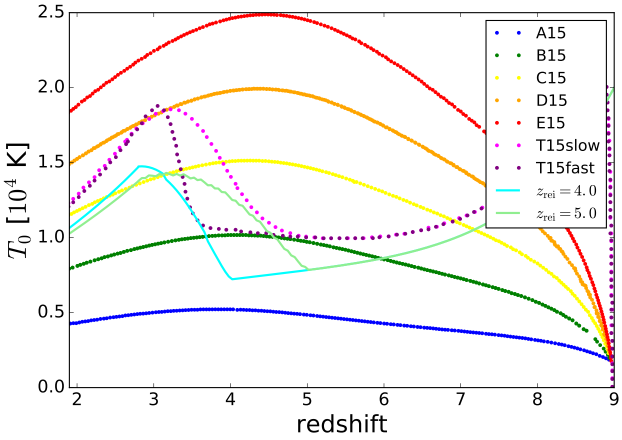

Figure 2.11: Models A15-E15, T15slow, and T15fast from Becker et al. (2011) with the two curves from the middle panel of Figure 2.6. Our two curves have linear He II reionizations scenarios and $C_{\rm HeIII} = 1.5$, $\alpha_{\rm bk} = 1.0$, $\alpha_{\rm QSO}$, with $z_{\rm max,HeII} = 4.0$ and $z_{\rm max,HeII} = 5.0$ respectively.

trapolation of the Boera et al. (2014) measurement to T_0, and it makes the Becker et al. (2011) and Boera et al. (2014) T_0 more consistent at overlapping redshifts. The mean optical depth in Becker et al. (2011) is estimated using a larger data set and agreed well with previous measurements (Faucher-Giguère et al., 2008), motivating this correction.

Chapter 3

THE SOURCES OF EXTREME ULTRAVIOLET AND SOFT X-RAY BACKGROUNDS

Material from this chapter was done in collaboration with Matthew McQuinn, Anson D'Aloisio, and Jessica Werk.

Radiation in the extreme ultraviolet (EUV) and soft X-ray holds clues to the location of the missing baryons, the energetics in stellar feedback processes, and the cosmic enrichment history. Additionally, EUV and soft X-ray photons help determine the ionization state of most intergalactic and circumgalactic metals, shaping the rate at which cosmic gas cools. Unfortunately, this band is extremely difficult to probe observationally due to absorption from the Galaxy. In this paper, we model the contributions of various sources to the cosmic EUV and soft X-ray backgrounds. We bracket the contribution from (1) quasars, (2) X-ray binaries, (3) super-soft sources, (4) hot interstellar gas, (5) circumgalactic gas, and (6) virialized gas, developing models that extrapolate into these bands using both empirical and theoretical inputs. While quasars are traditionally assumed to dominate these backgrounds, we discuss the substantial uncertainty in their contribution. Furthermore, we find that hot intrahalo gases likely emit an $\mathcal{O}(1)$ fraction of this radiation at low redshifts, and that interstellar and circumgalactic emission potentially contribute tens of percent to these backgrounds at all redshifts. We estimate that uncertainties in the angular-averaged background intensity impact the ionization corrections for common circumgalactic and intergalactic metal absorption lines by $\approx 0.3-1$ dex, and we show that local emissions are comparable to the cosmic background only at $r_{\rm prox}=10-100$ kpc from Milky Way-like galaxies.

3.1 Introduction

The extreme ultraviolet (EUV) through soft X-ray represent a slice of the electromagnetic spectrum that is difficult to observe in astronomical spectra. Not only must it be observed from above Earth's atmosphere, but for extragalactic sources much of this slice is absorbed by the Galaxy. Yet, because most transitions to ground Rydberg states of ions fall in this band and, hence, most cooling emissions, the EUV/soft X-ray extragalactic background holds clues into the location of the missing baryons, the energetics in stellar feedback processes, and the cosmic enrichment history. The lack of observations in this band complicates inferences from observable ionic transitions because these backgrounds often shape the ionic ratios of diffuse astrophysical gases.

AGN, or more specifically the brightest of these, quasars, are thought to be the dominate extragalactic source for radiation in the EUV and soft X-ray, especially at $z \lesssim 3$ (Meiksin & Madau, 1993; Madau et al., 1999; Faucher-Giguère et al., 2008; Haardt & Madau, 2012).[1] However, quasars' spectral energy distributions (SEDs) have only been measured at frequencies redward of ~ 25 eV (e.g. Telfer et al., 2002), and current theoretical models are likely not successful enough to motivate extrapolations to the soft X-ray. Thus, models for quasar spectra extrapolate with a single power-law between the EUV and soft X-ray, even though the quasar SED is certainly more complex (Bechtold et al., 1987; Laor et al., 1997; Done et al., 2012).

Quasars are not the only source that may contribute substantially to this critical waveband: X-ray binaries (XRBs), cooling gases (10^4-10^7 K) in the interstellar medium of galaxies (ISM) and the circumgalactic medium (CGM) that surrounds them, and virialized halo gas may also substantially contribute. Indeed, XRBs tend to dominate galactic X-ray emissions at $\gtrsim 1$ keV, while at lower energies radiative cooling from the hot ISM in galaxies is thought to become important (Grimes et al., 2005; Tüllmann et al., 2006; Owen & Warwick, 2009; Mineo et al., 2012b; Lehmer et al., 2015). This hot gas is the result of feedback from supernovae, massive star winds, and radiation pressure (McKee & Ostriker, 1977; Chevalier & Clegg, 1985; Strickland et al., 2000). A significant

---

[1] Starlight is an important contribution at $1-4$Ry in some models (and dominant at lower energies), with its relative importance depending on how efficiently these photons can escape from galaxies.

fraction of this feedback could also be radiated in the surrounding CGM in addition to the hot ISM (e.g., McQuinn & Werk, 2017). Similarly, intrahalo gas that has been shocked by virialization can also be important, especially with decreasing redshift as more massive and, hence, hotter systems form.

Many fields of study are reliant on models for the metagalactic ionizing background. Such models are used in essentially all calculations of the ionization state of photoionized gas in the intergalactic medium (IGM) and CGM (for a recent review see McQuinn, 2016; Tumlinson et al., 2017), and they are used to set the ionization state of gas in cosmological simulations (and, hence, shape the rate at which simulated gas cools). However, previous ionizing background models only considered the contribution of quasars in the EUV and soft X-ray, making the typical simplifying assumptions to extrapolate from observed bands (Haardt & Madau, 1996; Faucher-Giguère et al., 2009; Haardt & Madau, 2012). Even if the background is dominated by quasars, these models may not apply near galaxies (where they are most used), since many UV and X-ray sources are (circum)galactic in nature (Cantalupo, 2010; Gnedin & Hollon, 2012).

This paper estimates the contribution of all source classes that we are aware of that may emit substantially in the EUV and soft X-ray, in the process estimating the plausible range of $z \sim 0$ and $z \sim 2$ ultraviolet background angular-averaged specific intensities, J_ν. Section 3.2 estimates the emissivities of various EUV and soft X-ray sources. Using these estimates, we model the relative contribution of these sources to the ionizing background in Section 3.3. Section 3.4 discusses the impact of the uncertainties in the background on the ionization of highly ionized metals. Finally, for galactic sources, we estimate the size of the local enhancement expected around each galaxy in Section 3.5.

3.2 Modeling the sources

This section describes all the known sources that emit substantially in the UV and soft X-ray, developing models for their specific emissivity across redshift. These calculations are then fed into calculations of the background J_ν in Section 3.3.

3.2.1 Active galactic nuclei (AGN)

Quasars – highly luminous AGN – are likely the most emissive sources in the EUV and soft X-ray. Yet, their emissivity in this band is highly uncertain. Ultraviolet observations of quasar emissions can only be used to reliably estimate the mean SED to wavelengths as short as several hundred Angstroms (e.g. Telfer et al., 2002). A break is observed in the mean SED at $\lambda \sim 1000$ Å, with the spectrum softening blueward of this break. This break is commonly attributed to the innermost temperature of the quasar's accretion disk ('the Big Blue Bump'; Shakura & Sunyaev 1973) and the transition of quasar spectra to Compton up-scattered radiation from a coronae (e.g. Czerny & Elvis, 1987). However, thin accretion disk plus corona models have limited success at describing quasar spectra in the UV (Laor et al., 1997; Davis et al., 2007), which may be partly cured by invoking inhomogeneous temperatures (Dexter & Agol, 2011) and opacity effects (Czerny & Elvis, 1987). Additional tuning must be added to achieve power law-like emission into the soft X-ray as is observed (Bechtold et al., 1987; Laor et al., 1997): The disk emission almost certainly needs to be Compton up-scattered by material distinct from the traditional coronae. This could be accomplished by an optically thick region around the disk interior at temperatures of ~ 0.2 keV (Done et al., 2012).

Because of these open issues, UV background models have used, rather than theoretically-motivated templates, simple power-laws estimated from quasar stacks to extrapolate to shorter wavelengths. These power-laws fit stacked spectra blueward of the break at ~ 1000 Å and redward of the highest energy where the SED can be reliably estimated (~ 500Å). There is limited dynamic range over which the power-law is fit. The Lusso et al. (2015) stacked SED is the solid turquoise curve in Figure 3.1, with the cyan region highlighting the estimated 1-σ errors. We have normalized the SED to the $z = 0$ specific emissivity at 1 Ry as described below.

The effective power-law index of the quasar stacks, $\alpha_{\rm QSO}$ (see Equation 3.1), that analyses estimate varies significantly, with Telfer et al. (2002) finding $\alpha_{\rm QSO} = 1.57 \pm 0.17$ for their radio quiet sample, Shull et al. (2012) and Stevans et al. (2014) finding $\alpha_{\rm QSO} = 1.4 \pm 0.2$, and Lusso et al. (2015) finding $\alpha_{\rm QSO} = 1.7 \pm 0.6$, with their larger error owing to analysis differences described below. These observations show rough consistency (although they are discrepant with the lower luminosity sample of Scott et al. (2004), which finds $\alpha_{\rm QSO} = -0.6 \pm 0.4$). Lastly, photoionization calculations for the broad UV lines in these spectra favor somewhat softer spectra with $\alpha_{\rm QSO} \approx 2$ (Baskin et al., 2014; Lusso et al., 2015).

Lusso et al. (2015) pointed to several factors that result in differences in the estimated $\alpha_{\rm QSO}$ from stacking. Especially for quasars at $z \geq 1$, estimates for the stacked SED must correct for H I absorption from the IGM (with the Lyman series affecting $\lambda < 1216$ Å and Lyman-continuum $\lambda < 912$ Å). The differences in how this correction is done lead to some of the discrepancies in the reported values and their uncertainties. In addition, where the ~ 1000Å break wavelength is placed affects the final slope, and many samples do not have much spectral coverage of this break. Finally, broad line features are present in the stacks and so different choices are made for how to fit the continuum underneath the lines.

A justification often given for extrapolating with a single power-law into the soft X-ray is that the spectral indices of Type 1 AGN required in the EUV is similar to the spectral index needed to extrapolate to soft X-ray band, as well as the power-law index found in the soft X-ray (Laor et al., 1997). However, both in the UV and soft X-ray, individual systems show broad dispersion in their allowed index (although individual system inferences are difficult in the UV owing to IGM absorption). In addition, within the range of allowed mean spectral indices, there is no reason why there cannot be a softening followed by a hardening (indeed a soft spectrum followed by a hotter coronae spectra is seen in models such as Done et al. 2012) or vice versa (in the stacked SED, some quasars should harder and, hence, become more dominant at bluer wavelengths, hardening the spectrum).

Figure 3.1 shows the empirical estimates and extrapolation of quasar emissivity at $z \sim 0$. For our calculation, we use quasar emissivities reported at 1 Ry from Khaire & Srianand (2015), an update to the model of Haardt & Madau (2012) that reconciles the photon underproduction crisis (Kollmeier et al., 2014) and, hence, is consistent with the mean Lyα forest transmission (Fumagalli et al., 2017). These emissivities are extrapolated from the g-band luminosity function with the relation $\log \epsilon_g = \log \epsilon_{912} + 0.487$ (Khaire & Srianand, 2015; Haardt & Madau, 2012;

Boyle et al., 2000; Croom et al., 2004), and since the mean SED is much better known between these wavelengths – and the normalization is essentially calibrated to match robust constraints at 1 Ry from the Lyα forest – this extrapolation should not contribute significantly uncertainty.

We extrapolate from this emissivity at 1Ry with a power-law spectrum parametrized as

$$J(\nu) = J_0 \left(\frac{\nu}{\nu_{1\mathrm{Ry}}}\right)^{-\alpha_{\mathrm{QSO}}}. \tag{3.1}$$

We vary α_{QSO} between 1.1 and 2.3, the 1σ error bar of Lusso et al. (2015), a range shown by the dashed curves in Figure 3.1. However, one cannot extrapolate all the way to ≈ 1 keV with this spectrum unless it has $\alpha_{\mathrm{QSO}} \approx 1.7$ (Laor et al., 1997) to be compatible with soft X-ray background measurements discussed in § 3.3. We taper our spectrum starting at 100 eV so that it converges to the same point at 800 eV as if $\alpha_{\mathrm{QSO}} = 1.7$. While our choices here are somewhat arbitrary, we believe it provides a reasonable guess for the allowed range of quasar specific emissivities (motivated both by the error on UV extrapolations and the large theoretical uncertainty in the spectral form).

Above 800 eV, we assume the spectrum scales with a spectral index of $\alpha = 0.5$. While 800 eV is on the lower side of the observations for where the harder coronal emission dominates, finding $1-2$ keV (Laor et al., 1997), this spectral index is characteristic of the coronae of radio loud quasars, and somewhat harder than that found for radio quiet ones (although H I absorption additionally acts to harden their spectrum; Laor et al. 1997). The selected slope of $\alpha = 0.5$ is a good fit to the slope found in the more detailed models for this component in Haardt & Madau (2012) and also to $z = 0$ soft X-ray background measurements. However, our tapering to a single curve at > 800 eV, which is done to match the background intensity measurements in the soft X-ray, should underestimate the uncertainty in $\epsilon_\nu(z)$ at these energies. We justify not attempting to quantify the uncertainty > 800 eV because these higher energies are less important for this study.

3.2.2 X-ray binaries (XRBs)

The X-ray emission from galaxies is thought to be dominated by XRBs at > 1 keV. The galactic XRB emission from high mass XRBs should trace the star formation rate – as their formation lags

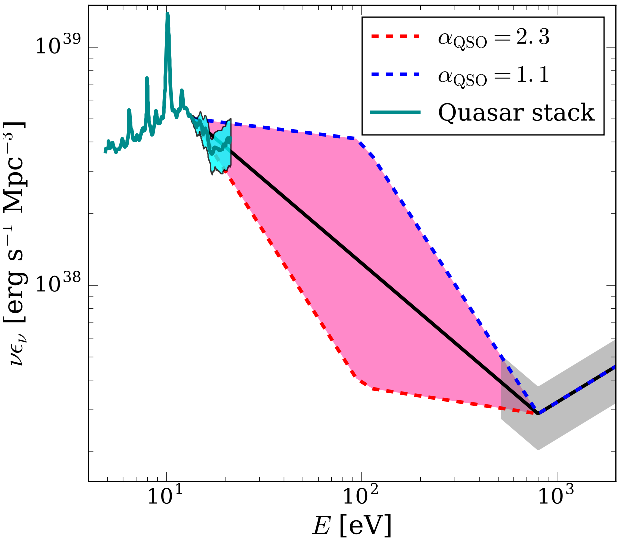

Figure 3.1: Observations and stacks of the quasar specific emissivities. The jagged turquoise solid curve shows the stacked quasar SED of Lusso et al. (2015), normalized to match the Khaire & Srianand (2015) specific emissivity at 1 Ry. Filled regions represent the range of allowed values. The solid line at $13.6-800$ eV is the fiducial power-law model with $\alpha_{\rm QSO}=1.7$. The Lusso et al. (2015) 1σ upper and lower limits on $\alpha_{\rm QSO}$ are shown by the blue and red dashed lines. The inner pink shaded region represents the range of viable specific, which are tapered to 800eV to match soft X-ray observations. The harder component above 800eV owes to coronal emission.

star formation episodes by just tens of megayears – and low mass XRBs should trace stellar mass – as theirs can lag star formation by many gigayears. These correlations have been confirmed observationally (Ranalli et al., 2003; Grimm et al., 2003; Gilfanov et al., 2004; Hornschemeier et al., 2005; Lehmer et al., 2010; Boroson et al., 2011; Mineo et al., 2012a; Zhang et al., 2012). We use these correlations to relate the cosmic XRB emissivity with redshift to the observed star formation rate density and stellar mass density. We approach the XRB contribution to the EUV/soft X-ray from both a theoretical and an empirical standpoint, considering two models:

Empirical Model In this model, all X-ray emission traces either the star formation rate or the stellar mass (Lehmer et al., 2010). Low-mass XRBs are likely as important as their high-mass counterpart in the average galaxy at $z \sim 0$, though at $z \gtrsim 1$ and in star forming galaxies, high-mass XRBs dominate the X-ray emission from XRBs. We allow the relationship between star formation rate and X-ray emission to account for temporal trends that result from such things as increasing cosmic metallicity.[2] For high-mass XRBs (HMXBs), we use the redshift-dependent relation constrained in Dijkstra et al. (2012), parametrized as $L_{X,0.5-8}/\mathrm{SFR} = [L_{X,0.5-8}/\mathrm{SFR}]_{z=0}(1+z)^b$, where $L_{X,0.5-8}$ is the $0.5-8$ keV X-ray luminosity. Dijkstra et al. (2012) finds $0 \leq b \leq 1.3$, anchoring to the Mineo et al. (2012a) best fit of $[L_{X,0.5-8}/\mathrm{SFR}]_{z=0} = 2.6 \times 10^{39}$ erg s^{-1} (M$_\odot$ yr^{-1})$^{-1}$. For the cosmic star formation rate density, we use the fit in Haardt & Madau (2012) derived from rest-frame optical and UV observations. [3] For low-mass XRBs (LMXBs), we use a correlation between total stellar mass and X-ray luminosity, $L_{X,0.5-8}/M_\star \sim 9 \times 10^{28}$ erg s^{-1} (Gilfanov et al., 2004; Lehmer et al., 2010). We use Wilkins et al. (2008) for the cosmic stellar mass density as a function of redshift.

This model's second ingredient is the XRB SED. Above 300 eV the SED of galactic X-ray emission has been constrained observationally. For the SED, we stack the spectrum of four star-

---

[2] Increasing metallicity is expected to decrease the number of XRBs because metallicity increases mass loss from stellar winds, affecting binary separations, and because higher metallicity stars have larger radii, which increases Roche lobe overflow (Linden et al., 2010). There is also observational evidence for X-ray flux scaling inversely with metallicity (Brorby et al., 2016).

[3] The total SFR density that is often estimated is likely less appropriate because star formation enshrouded behind gas and dust is unlikely to produce EUV and soft X-ray photons that can escape.

forming galaxy SEDs observed from $0.3-3$ keV with *Chandra/XMM-Newton* (Lehmer et al., 2015; Wik et al., 2014; Yukita et al., 2016). The stack is computed by averaging the specific luminosity per unit star formation rate (SFR) of each galaxy, $L_X(\nu)/\mathrm{SFR}$. However, the spectrum of XRBs is not constrained below 300 eV. To extrapolate, we model the XRB spectrum as a simple power law in specific luminosity with $\alpha_{\mathrm{empirical}} = 0.7$ (using the same conventions as with α_{QSO} in eqn. 3.1). This slope is based on the scaling of stacked X-ray emission – not just the four we use for our empirical spectrum (Rephaeli et al., 1995; Swartz et al., 2004).

The thick solid curves in Figure 3.2 (and later Fig. 3.3) show the resulting specific emissivity at $z = 0$ for the stacked SED and $\alpha_{\mathrm{empirical}} = 0.7$ models. Even among the four stacked galaxy spectra there is ~ 1 dex scatter in $L_X(\nu)/\mathrm{SFR}$, owing largely to scatter in the number of ultraluminous X-ray sources. An extremely crude estimate of the error on the mean stack is shown by the highlighted regions in Figure 3.2, which is the standard deviation of the four spectra divided by $\sqrt{N_{\mathrm{gal}} - 1}$.

We note that much of the emission below 1 keV is likely from hot gas in the ISM and not XRBs. Most XRB's emission is found to decline below 1 keV rather than have a flat power-law as our extrapolation assumes (because of their intrinsic spectrum and H I absorption), and the < 1 keV appears to owe to more diffuse sources as discussed in Section 3.2.4. Thus, our $\alpha_{\mathrm{empirical}} = 0.7$ model may be better conceived as an amalgam of XRB and hot ISM emission, where hot ISM takes over at lower energies and has a power law-like spectrum. We discuss the realism of this power-law extrapolation for ISM emission in Section 3.2.4. In addition, the bounds we place on super soft sources in § 3.2.3 also are relevant to potential soft emissions from LMXBs.

Fragos++(2013) Model We use the XRB population synthesis model of Fragos et al. (2013). It uses the XRB population synthesis simulations `StarTrack` (Belczynski et al., 2008), which are calibrated to observations of XRBs at low redshift, and the semi-analytic galaxy catalog of Guo et al. (2011), which models the star formation and stellar metallicity histories. The assumed SED is based on samples of observations of both neutron star and black hole XRBs. The overall shape of their XRB SED does not change significantly with redshift, despite accounting for trends in

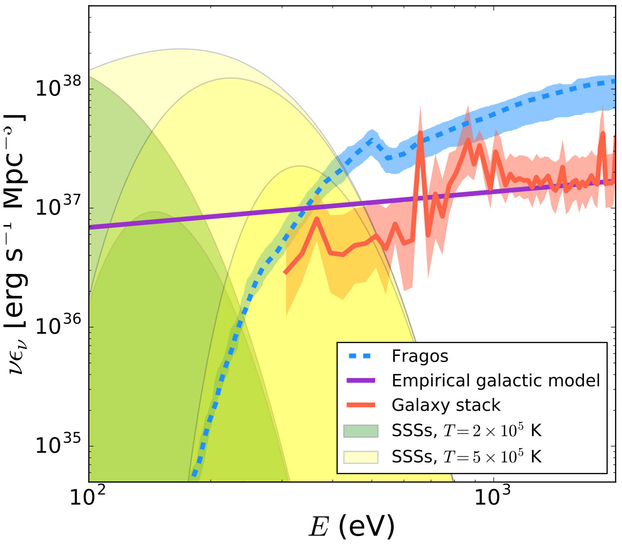

Figure 3.2: Soft X-ray models and bounds for the $z = 0$ specific emissivities of XRBs and SSSs. The solid purple and red curves represent respectively the empirical models described in the text assuming the power-law SED and the stacked four star-forming galaxies. The blue dashed curve represents the theoretical model of Fragos et al. (2013). The highlighted bands around the red solid and blue dashed curves are, respectively, the standard deviation estimated from the four stacked galaxies and the quoted uncertainties in Fragos et al. (2013). The light green and yellow shaded areas represent the allowed emissivity for SSSs with blackbody temperatures of 2×10^5 K and 5×10^5 K respectively, using the bound derived from elliptical galaxies Hα emission. The darker shaded regions in these allowed emissivities represent absorption by H I columns of 10^{20} cm^{-2} for the 2×10^5 K model and 10^{20} cm^{-2} and 10^{21} cm^{-2} for the 5×10^5 K model.

metallicity and the fraction of LMXBs to HMXBs. Emissivities at high redshift will be slightly enhanced relative to star formation rate density due to the lower metallicity of the stars in binary systems. This reduces stellar winds and increases Roche lobe overflow, increasing the number of XRBs, especially HMXBs. The spectrum falls off rapidly at energies lower than a few hundred electron volts, due both to the XRB SED and interstellar/circumstellar absorption associated with most XRBs. The dashed blue curve in Figure 3.2 shows this model, with the fainter blue band signifying their estimated uncertainties.

3.2.3 Super soft X-ray sources

Super soft X-ray sources (SSSs) are observed systems with blackbody spectra that peak in the soft X-ray and that are theorized to be compact binary systems with a white dwarf accreting from either a main sequence star or a red giant and this accretion igniting on the surface (Kahabka & van den Heuvel, 1997; Greiner, 2000). Accretion onto white dwarfs should be generic and such accretion is necessary in a major progenitor scenario of Type 1a supernovae. Models find that the accretion should be thermally stable with rates of $\dot{M} \sim 10^{-7} M_\odot$ yr^{-1} (Nomoto et al., 2007). With such $\dot{M}$, accreting white dwafs should emit substantially in the $0.1 - 0.7$ keV band. SSS could increase ISM photoheating rates enough to explain the higher temperatures inferred from photoionized ISM observations compared to models (Woods & Gilfanov, 2013).

However, the number of SSSs that have been detected is 1-2 orders of magnitude below expectations from population synthesis models (Chen et al., 2014, 2015). The lack of sources could be because of obscuring H I columns around these sources (although see Nielsen & Gilfanov 2015), if dynamically unstable mass loss for giant stars occurs differently from in current models (Chen et al., 2015), or if the nature of accretion onto these systems is different (Cassisi et al., 1998). Observations are sensitive to SSSs with a more massive white dwarf primary, so the smaller primaries (which are more important at lower energies) could still be present at forecast abundances.

Here we assume that stable accretion onto undetected (i.e. less massive) white dwarfs is occurring, and we attempt to place an upper bound on the total ionizing emissions. We assume that the spectrum of these objects follows a blackbody with an effective temperature ranging between 2×10^5 and 5×10^5 K, characteristic of the lower mass primaries that would go undetected in previous soft X-ray searches (Greiner, 2000).

The luminosity of SSSs is expected to roughly trace stellar mass and, hence, their ionizing emissions should be most dominant in elliptical galaxies – the galaxies with the lowest specific star formation rates. Thus, we can place an upper limit on the SSS contribution by assuming that any Hα emission from elliptical galaxies owes to recombinations sourced by SSSs' ionizing emissions. (This approach is similar to that in Woods & Gilfanov 2016, who calculated the expected Hα due to SSSs in the Large Magellanic Cloud. Our constraint from ellipticals is $\sim 30\times$ stronger.)[4] Yan & Blanton (2012) gives a relation between the Hα luminosity of the brighter (in Hα) half of sample of passive red galaxies and redshift, showing the average stellar continuum–corrected Hα luminosity of the sample to be $\sim 3 \times 10^{38}$ erg s^{-1} at $z \sim 0$.[5] We assuming that this Hα is the result of Case B recombinations for $\sim 10^4$ K gas (e.g. Osterbrock & Ferland, 2006). We then divide this luminosity by the average stellar mass of the sample, 7.5×10^{10} M$_\odot$, and multiply by the cosmic stellar mass of Wilkins et al. (2008) to estimate the global emissivity.

The resulting bound on the ionizing luminosity of SSSs assumes that the ionizing photons are absorbed by ambient gas within elliptical galaxies. We estimate the H I column densities in elliptical galaxies to be $N_{\rm HI} \sim 10^{19} - 10^{22}$ cm^{-2} from 21cm observations of Serra et al. (2008), with a median of $\sim 10^{20}$. Also note that for $N_{\rm HI} \sim 10^{20}$cm^{-2}, 98% and 73% of the ionizing photons are absorbed for $T = 2 \times 10^5$K and $T = 5 \times 10^5$K source temperatures, respectively. For a measly column of $N_{\rm HI} \sim 10^{19}$cm^{-2}, these become 76% and 34% (such diminutive columns are found even in the CGM around many ellipticals Tumlinson et al. 2013). Dust could also be a source of absorption. While dust extinction in ellipticals is found to be similar to that of the Milky Way (Patil et al., 2007; Kulkarni et al., 2014), since dust is more likely to absorb ionizing photons than Hα, its effect would be to strengthening our bounds.

If SSS source photons likely do not escape ellipticals, is it even plausible that they contribute to the ionizing background? There is still some wiggle room here. Even if most of their photons are absorbed in the host galaxy, as long as $N_{\rm HI} \ll 10^{21}$cm^{-2} (as may be the case in elliptical, dwarf galaxies, or the outskirts of spirals), they are relatively unobscured at ~ 200eV and so can contribute to the metagalactic background there. Furthermore, a substantial fraction likely reside in halo globular clusters ($\sim$ 40 percent of LMXBs in elliptical galaxies are found in globular

---

[4] The assumption that all Hα emission comes from SSS is likely extreme. In elliptical galaxies, Hα emission is more often associated with the ionizing flux from AGN or post-AGB stars, and in fact, models of post AGB stars in ellipticals have been able to reproduce equivalent widths of Hα in early type galaxies (Byler et al., in prep).

[5] There is 0.5 dex scatter around this luminosity. Our bound would be tighter if we took the lowest luminosity observed. However, it is unclear how much of this scatter owes to observational uncertainty, unseen AGN, or other highly stochastic sources of emission.

clusters, Kundu et al. 2007), for which emissions likely suffer little H I absorption. For our most conservative bound, we take all of the ionizing luminosity (i.e. summed over all SSSs) to escape. We also show models that experience absorption from a 10^{20} and 10^{21} column.

Figure 3.2 shows the allowed emissivity of SSSs. The green and yellow shaded areas represent the allowed emissivity for SSSs with blackbody temperatures of 2×10^5 K and 5×10^5 K respectively. The darker shaded regions within these models represent models attenuated by a 10^{20} cm^{-2} column for the 2×10^5 K model and 10^{20} cm^{-2} and 10^{21} cm^{-2} for the 5×10^5 K model. Our bound on SSSs allows for an excess of softer X-ray emission at $\lesssim 300$ eV, with a potential contribution that is as much as an order of magnitude above our empirical XRB model. For the emissivity of SSSs to compete with quasars at $z \sim 0$, our bound would have to be nearly saturated. However, we find in § 3.3 that, because they trace stellar mass which decreases with increasing redshift, SSSs are always subdominant to quasars in their contribution to the background intensity. These bounds, modulo spectral assumptions, are relevant for any ~ 100 eV source of ionizing photons that traces stellar mass.

3.2.4 Warm–Hot gas in the ISM and CGM

The ISM is a mix of different gas phases, with this multiphase structure driven largely by stellar wind bubbles and supernovae blastwaves (McKee & Ostriker, 1977). The spectrum of radiation emitted by these bubbles and blastwaves depends on the resulting temperatures and ionization states of associated gases. Some of this emission escapes into intergalactic space, with the amount depending on the H I columns out of the host galaxy. Furthermore, some of the gas driven by these feedback processes vents from galaxies, potentially heating the CGM and leading to additional cooling emission that has less difficulty escaping from the galactic environs.

Radiation from warm-hot gas in the ISM can in principle be observed directly at > 300 eV. However, there is no robust determination of this ISM X-ray emissivity because no straightforward method exists for disentangling the ISM contribution from the XRB one. Mineo et al. (2012b) attempted to disentangle the ISM contribution by subtracting off flux from X-ray point sources, which are likely XRBs, finding that most of the observed flux remains at the lowest energies observed, with little above 1 keV. Using the remaining flux as an estimate for the ISM contribution, they measured the relation between ISM emission and SFR:

$$L_{X,0.5-2}/\mathrm{SFR} \approx 8.3 \times 10^{38}\ \mathrm{erg\ s^{-1}}\ (M_\odot\ \mathrm{yr}^{-1})^{-1}, \tag{3.2}$$

where $L_{X,0.5-2}$ is the $0.5-2$ keV ISM luminosity.

Observationally the shape of the average ISM SED is essentially unconstrained at $< 300\mathrm{eV}$, and the more diffuse emission from the CGM is unconstrained at all wavelengths. To model the spectral shape, we use the spectrum of gas cooling from some maximum temperature to a much lower temperature. The specific emissivity of a population of objects with this spectrum is then given by

$$\epsilon_\nu(T_{\max}) = \dot{\rho}_{\mathrm{SFR}} \times [L_{\mathrm{bol}}/\mathrm{SFR}] \times \int_{T_{\min}}^{T_{\max}} dT\ \epsilon_{T,\mathrm{bol}}^{-1}\ \epsilon_T(\nu), \tag{3.3}$$

where $\epsilon_{T,\mathrm{bol}} = \int d\nu \epsilon_T(\nu)$, $\dot{\rho}_{\mathrm{SFR}}$ is the UV star formation rate, and $[L_{\mathrm{bol}}/\mathrm{SFR}]$ sets the normalization (which we develop models for shortly). We compute $\epsilon_T(\nu)$ using CLOUDY (Ferland et al., 2013) and assuming collisional ionization equilibrium[6]. We choose $T_{\min} = 10^4$K, although our calculations are not sensitive to this choice. In addition, our calculations assume a single metallicity of $Z = 0.3Z_\odot$ for $T_{\max} = 10^6$K and $Z = Z_\odot$ for $T_{\max} = 3 \times 10^6$K. However, since metal emission lines dominate the bolometric emission – what we normalize to – metallicity has little effect on the resulting spectrum.

We choose $T_{\max}$ to have values of 1×10^6 K or 3×10^6 K. The motivation for this spectral form is that gas tends to be shock heated to these temperatures by $10^2 - 10^3$ km s^{-1} flows before cooling. At these temperatures, cooling times tend to be short and so there is not often a heating process to halt cooling from running away. (Since we assume a single maximum temperature, our calculation misses that decelerating blastwaves tend to shock gases to a range of temperatures.) In the CGM, our simple model has the additional motivation that gas may be cooling from the $\sim 10^6$K virialized phase characteristic of star forming galaxies.

---

[6] To understand the effect of ionizing backgrounds on our predictions, we have computed the ionization state with the Haardt and Madau 1996 model and $nT = 10\mathrm{K\ cm^{-3}}$ and $nT = 100\mathrm{K\ cm^{-3}}$, thermal pressures justified in McQuinn & Werk (2017). We find there is a negligible difference in the spectra and thus the photoionization background does not have a significant effect on the resulting SED of the hot gas.

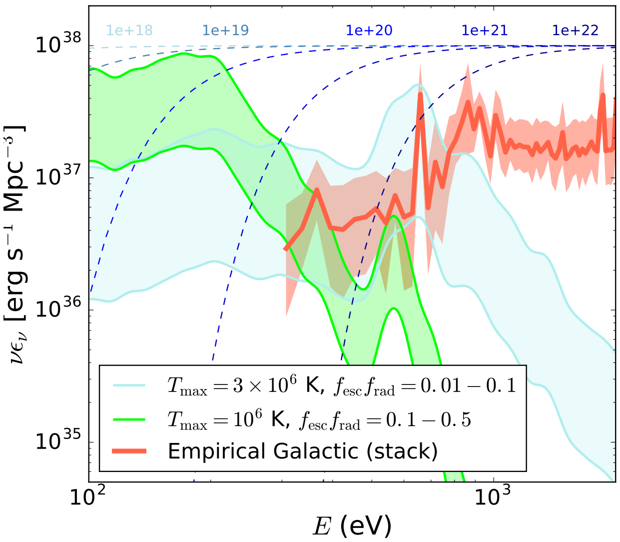

Figure 3.3: Estimates for the $z = 0$ ISM and CGM emissivities using the models discussed in § 3.2.4. The turquoise band is our fiducial, theoretically-calculated ISM emissivity that uses equation (3.4) with $T_{\rm max} = 3 \times 10^6$ K and $f_{\rm esc} f_{\rm rad} = 0.01 - 0.1$. The green band is our CGM/ISM emissivity that also uses Equation 3.4, but with $T_{\rm max} = 10^6$ K and $f_{\rm esc} f_{\rm rad} = 0.1 - 0.5$. The red curve represents the stack of four star-forming galaxies (the empirical model in § 3.2.2). The various blue dashed curves represent the amount of H I + He I absorption for hydrogen column densities increasing from 10^{18}cm^{-2} to 10^{22}cm^{-2}.

This model assumes collisional ionization equilibrium (CIE) cooling, which is likely not a good approximation for ISM cooling. McQuinn (2012) used Allen et al. (2008) models for unmagnetized supernovae shocks to compute the spectrum of a supernovae blastwave as it decelerates in a constant density medium of density 1 cm^{-3}. This calculation includes the non-equilibrium ion abundances and consistently models the self-ionization of the shock They found a spectrum that on average scales as $\alpha = 1.7$, between 10 eV before a cutoff at ~ 1 keV. Such a spectral index between $10^2 - 10^3$eV falls in between the effective scaling of our two considered $T_{\rm max}$ models.

Our normalization of the ISM and CGM emissivities uses that the radiated energy is likely a significant fraction of the total feedback energy. We consider supernova feedback, although stellar winds can be comparable energetically (Leitherer et al., 1999). The bolometric luminosity per unit

SFR – what sets the emissivity normalization in our models (eqn. 3.3) – is

$$[L_{\rm bol}/{\rm SFR}] = f_{\rm esc} f_{\rm rad} f_{\rm SN} E_{\rm SN}, \tag{3.4}$$

where $f_{\rm SN}$ is the approximate fraction of stars expected to go supernova that we take to be 10^{-2}, $E_{\rm SN}$ is the approximate energy output per supernova that we take to be 10^{51}erg s^{-1}, $f_{\rm rad}$ is the fraction of the feedback energy that is radiated, and $f_{\rm esc}$ is the fraction that escapes the galaxy. Calculations find that $f_{\rm rad} \approx 0.9$ in the local ISM surrounding supernovae if they are unclustered (Thornton et al., 1998), and that for clustered supernovae this fraction can go down to $f_{\rm rad} \approx 0.5$ (Sharma et al., 2014). Much of the energy which is not radiated in the ISM (or, if radiated, that is re-absorbed) is likely radiated in the CGM where $f_{\rm esc} \approx 1$: McQuinn & Werk (2017) argued that the large OVI columns require $f_{\rm rad} > 0.1$ in the CGM, and large $f_{\rm rad}$ appear to be born out in numerical simulations of the CGM (Fielding et al., 2017; van de Voort & Schaye, 2013). Observations further suggest that the characteristic scale for the CGM emission extends many tens of kiloparsecs outside of the galaxy (Werk et al., 2014), and so this diffuse emission would likely go undetected in soft X-ray images even if the gas reached sufficiently high temperatures to be seen in the soft X-ray. We note that this energetics-motivated model for CGM emission is similar to that of Miniati et al. (2004, except they assume emission at $T_{\rm vir}$), as are our conclusions for the potential impact on J_ν.

In our model of the CGM emission (though it can also be colder, less obscured ISM emission), we take the possible range for escaping emission to be $f_{\rm esc} f_{\rm rad} = 0.1 - 0.5$ and $T_{\rm max} = 10^6$K. This 'CGM/ISM' model is shown by the green band in Figure 3.3. This spectrum peaks at hundreds of eV, and falls off below the X-ray measurements at > 300eV. However, we again note that falling below the X-ray measurements is not required as this emission could be too diffuse to detect.

For hotter ISM gas with $T_{\rm max} \approx 3 \times 10^6$ K, we tune the normalization to meet the observations, finding $f_{\rm esc} f_{\rm rad} = 0.01 - 1$. This 'ISM' model is shown by the turquoise band in Figure 3.3. Much of the ISM radiation is likely absorbed in the galaxy to produce such low $f_{\rm esc} f_{\rm rad}$: the blue dotted lines represent the H I + He I transmissions for H I column densities ranging from 10^{18}cm^{-2} to 10^{22}cm^{-2}. Large H I columns of $\sim 10^{22}$cm^{-2} are necessary to obscure the X-ray emission.

Additionally, lower columns would obscure ISM models with smaller $T_{\rm max}$.

For both the ISM and CGM models, we assume the same range of $f_{\rm esc} f_{\rm rad}$ holds with redshift to compute J_ν in § 3.3. As the properties of galaxies change, and it is thought that the escape of ionizing photons goes up with redshift, this might underestimate temporal trends, especially for J_ν at higher redshifts.

3.2.5 Virialized hot halo gas

This section considers the emission from virialized gas in massive halos. We distinguish this scenario from the diffuse CGM gas previously considered in that, as cooling times get longer in larger systems, a roughly single temperature hydrostatic virialized region forms, whereas the CGM emission owes to cooling gas and likely a range of temperatures. A second distinctions is that the CGM emission is sourced by halos where most star formation occurs in the Universe, $\sim 10^{12} M_\odot$ halos, whereas we will see that hot halo emission owes to systems at least an order of magnitude larger (and is powered by virialization and quasar feedback).

The hot gas scenario should be thought of as being essentially the same as warm hot intergalactic medium emission that has been discussed extensively by prior studies as a source of the soft X-ray background (Cen & Ostriker, 1999; Davé et al., 2001; Croft et al., 2001). While some of the diffuse emission likely comes from filamentary gas, most is likely to come from gas associated with halos as modeled in Pen (1999). There is 25% (15%) of dark matter in $> 10^{13} M_\odot$ halos at $z = 0\ (0.5)$, and 10% (5%) of dark matter in $> 10^{14} M_\odot$ halos. Filamentary gas is too diffuse (and, possibly, too unenriched) to compete with virialized regions even though it constitutes a somewhat larger mass fraction. The amplitude of this emission is more sensitive to how the associated gas is distributed around halos, which we discuss below.

Group and cluster virialized gas emits in the EUV and soft X-ray of massive halos via free-free and atomic line emissions, with the latter becoming more prominent in lower temperature halos. The X-ray emission from virialized gas that has been measured for $\gtrsim 10^{13} M_\odot$ halos can be directly observed (Jeltema et al., 2008; Holden et al., 2002; Markevitch, 1998; Helsdon & Ponman, 2000; Mulchaey et al., 2003; Della Ceca et al., 2000; Arnaud & Evrard, 1999; Borgani et al., 2001; Pratt et al., 2009), and we design our models to latch onto these observations. In particular, we use the models of Sharma et al. (2012) based on timescale considerations, which are able to fit the observed X-ray luminosity – temperature relation (L_X-T_X). In particular, McCourt et al. (2012) and Sharma et al. (2012) find (using simulations of a gravitationally stratified atmosphere in which cooling is initially in balance with heating) that in order for a halo to not be locally thermally unstable, leading to condensation and driving star formation rates larger than observed, the cooling time must be at least ten times the dynamical time. This bound on the density of gas in halos has been confirmed in simulations with more realistic feedback prescriptions (Gaspari et al., 2013). It also is consistent with observations (Sharma et al., 2012; Voit & Donahue, 2015; Voit et al., 2017a).

We use the Sharma et al. (2012) fiducial model which uses a cooling time to dynamical time ratio of 10 (an upper limit on the core density and therefore on L_X) as an upper limit to our calculation and their lowest luminosity model with a cooling time to dynamical time ratio of 100 as a lower limit. These models, which produce $L_X^{\rm Sharma}$, generously bracket the spread in L_X-T_X values seen in observations (see Figure 3 of Sharma et al. 2012). Indeed, a more detailed analysis likely could shave off factors of two in the uncertainty at both sides. Both of these models use an asymptotic gas density slope of -2.25 to solve a differential equation for the gas density profile (see Sharma et al. 2012). We identify T_X with $T_{\rm vir}(M_{\rm halo})$, the virial temperature of a halo of mass $M_{\rm halo}$, calculated assuming an isothermal sphere (Barkana & Loeb, 2001).[7]

For the spectral form of this emission, $\ell(\nu) \equiv L_\nu / \int d\nu L_\nu$, we use a composite CLOUDY spectrum that is made up of a series of CLOUDY "coronal equilibrium" models with several discrete temperatures. These CLOUDY models assume collisional ionization equilibrium (Ferland et al., 2013) and a hydrogen density of 10^{-4} cm^{-3} – the virial density of halos in spherical collapse at $z = 0.2$. We use Solar abundance ratios of Grevesse et al. (2010) with an overall metallicity of $Z = 0.3\,Z_\odot$, in accord with the typical metallicity in intracluster and circumgalactic media measurements (Prochaska et al., 2017; Mantz et al., 2017). Changing to $Z = 0$ (or, to a lesser

---

[7] We note that the Sharma models are computed for just free-free cooling, which could lead to differences at the lowest temperatures we consider where atomic cooling becomes important. However, the CGM models become more applicable in this limit.

extent, turning on an ionizing background or decreasing the density we assume) results in the emission lines disappearing in the spectra, but do not significantly change our results.

The temperatures of these models are computed over a large range of virial temperatures. The models in the composite spectrum are then weighted in accordance to the Sheth-Tormen halo mass function (Sheth & Tormen, 1999), $\frac{dn}{dM}$, at a given redshift such that

$$\epsilon_\nu = \int_{M_{\rm min}}^{\infty} dM \frac{dn}{dM} L^M(\nu), \tag{3.5}$$

where $L^M(\nu)$ is the frequency-dependent luminosity of the halo gas of a given halo mass, set equal to $L_X^{\rm Sharma} \times \ell^{\rm cloudy}(\nu)$. We set $M_{\rm min} = 10^{13} M_\odot$ here, but smaller values would not change our results for ϵ_ν and J_ν (as discussed below) at $z = 0$.

Our fiducial model, shown as the red band in Figure 3.4, is this calculation for the $z = 0$ emissivity of halo gas, with the band bracketing the two $T_X - L_X$ models of Sharma et al. (2012) described above. The cyan band and gold band show this calculation above higher minimum masses as discussed in the following paragraph. If we treat the observed spread as an indication of measurement error (or, e.g., biases owing to missing the most diffuse components), then the band indicates the level of uncertainty. Interestingly, these estimates for virialized gas emission exceed our lower bounds for quasar emission between several tens and a few hundred eV. In contrast to the $z = 0$ emissivity, the observed background comes from a range of redshifts, and when this is considered we find in Section 3.3 that quasars are still likely the dominant source due to the declining abundance of massive halos at increasing redshift.

Most of the $z = 0$ emission from virialized gas comes from small clusters. Figure 3.4 also shows calculations that only allow for emission above halos with masses of $10^{14} M_\odot$ (cyan band) and $10^{15} M_\odot$ (gold band), respectively. We find that the EUV and soft X-ray emission from this gas is dominated by $M \gtrsim 10^{13} M_\odot$ at $z = 0$.[8]

Lower mass halos cool very efficiently and so have lower gas densities. In the Sharma et al. (2012) models, the gas in the most massive halos essentially traces the dark matter, but becomes

---

[8] Because the virial scale is an arc-minute for a $M = 10^{13} M_\odot$ halo at $z = 0.5$, these sources of emission would not be included in X-ray point source catalogues. Nearly every sightline on the sky intersects a $10^{13} M_\odot$ halo (McQuinn, 2014).

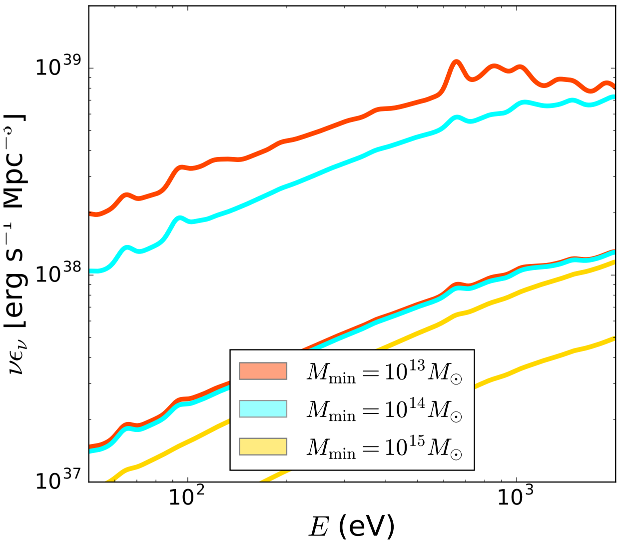

Figure 3.4: Specific emissivity of $z = 0$ virialized halo gas following the calculation described in § 3.2.5. The lower (upper) limit uses the models in Sharma et al. (2012) to relate the halo virial temperature and luminosity, assuming a cooling timescale to dynamical timescale ratio of 100 (10). These values are chosen to bracket observations. The red band is our fiducial model and represents a minimum halo mass of $10^{13} M_\odot$. The cyan and gold bands correspond to minimum masses of $10^{14} M_\odot$ and $10^{15} M_\odot$ respectively.

cored at lower masses with a large fraction does not fitting within in the virial radius for $M \lesssim 10^{13} M_\odot$. We caution that at $M \lesssim 10^{13} M_\odot$, representing the cooling emission with a virialized atmosphere may be fraught and the CGM calculations described previously likely hold more bearing.

3.3 the contribution of different sources to J_ν

The summary of the emissivity calculations described in Section 3.2 is shown in Figure 3.5. We plot each of the sources' specific emissivities at $z = 0.1$, 2.0, and 4.0. We use the quasar calculations described in Section 3.2.1, the XRB calculation of Section 3.2.2, the SSS calculation of Section 3.2.3, the ISM and CGM calculations as described in Section 3.2.4, the empirical galactic model with a power-law SED discussed in Section 3.2.2, and virialized halo gas calculation as described in Section 3.2.5. The band encapsulating each model reflects the range of possible values that we motivated.

Both the peak of the quasar emissivity and cosmic star formation rate (to which the XRB and CGM emissivity are tied) occur at $z = 2-3$, prompting a similar peak in each sources' emissivity near these redshifts. In contrast, the amount of free-free emission from virialized halo gas drops off rapidly with increasing redshift due to the abundance of $\gtrsim 10^{13} M_\odot$ halos decreasing quickly with redshift. While virialized gas likely is the most important source at most of the considered wavelengths at $z = 0$, quasars become the most important at $z = 2-4$. At higher redshifts than shown, models suggest that XRBs and perhaps hot ISM gas become the dominant source at $100-1000$ eV (Mirabel et al., 2011; Pacucci et al., 2014; Madau & Fragos, 2017). At $z \sim 0$ SSSs appear that they could most important galactic source at energies ~ 100 eV, although the upper limit that we estimate for their emissivity is likely extreme as discussed in Section 3.2.3.

The solution to the cosmological radiative transfer equation gives the background angular-averaged specific intensity at a particular energy as observed at z_0,

$$J_\nu(z_0) = \frac{c}{4\pi}\int_{z_0}^{\infty} dz \left|\frac{dt}{dz}\right| \frac{(1+z_0)^3}{(1+z)^3}\epsilon_\nu(z)e^{-\bar{\tau}(z_0,z,\nu)}, \tag{3.6}$$

where ϵ_ν is the proper volume emissivity – what we modeled in Section 3.2 for various sources –, $|dt/dz| = [H(z)(1+z)]^{-1}$, and $\bar{\tau}$ is the effective optical depth between z_0 and z in a nonuniform IGM, and given by

$$\bar{\tau}(E_0, z_0, z) = \int_{z_0}^{z} dz' \int_0^{\infty} dN_{\rm HI} f(N_{\rm HI}, z') \left(1 - e^{-\tau_\nu(N_{\rm HI})}\right), \tag{3.7}$$

for randomly distributed absorbers, where $f(N_{\rm HI}, z')$ is the H I column density distribution and $\tau_\nu(N_{\rm HI})$ is the optical depth at a particular energy through an absorber,

$$\tau_\nu = N_{\rm HI}\sigma_{\rm HI}(\nu) + N_{\rm HeII}\sigma_{\rm HeII}(\nu), \tag{3.8}$$

where σ_X is the photoionization cross section of species X, and the He II column of a system $N_{\rm HeII}$ must be modeled in terms of $N_{\rm HI}$. We use Equation A10 in Fardal et al. (1998) for the relationship

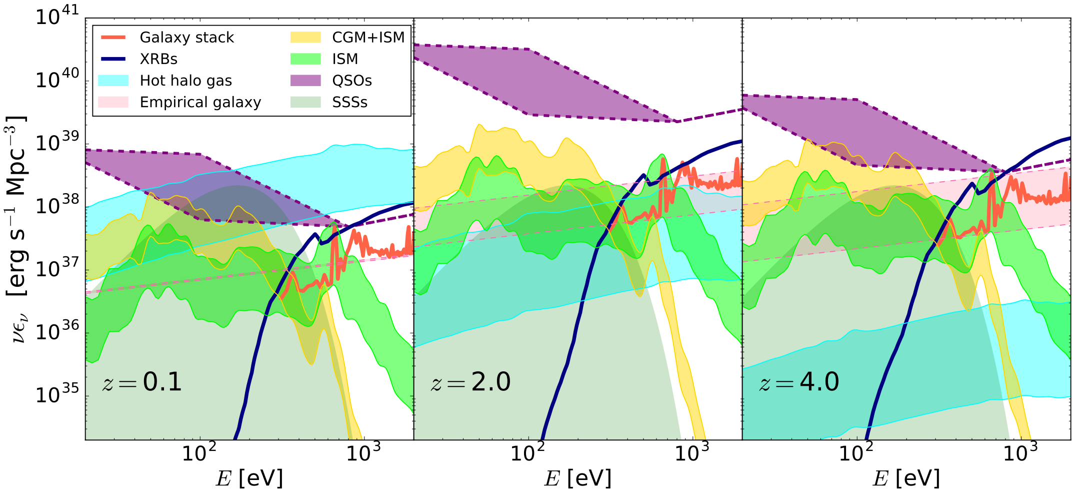

Figure 3.5: Estimated specific emissivities of the sources using the models described in Section 3.2. The purple shaded region shows quasar emissivity estimates from extrapolating into the EUV/soft X-ray with the range of mean power-law slopes that are estimated. The ISM/CGM are represented in the green and yellow bands, with $T_{\rm max} = 3 \times 10^6$ K and $T_{\rm max} = 1 \times 10^6$ respectively, with their spectra set to a resolution of 15 to smooth out lines. The cyan band represents the virialized hot halo gas described in Section 3.2.5. The dark blue SED represents the Fragos et al. (2013) XRB model. The red spectrum represents the empirical XRB model from stacked spectra, the light pink band the power-law extrapolation of galactic soft X-ray emission (whose width increases with redshift according to the allowed range of evolution in XRB emissions), and the dark green shaded area represents our upper bound on the unattenuated allowed emissivity of super soft X-ray sources.

between $N_{\rm HeII}$, $N_{\rm HI}$, $\Gamma_{\rm HI}$ for a single temperature and density slab. We assume 10^4K and a density set by the model in Schaye (2001) in which absorbers column and density are related by assuming the size of absorbers is the Jeans length and photoionization equilibrium. The Schaye (2001) model agrees well with simulations (McQuinn et al., 2011b; Altay et al., 2011). Our calculations neglect He I continuum absorption and resonant lines, which contribute relatively small features in J_ν compared the the H I and He II continuum absorption that we include.[9]

For $f(N_{\rm HI}, z)$, our calculations use the piecewise-in-$N_{\rm HI}$ fits of Prochaska et al. (2014), which use a parametrization of the form $f(N_{\rm HI}, z) = AN_{\rm HI}^{-\beta}(1+z)^\gamma$. While the error bars over the range of columns probed are generally quoted at the tens of percent level, there are some factor of two discrepancies around 10^{16}cm^{-2} (Prochaska et al., 2014). However, for the $z \sim 0$ background, the dilution from expansion and redshifting (which is perfectly captured) is more important than the continuum absorption of hydrogen. At $\gg 1$Ry, where we focus, this is true not just at $z \sim 0$ but also at higher redshifts. Therefore, discrepancies in the column density distributions may indicate there is room for as much as a factor of two difference from mean free path effects, but then likely only at the lowest energies considered and moderate redshifts. Even a factor of two is smaller than the possible amplitude ranges in all of our source models. Thus, our modeling of absorption is not the dominant source of uncertainty.

Figure 3.6 shows J_ν at $z = 0$ for each of the sources shown in Figure 3.5. We also include two observational constraints from *ROSAT*: The constraint of Warwick & Roberts (1998) using the lowest energies where the extragalactic background can be estimated is represented by the error bar at 250 eV, and the *ROSAT* PSPC data constraint of Georgantopoulos et al. (1996) is shown as the red bowtie starting at ~500 eV. By construction, both of these observational bounds are reasonably matched by the full range of quasar emissivity models.

Our calculations show that, even accounting for our estimated range of specific emissivities, quasars are the dominant contributor to the EUV/soft X-ray background at energies $\lesssim$100 eV. If

---

[9] Because the mapping of $N_{\rm HI}$ to $N_{\rm HeII}$ depends on J_ν, we must solve for J_ν iteratively. Additionally, we use the rates for our fiducial quasar model when calculating the generally subdominant contribution to J_ν from other sources models.

the value of $\alpha_{\rm QSO}$ is on the softer side as observations may suggest, then the emission of hot halo gas in massive halos could be the more important contributor to the EUV background at energies upwards of a couple hundred electron volts. Figure 3.6 suggests that galactic sources may be of secondary importance to these two sources where $E \geq 100$ eV, but the ISM and CGM may be second only to quasars at lower energies. Even though they are not the dominant sources of emission of the extragalactic background, they can dominate within the halos of galaxies (§ 3.5) and their contribution.

Potential background sources can be isolated using unresolved X-ray background measurements. In particular, the $1-2$ keV, resolved fraction of X-ray background is 80% of the total in the Chandra deep fields (a total of 0.06 sq. deg.), and similar constraints have been found in larger fields (Hickox & Markevitch, 2006). Thus, only $\approx 20\%$ of the X-ray background owes to diffuse sources like virialized halo gas. This bound suggests that the maximum virialized halo gas emission is a factor of ~ 2 below our maximum estimates. However, at $1-2$ keV, the signal is dominated by rare $> 10^{14} M_{\odot}$ halos (Fig. 3.4), which may not fall in the Chandra field of view. A more detailed analysis is necessary to understand this constraint.

Figure 3.7 shows J_{ν} for the same sources at $z = 2$. Here quasars are undisputedly the dominating source of the EUV/soft X-ray background. No other source is likely to produce enough > 54eV photons to doubly ionize the He II if it is ionized at $z \sim 3$ as observations suggest (McQuinn, 2016). The number of $M > 10^{13} M_{\odot}$ halos steeply declines with increasing redshift, and thus the contribution of virialized hot halo gas at $z = 2$ is negligible in comparison to the contribution of both quasars and galactic sources. The overall increase in the background intensity from $z = 0$ to $z = 2$ follows from the rise of both the cosmic star formation rate and quasar luminosity function.

3.4 the effect of the extragalactic background on IGM and CGM absorption line inferences

Photoionization models are used to infer the density and metallicities of intergalactic and circumgalactic absorption systems (e.g. McQuinn, 2016; Tumlinson et al., 2017). As ions have electronic binding energies in the EUV and soft X-ray, their abundances are shaped by these radiation back-

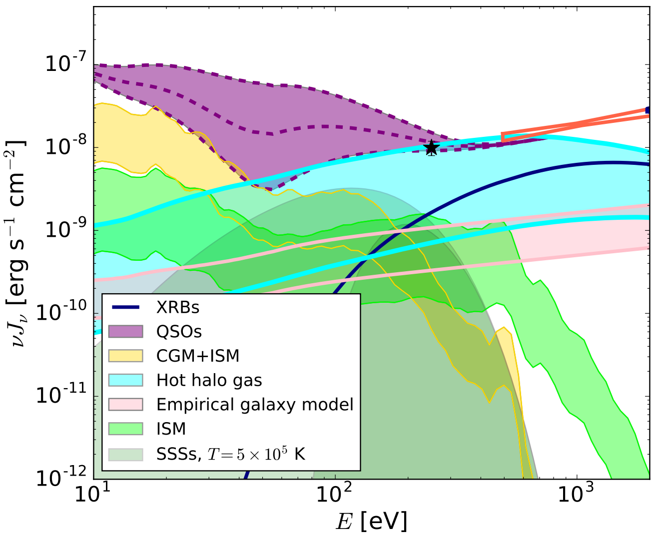

Figure 3.6: Angle-averaged $z = 0$ specific intensity, J_ν, of sources described in Section 3.2 and shown in Figure 3.5. The errorbar at $E = 250$ eV is the soft X-ray background intensity *ROSAT* measurement by Warwick & Roberts (1998). The red bowtie is *ROSAT* PSPC observations from Georgantopoulos et al. (1996). Despite observations suggesting that $\alpha_{\rm QSO}$ may be on the softer end, quasars likely dominate the background at energies $\lesssim$ 100 eV. Between one and several hundred electron volts, virialized hot halo gas may can become as important as quasars. Galactic sources such as XRBs, the ISM, and especially the CGM, can contribute at the tens of percent level.

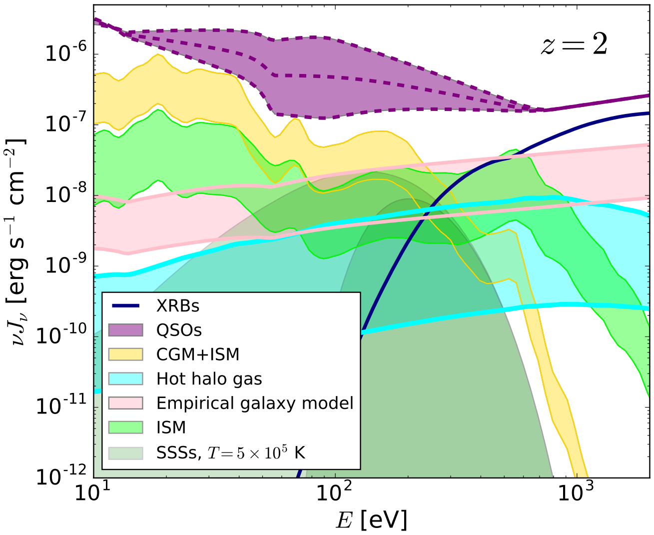

Figure 3.7: Angle-averaged $z = 2$ specific intensity, J_ν, of sources described in Section 3.2 and shown in Figure 3.5. At this redshift, quasars dominate the background at throughout the EUV and soft X-ray. Virialized hot halo gas is much less important than at $z = 0$ due to the declining abundance of $M > 10^{13} M_\odot$ halos.

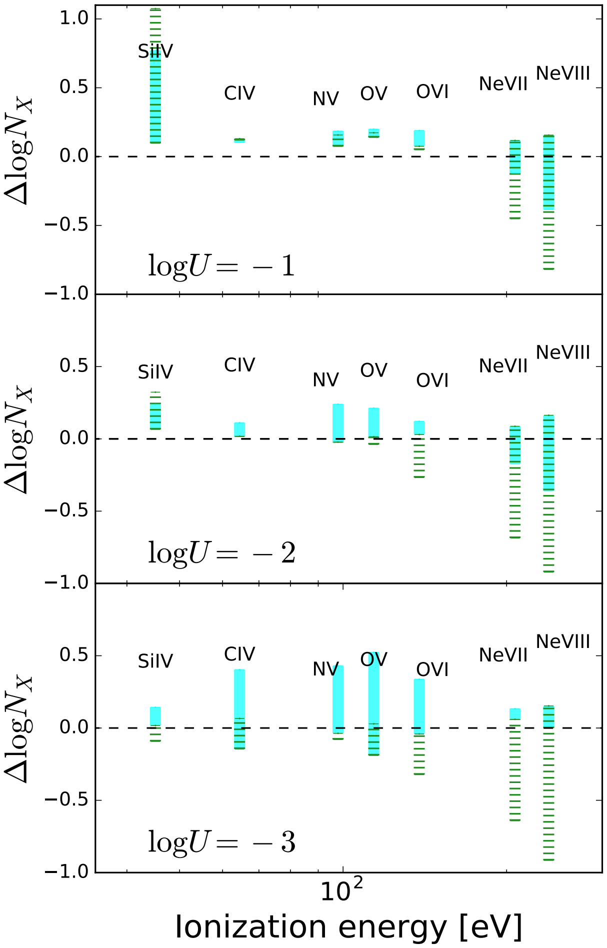

Figure 3.8: Error bars show estimates of column densities of several observationally relevant ions for the upper and lower limits of the J_ν range allowed, normalized to estimates using Haardt & Madau (2012) background model and ordered by ionization energy of the least bound electron. The top panel shows an ionization parameter, U, of 10^{-1}, the middle 10^{-2}, and the bottom panel shows $U = 10^{-3}$, which approximately correspond to $n = 10^{-5}\text{cm}^{-3}$, 10^{-4}cm^{-3} and 10^{-3}cm^{-3} for the Haardt & Madau (2012) model. The green dashed errors compare the differences at fixed U, and the cyan errors normalize the larger of our background models to a different U in a manner that matches at the H I photoionization rate of the smaller background model.

grounds. We have shown that the uncertainty in the spectrum of the background at these energies is considerable, suggesting commensurate uncertainties in the density and metallicity inferences. In this section, we apply our models to quantify the sensitivity of the most observable ions to the assumed ionizing background.

Previous attempts to make metallicity and density inferences from ionic absorption measurements use a metagalactic ionizing background model, such as Haardt & Madau (2012). When errors are quoted pertaining to the ionizing background choice, they are computed as the differences between historical models for these backgrounds, such as comparing how a calculation changes if it uses the Haardt & Madau (1996) rather than the Haardt & Madau (2012). The major differences between various historical models for the ionizing background is in improved constraints on IGM absorption and for the 1Ry emissivity of quasars, and not improved modeling of the spectrum of the sources. In contrast, our models allow for us to quantify the principle source of uncertainty.

We use CLOUDY to compute the equilibrium column densities of several common metal ions in the UV, with our J_ν models as the input ionizing spectrum and assuming temperature equilibrium. We only consider the range of J_ν in our quasar models, using the lower and upper envelopes of the quasar intensity. We then compare the resulting columns to the columns with the Haardt & Madau (2012) J_ν. These models implicitly assume that photoionization is dominant for all ionic species as the equilibrium temperature is $\sim 10^4$K. (Collisional ionization is included, but since our calculations use the equilibrium temperature these effects are generally small.) We vary the dimensionless ionization parameter, U, the ratio between the ionizing photon flux and the volume density of the gas. We choose $\log_{10} U = -1, -2,$ and -3, which approximately bracket the mean of values of U allowed by the data in Werk et al. (2014). For Haardt & Madau (2012), these correspond to densities of $8 \times 10^{-6} - 8 \times 10^{-4}\text{cm}^{-3}$, with larger $\log_{10} U$ corresponding to lower densities. However the precise density depends on the background model.

The dispersion from the range of models in select ions' column densities is shown in Figure 3.8. Here we show the difference between the CLOUDY column densities computed with the lower and upper limits of our quasar J_ν band and those of our CLOUDY calculations using the Haardt & Madau (2012) background model. (By only using the lower and upper parts of our band, we may underestimate range of expected columns if there are complex trends with J_ν in the ionic column.) The green bars represent the range of $J_{\nu_{\rm QSO}}$ in relation to the Haardt & Madau (2012) background model, $\log N_{X,\rm QSO} - \log N_{X,\rm HM12}$. The reason the midpoint of our errors is not centered at zero, the Haardt & Madau (2012) values, likely owes to our soft X-ray normalization being slightly lower than theirs. The larger $\log U$ are more applicable for the higher ionization state metal lines (e.g. NeVIII), and the smaller $\log U$ are more applicable for the low ionization state metal lines (e.g. SiIV). We set $N_{\rm HI} = 10^{15}$ cm^{-2} and the metallicity to $Z = 0.3Z_\odot$ in these calculations, but note that these are easily rescaled at fixed U to higher column or more metal-rich systems. For the model with the Haardt & Madau (2012) ionizing background, we find that with Log$U = -1$, the logarithmic column densities are {10.0, 13.8, 14.0, 14.9, 15.1, 14.4, 14.0} for [SiIV, CIV, NV, OV, OVI, NeVII, NeVIII], for Log $U = -3$ they are {12.1, 13.7, 13.1, 14.0, 13.3, 11.5, 10.4}, and for Log $U = -3$, the column densities are {11.7, 11.9, 10.2, 11.2, 9.5, 6.7, 4.9}. The dispersion in possible J_ν results in up to an order of magnitude in the uncertainty in the calculated column densities for the highest ions (Fig. 3.8).

While normalizing to a fixed U is standard practice in this field, normalizing to a fixed H I photoionization rate would better encapsulate the uncertainty in the ionization correction, as this fixes the background to the most constrained location, as Lyα forest measurements nail down the H I photoionization rate. While the green errors in Figure 3.8 compare the differences at fixed U, the cyan errors normalize the model that traces our upper envelope for the quasar J_ν to a different U such that it matches the H I photoionization rate of the lower envelope of J_ν model. Because this normalization fixes the background at a lower energy (near 13.6eV) compared to normalizing in U, this more physical normalization can sometimes result in more uncertainty, especially for the low ions. Indeed, most of the low ions show ≈ 0.3 dex variation. When fixing the H I photoionization rate, we find factors of $3 - 10$ errors in the ionization correction for all considered ions, which in turn reflects factor of $\sim 3 - 10$ uncertainties in density and metallicity inferences from IGM and CGM absorbers.

3.5 Proximity effects

The uncertainties in derived metal ion column densities in the previous section neglect the possibility that the ionization state of circumgalactic gas could be affected by the ionizing flux of the host galaxy. Within some radius, local galactic sources will dominate the cosmic EUV/soft X-ray background in ionizing photon flux. The low to mid ionization states of metals tend to arise in 10^4K gas, with their ionization states set predominantly by the photoionizing radiation background. Thus, knowledge of the UV background is critical for estimating the densities and metallicities of the clouds that these lower ions trace. For example, the inferred densities for these clouds using standard ionizing background models is an order of magnitude smaller than predicted by pressure equilibrium with the virialized phase (Werk et al., 2014, 2016; McQuinn & Werk, 2017). Modifications to the UV background have been hypothesized as a potential solution, likely requiring a $1-2$ order of magnitude enhancement from unknown sources at ~ 100eV (Werk et al., 2016). In addition, because highly-ionized metals are major coolants of gas in the CGM, order unity changes in their ionization fractions from local emissions translate to order unity changes in their cooling rates when the major coolants are predominantly photoionized, potentially impacting the rate at which galaxies are fed gas.

We compare the angular-averaged intensity from local galactic sources (i.e. ISM, XRBs, and SSSs) to that from the global background to determine the "proximity radius:" the distance from a galaxy where local and background sources contribute equally to the radiation. The proximity radius for a galaxy is given by

$$r_{\nu,\mathrm{prox}} = 103\ \mathrm{kpc}\ \left[\frac{([\nu L_\nu]/[10^{39}\mathrm{erg\ s^{-1}}])}{([\nu J_\nu]/[10^{-8}\mathrm{erg\ s^{-1}cm^{2}}])}\right]^{1/2} \tag{3.9}$$

where L_ν is the local galactic specific luminosity. We have evaluated the equation at a J_ν characteristic of our ionizing background calculations, and for an L_ν at the maximum of what we find in our galactic source models. Thus, we conclude that the proximity region is unlikely to extend beyond $\sim$ 100 kpc, a smaller extent then inferred for many absorbers in the CGM and especially

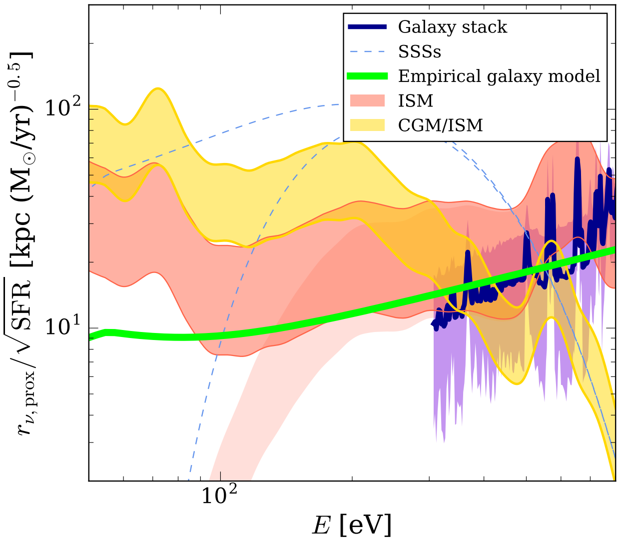

Figure 3.9: The proximity region radius for a galaxy with a SFR of 1 M$_\odot$ yr^{-1} at $z = 0.2$ for our galactic and circumgalactic source models, defined as the radius where the background J_ν is equal to the local contribution from galactic EUV and X-ray sources. The fainter ISM band represents the ISM model attenuated by a column of 10^{20} cm^{-2}. The two SSSs curves show the conservative upper limit of an unattenuated model as well as a model attenuated by a column of 10^{20} cm^{-2}. These SSS models scale with stellar mass rather than SFR, thus for these two models the y-axis becomes $r_{\nu,\mathrm{prox}}/\sqrt{M_\star}$. We have scaled them to a Milky Way stellar mass of $\sim 6 \times 10^{10}$ M$_\odot$. In Section 3.2.3 we state that the upper limits of SSS emissivity are likely extreme and thus these SSS curves probably drastically overestimate their proximity radii.

the O VI (Tumlinson et al., 2011; Prochaska et al., 2011; Johnson et al., 2015; Werk et al., 2016).[10] We note that this expression treats sources as if they are residing at $r < r_{\nu,\mathrm{prox}}$; this will generally *overestimate* the proximity radius in the case of emission extending beyond this radius (which may happen in the CGM).

Figure 3.9 shows our full calculations for the proximity radii in our models for $z = 0.2$, a redshift chosen to match COS-Halos L* galaxy CGM survey (Tumlinson et al., 2013). We show the galactic emission models described in Section 3.2.4, Section 3.2.3, and Section 3.2.2 for the

---

[10] See the appendix in McQuinn & Werk (2017) for generic arguments that the proximity region must have extent less than $\lesssim 100$ kpc.

specific luminosities, $L_{\nu,\mathrm{local}}$/SFR, excluding the SSS upper limits for which we give $L_{\nu,\mathrm{local}}$/M$_\star$ with a Milky Way stellar mass of $\sim 6 \times 10^{10}$ M$_\odot$. For the extragalactic background, we use our fiducial quasar model with a power-law index of $\alpha = 1.7$. In our source models, the proximity radius for a star-forming galaxy with a SFR of $\sim$ 1M$_\odot$ yr^{-1} varies between 10 and 100 kpc. Taking the median of our bands or the observed X-ray luminosities would suggest $\sim 10 - 30$ kpc, a small fraction of the total CGM, but scaling as (SFR)$^{1/2}$. Thus, proximity radiation changes the nature of cooling gas that resides fairly close to galaxies but does not affect the bulk of the halo gas with extent $\sim$ 100 kpc. Thus, local sources are unlikely to be dominant for the vast majority of absorbers in many CGM samples, such as in Tumlinson et al. (2011) and Stocke et al. (2013), whose absorbers mainly reside at $30 - 150$ kpc. That being said, proximity emission does substantially effect gas ionization near galaxies. This likely does not directly translate over to cooling in these smaller radii, as the denser cooling gas in interior of halo is more likely to be in collisional ionization equilibrium.

This conclusion is consistent with the geometric arguments of McQuinn & Werk (2017) that showed that $r_{\mathrm{prox}} \lesssim 100$ kpc, assuming that the proximity region sources are also the dominant source of the background. Our calculations add the likely-dominant background from quasar emissions, which reduces this radius further beyond the McQuinn & Werk (2017) estimates.

3.6 Conclusions

We have modeled the sources of the extragalactic background in the EUV and soft X-ray. In addition to the contribution from quasars, we included emissions that have so far been neglected in widely-used background models: X-ray binaries, the warm-hot interstellar and circumgalactic gas of star-forming galaxies, and virialized halo gas from groups and clusters. Our models are calibrated against the latest observational measurements to bracket the possible range of contribution from each of these sources. Note that these estimated ranges should be thought of as rough guidelines rather than rigorous bounds.

In agreement with previous studies, we find that quasars are likely the most important contributor to the ionizing background[11]. However, we also show that their contribution to the observationally elusive $20 - 500$ eV band can vary by up to a factor of 10 for plausible extrapolations into this band using power-laws derived in the far UV and soft X-ray. Furthermore, the evidence that the quasar SED is a single power-law, as assumed in previous background studies, is weak.

If quasars contribute at the lower envelope of our estimated J_ν range, we find that emissions from the galactic ISM/CGM, from virialized halo gas in groups/clusters, and possibly from super soft sources may contribute significantly to the background.

- The ISM contribution originates from cooling gas within stellar wind bubbles and supernovae blastwaves. While a large fraction of the ISM emission is absorbed by H I within the galaxy, a significant amount of stellar feedback energy is likely dumped as lower temperature gas and further away from obscuring H I in the ISM, venting into the CGM, where it is more easily radiated away. If most of the energy in stellar feedback is converted into background radiation, we find that the combined ISM/CGM contribution is roughly equal to the lower bound on quasars in the energy range $20 - 50$ eV.

- We also find that, at $z = 0$, emissions from hot, virialized gas in groups/clusters can be as important as quasars at energies of $\sim 100-1000$ eV. This contribution falls off in importance at higher redshifts owing to the decreasing abundance of groups and clusters, and to the increasing number density of quasars.

- Super soft sources have are often invoked as a huge unknown contribution at $\sim$ 100 eV, although there is little evidence for such a population. By deriving a much more stringent bound than previously bounds (from assuming that SSSs drive the Hα luminosity of elliptical galaxies), we show that unseen super soft sources could contribute tens of percent to the background at $\sim$ 100 eV.

---

[11] With the caveat that stellar emissions – which we do not model here – are likely to be important at < 50eV, with many models suggesting that they contribute up to a the factor of 2 level and are possibly dominant at $z \gtrsim 4$ (e.g., Haardt & Madau, 2012).

Disentangling the physics of circumgalactic gas with absorption line spectra requires accurate modeling of the EUV and soft X-ray backgrounds. Previous studies have estimated the effect of uncertainties in these backgrounds by comparing inferences obtained from different historical background models – for example, the Haardt & Madau (1996) and Haardt & Madau (2012) models. As an application of our work, we have used our range of J_ν models to quantify this uncertainty more rigorously. We bracketed the effect of the ionizing background on the inferred column densities of ions commonly identified in UV absorption line studies of the CGM. We showed that uncertainties in the average quasar spectrum alone are sizable, enough to introduce a few tenths of dex differences in the abundances of the most observationally important ions and up to 1 dex in the inferred column densities for the highest observationally-relevant ionization states. These differenes likely translate into comparable uncertainties in the densities and metallicities constrained by these ions.

The uncertainties in metal ionization corrections are even larger if local sources – e.g. XRBs and warm-hot ISM/CGM gases– contribute significantly. We estimated the EUV/soft X-ray proximity radius of a star-forming galaxy – the radius at which local emissions become equal to the extragalactic background. We found that this proximity radius is between $r_{\rm prox} \approx 10$ kpc and 100 kpc, assuming a star formation rate of $1\ M_\odot$ yr^{-1}, with $r_{\rm prox} \approx 100$ kpc for choices that maximize the potential galactic luminosity (and only at $E < 100$ eV). Thus, local emission is unlikely to be the dominant source of ionization for the absorbers in most extragalactic CGM samples.

Future observations and theoretical work has the potential to further constrain emission process that contribute sizably to the EUV and soft X-ray backgrounds. With a factor of $2-3$ improved sensitivity, diffuse soft X-ray background measurements would reach most of our model space for hot halo emission. In analogy to the γ-ray, where angular anisotropy analyses have constrained the blazar, millisecond pulsar, and galactic contributions (Ackermann et al., 2012), a future soft X-ray space telescope could measure the angular anisotropy to constrain source models: Low redshift clusters and groups are rare and have large arc-minute extents, whereas (abundant) galactic sources will contribute a smoother signal in angle. Finally, future CGM observations and modeling has the potential to better constrain the density and thermal structure of this medium and, hence, its cooling emissions.

PRUS thanks Nell Byler for helpful discussion.

Chapter 4

ESTIMATES FOR THE IMPACT OF ULTRAVIOLET BACKGROUND FLUCTUATIONS ON GALAXY CLUSTERING MEASUREMENTS

Material from this chapter was done in collaboration with Vid Iršič and Matthew McQuinn.

Spatial fluctuations in ultraviolet backgrounds can subtly modulate the distribution of extragalactic sources, a potential signal and systematic for large-scale structure surveys. While this modulation has been shown to be significant for 3D Lyα forest surveys, its relevance for other LSS probes has not been explored despite being the only astrophysical process that can affect clustering measurements on scales of $\gtrsim 1$ Mpc. We estimate that background fluctuations have a fractional effect of $\sim 0.1(k/[10^{-2}\mathrm{pMpc}^{-1}])^{-1}$ on the power spectrum of $z \sim 1-2$ 21cm intensity maps. We find a similar fractional effect for Hα and Lyα intensity mapping surveys (as a significant fraction of recombination radiation owes to absorptions from the ionizing background), but a much smaller effect for a traditional galaxy survey that correlates individual Hα or Lyα emitters. We also provide a rough estimate for the effect of backgrounds on low-redshift galaxy surveys in general, estimating a maximum fractional effect on the power of $\sim 0.03(k/[10^{-2}\mathrm{pMpc}^{-1}])^{-1}$ at $z = 1$ (based on fluctuations in ionizing background modulating the cooling of halo gas). In all cases, the effect of ionizing backgrounds likely increases with redshift. The sizes of these imprints tend to be smaller than cosmological parameter benchmarks for the next generation of LSS surveys; we focus in particular on squeezed triangle non-Gaussianity, finding that ionizing backgrounds could results in a bias of $\Delta f_{\mathrm{NL}} \sim 0.3$ for power spectrum measurements with for a SPHEREx-like galaxy survey.

4.1 Introduction

Radiation backgrounds, especially of the ionizing sort, have the potential to impact structure in the Universe on larger scales than any other non-gravitational, astrophysical process. The photons in these backgrounds can travel significant fractions of the Hubble length (Meiksin & Madau, 1993; Haardt & Madau, 1996, 2012), and, with their ability to ionize neutral hydrogen and alter the cooling rates of ions, they can modulate the properties of extragalactic sources (Benson et al., 2002; Hambrick et al., 2009). Despite this large-scale impact, the effect of background fluctuations on various large-scale tracers has not been investigated. This paper estimates how ionizing background fluctuations impact post-reionization 21cm intensity mapping surveys, Lyα and Hα emitter surveys, and galaxy surveys in general.

Detecting the imprint of these fluctuations on large scale structure (LSS) surveys would constrain the properties of the sources, such as fraction of the ionizing background that owes to quasars versus galactic emissions (e.g., Madau & Haardt, 2015). In addition, an imprint from background fluctuations in LSS surveys could complicate cosmological parameter constraints on, e.g., neutrino masses, the scalar spectral tilt plus its running, or primordial non-Gaussianity – meeting motivated benchmarks for all of these requires sub-percent precision on clustering measurements. Ionizing backgrounds have already been shown to be an important systematic for extracting cosmological parameters from 3D Lyα forest observations (Pontzen, 2014; Gontcho et al., 2014). We investigate here whether ionizing background fluctuations could also be relevant for other LSS measurements.

This paper is organized as follows. Section 4.2 describes how the ionizing background affects linear scales in LSS measurements, and Section 4.3 outlines the formalism used to calculate the spectrum of ionizing background fluctuations and presents a few models for the ionizing background power spectrum. In Section 4.4, we estimate the impact of background fluctuations on post-reionization 21cm intensity mapping surveys. Section 4.5 presents similar estimates but for surveys that view galaxies by either their Lyα or Hα emission. Section 4.6 considers the effects of ionizing background inhomogeneities on galaxy surveys in general. Finally, Section 4.7 compares to the requirements for constraining targeted cosmological parameters to benchmarks values, a particularly interesting one being squeezed triangle non-Gaussianity to $\Delta f_{\rm nl} = 1$.

4.2 The impact of intensity fluctuations on galaxy clustering

Metagalactic intensity fluctuations have a component that traces the density fluctuations with transfer function $T_J(k, w_\nu)$ and a stochastic (or 'shot') component $n_J(k, w_\nu)^{-1}$, where w_ν indicates some frequency-weighting of the radiation background. Thus, the linear power spectrum of intensity fluctuations is given by

$$P_J(k) = T_J(k, w_\nu)^2 P_{\delta_L}(k) + n_J(k, w_\nu)^{-1}, \tag{4.1}$$

where $P_{\delta_L}(k)$ is the linear matter power spectrum. In Section 4.3 we discuss how T_J and n_J are computed. For larger wavenumbers than the mean free path, T_J^2 and n_J^{-1} decrease as k^{-2}, resulting in the impact of ionizing backgrounds being largest at low wavenumbers.

Our concentration is not the nature of fluctuations, P_J itself, which was investigated in detail in Meiksin & McQuinn (2018) and whose calculation we briefly summarize below. Instead, our focus is the imprint that J fluctuations have on LSS surveys. When including intensity fluctuations, the standard expression for the linear power spectrum of some galaxy population is extended to

$$P_g(\boldsymbol{k}) = \left(b_g + b_J T_J + f\mu^2\right)^2 P_{\delta_L} + b_J^2 n_J^{-1}, \tag{4.2}$$

where $\mu \equiv \hat{\boldsymbol{n}} \cdot \boldsymbol{k}$, $\hat{\boldsymbol{n}}$ is the line-of-sight unit vector, $f \approx \Omega_m(z)^{0.6}$ and the associated term arises from redshift space distortions (Kaiser, 1987), and b_g (b_J) are the linear density bias (intensity bias) of the particular galaxy population. (We have ignored that the b_J coefficient could be different between the Poissonian and density-tracing terms, a distinction discussed below.) Equation 4.2 omits the shot noise from the surveyed galaxies themselves. Since b_J sets the magnitude of intensity fluctuations, much of the focus of this study is on estimating this bias for different types of galaxy survey. Our estimates of b_J from Sections 4.4- 4.6 are shown in Table 4.1 in addition to our estimates of fractional changes in power from intensity fluctuations.

---

[1] The estimated intensity bias for galaxy surveys is far less certain than H I or recombination line surveys because we do not have a predictive model that connects the ionizing background to galactic properties. This b_J estimates is for $L_\star$ galaxies and assumes that the cooling of the circumgalactic medium is tied to star formation (see § 4.6).

Table 4.1: The impact of J fluctuations on different surveys, where b_J is our estimated response of the survey to a fluctuation in Γ.

survey	redshifts	b_J	fractional change in power from J-fluctuations
21cm intensity mapping	$1, 2$	$0.2 - 0.25$	$\sim [0.03, 0.1](k/[10^{-2}\mathrm{pMpc}^{-1}])^{-1}$
Hα or Lyα intensity mapping	$1, 3$	0.1	$\sim [0.005, 0.1](k/[10^{-2}\mathrm{pMpc}^{-1}])^{-1}$
Galaxy surveys	$0.5, 2$	$\sim 0.05^1$	$\sim [0.002, 0.02](k/[10^{-2}\mathrm{pMpc}^{-1}])^{-1}$

4.3 The linear theory of ionizing radiation backgrounds

On megaparsec scales and greater, fluctuations in the $z \lesssim 5$ ionizing background are small and, hence, well suited for perturbation theory. While the fluctuations are small, they may still be a relevant driver of inhomogeneity for large-scale structure (LSS) surveys. Aside from the Lyα forest, this source of inhomogeneity has not been previously considered. This section discusses our calculation of the linear power spectrum of intensity fluctuations, with our approach following the spirit of the calculations for intensity fluctuations of earlier studies (Meiksin & White, 2004; Croft, 2004; McDonald et al., 2005; McQuinn et al., 2011a; Pontzen, 2014; Gontcho et al., 2014; Pontzen et al., 2014), based on the formalism presented in Meiksin & McQuinn (2018). Future sections use these calculations to estimate the imprint on various LSS surveys.

To proceed, we linearize and then solve the cosmological radiative transfer equation, given by

$$\frac{\partial I_{\nu_0}}{\partial t} + 2\frac{\dot{a}}{a} I_{\nu_0} + a^{-1}\, \hat{\boldsymbol{n}} \cdot \nabla I_{\nu_0} = -\kappa_\nu I_{\nu_0} + j_{\nu_0}, \tag{4.3}$$

where $\nu_0 \equiv \nu/(1+z)$, I_ν is the specific photon number intensity [photons $\mathrm{Hz}^{-1}\mathrm{s}^{-1}\mathrm{cm}^{-2}\mathrm{sr}^{-1}$], a the cosmic scale factor, κ_ν and j_ν the absorption and emission coefficients, and we have set $c = 1$ for simplicity.

Linearizing this equation in the intensity fluctuation $\delta I_{\nu_0} \equiv I_{\nu_0} - \bar{I}_{\nu_0}$ and going to Fourier space yields

$$\begin{aligned} \dot{\widetilde{\delta I_{\nu_0}}} \quad -ia^{-1}\hat{\boldsymbol{n}}\cdot\boldsymbol{k}\,\widetilde{\delta I_{\nu_0}} + (\bar{\kappa}_{\nu_0}+2H)\,\widetilde{\delta I_{\nu_0}} \\ = \tilde{\beta}_0 + \beta_\delta\tilde{\delta} + \beta_\Gamma\tilde{\delta}_\Gamma; \qquad (4.4) \\ \beta_\delta(\nu,t) \equiv \bar{j}_\nu\, b_{j,\delta} - \bar{\kappa}_\nu \bar{I}_\nu b_{\kappa,\delta}, \\ \beta_\Gamma(\nu,t) \equiv \bar{j}_\nu b_{j,\Gamma} - \bar{\kappa}_\nu \bar{I}_\nu b_{\kappa,\Gamma}, \end{aligned}$$

where tildes indicate the field's Fourier dual and we have also expanded the absorption and emission coefficients to linear order in their overdensities in the density and in the photoionization rate, namely $\kappa_\nu = \bar{\kappa}_\nu\,(1 + b_{\kappa,\delta}\delta + b_{\kappa,\Gamma}\delta_\Gamma)$ and $j_\nu = \bar{j}_\nu\,(1 + b_{j,\delta}\delta_S + b_{j,\Gamma}\delta_\Gamma)$, plus a stochastic field $\beta_0(\boldsymbol{x})$ from uncorrelated small-scale structure. The H I photoionization rate is most relevant for most of the modulating effects of the ionizing background (as essentially it modulates the opacity and recombination emission), justifying only expanding the background in terms of $\delta\Gamma$ rather than the more general expansion in δJ_ν. While formally (in addition to $t,\ \nu$) the β_X can depend on angle if there is anisotropic emission from sources, we will assume isotropy. Anisotropy enters into the stochastic contribution to fluctuations n_J^{-1} (Suarez & Pontzen, 2017), which we find is generally subdominant to the density tracing terms.

We further assume that quasars dominate the ultraviolet background, consistent with the findings of most background models at $z \lesssim 3$ (Meiksin & Madau, 1993; Haardt & Madau, 2012; McQuinn & Worseck, 2014; Upton Sanderbeck et al., 2017), although a dominant galactic contribution would only have an $\mathcal{O}(1)$ effect on our estimates.[2] To model quasars, we use the 1 Ry quasar emissivity of Haardt & Madau (2012), and we assume that their spectral index in specific intensity is $\alpha_Q = -1.7$. For the quasar bias, we linearly interpolate between $b_{j,\delta} = \{0.5, 1.1, 1.5, 1.8, 2.2\}$ at $z = \{1.4, 1.8, 2.1, 2.6, 3.0\}$, numbers based on quasar SDSS clustering measurements (Ross et al., 2009; Laurent et al., 2017). We further assume that $b_{j,\delta} \propto a$ to extrapolate to higher redshifts. While these bias measurements are for the $> L_*$ quasars observable with BOSS, we note

---

[2] In the general case of both galaxies and quasars, the amplitude would instead be set by the bias of both populations weighted by their fractional contribution (because we find the density tracing term is dominant over the Poissonian, even for rare quasars).

that in many models for quasar clustering the luminosity dependence is weak (Lidz et al., 2006). We further take the shot noise to be dominated by quasars for which the effective number density $\bar{n} \equiv [\int dL\phi(L)L]^2/[\int dL\phi(L)L^2]$, where $\phi(L)$ is the full redshift evolution quasar luminosity function of Hopkins et al. (2007).[3]

For the opacity coefficient, we use $\kappa_\nu = 0.027[(1+z)/5]^{-5.4}(\nu/\nu_{\rm 1Ry})^{-1.5}$ physical Mpc^{-1}, for which the coefficient is the fit of Worseck et al. (2014) to $z = 2.3 - 5.5$ for $\nu = \nu_{\rm 1Ry}$ and we have assumed the expected scaling with ν for an H I column density distribution with slope of $\beta = -1.5$. At lower redshifts than $z \approx 2$, opacity effects become unimportant as the propagation of radiation backgrounds becomes limited by the Horizon and so we use this fit even beyond its intended redshift range. We take the response of the opacity to the ionizing background to be $b_{\kappa,\Gamma} = 0.5$. This value is consistent with an anlytic models based on Miralda-Escudé et al. (2000) for $\beta = -1.5$ and what is directly measured from simulations at $z \sim 2-4$ (McQuinn et al., 2011a).[4]

The remaining bias coefficients $b_{\kappa,\delta}$ and $b_{j,\Gamma}$, are set to zero. Setting $b_{\kappa,\delta}$ to zero is justified because the sources are more biased than the absorbers. The limit $b_{j,\Gamma} = 0$ is applicable if the photoionization rate does not have a significant effect on modulating the emission: models find associated recombinations contribute at the $10-20\%$ level to the ionizing background (Faucher-Giguère et al., 2009).

To solve for δ_Γ, we can average Equation 4.4 over frequency with weighting $w_\nu = \sigma_\nu$, where σ_ν is the frequency-dependent photoionization cross section, and angle, using that the average background scales as $\bar{I}_\nu \approx \nu^{-\alpha_{\rm bk}}$ where $\alpha_{\rm bk} = \alpha_Q - (3\beta - 3)$. This scaling is most relevant when $\kappa \ll H$, which holds at $z \gtrsim 2$. This choice will result in an underestimate of the intensity power at lower redshifts. We indicate σ_ν–averaged coefficients with a subscript σ.

---

[3] See Meiksin & McQuinn (2018) for a discussion of observational uncertainties in $\bar{n}$, who finds that it is relatively well constrained at the redshifts of interest (unless the bright-end is fit with a power-law and extrapolated to unphysically high luminosities).

[4] The parameter $b_{\kappa,\Gamma}$ enhances the amplitude of fluctuations by $(1-b_{\kappa,\Gamma})^{-1}$ on scales larger than the mean free path when opacity matters ($z > 2$), leading to at most a factor of 2 enhancement for the cases we consider. We note that Pontzen (2014) used a value of $b_{\kappa,\Gamma} = 0.9$ that is inapplicable to the IGM at considered redshifts, which results in a much more significant enhancement.

Noting that the angular-averaged Green's function for the right hand side of the resulting equation is $j_0(k\eta_{t,t'})\exp[-\int_{t'}^{t} dt''\bar{\kappa}_{\mathrm{eff},\sigma}(t'')]$, where $\eta_{t,t'} = \int_{t'}^{t} dt''/a''$ and $\bar{\kappa}_{\mathrm{eff},\sigma} \equiv (2+\alpha_{\mathrm{bk}})H + \Gamma^{-1}\int d\nu\sigma_\nu \bar{I}_\nu \bar{\kappa}_\nu$, and ignoring fluctuations in the spectral index of the background on δ_Γ, the solution to the spatial Fourier transform of this equation can be written in terms of the following transcendental equation

$$\begin{aligned}\tilde{\delta}_\Gamma(t) \quad &= \int_0^t dt' j_0\left(k\eta_{t,t'}\right)\exp[-\int_{t'}^{t} dt''\bar{\kappa}_{\mathrm{eff},\sigma}(t'')] \\ &\times \left[\tilde{\beta}_{0,\sigma} + \beta_{\delta,\sigma}\tilde{\delta} + \beta_{J,\sigma}\tilde{\delta}_J\right].\end{aligned} \tag{4.5}$$

This equation can be solved for δ_Γ by discretizing the first integral in Equation 4.5 and some matrix algebra (Meiksin & McQuinn, 2018). Symbolically,

$$\tilde{\delta}_{J,i} = M_{iq}\tilde{\delta}_{S,q}, \tag{4.6}$$

where i indexes time, M_{iq} describes how the ionizing background at time i is sensitive to emission at time q, and there is summation over repeated indices. We have grouped the stochastic and δ-tracing components of the sources into this one source overdensity, δ_S. The power spectrum of Γ fluctuations $P_J = |\tilde{\delta}_J|^2$ follows as

$$P_J(k|t_i,t_q) = M_{il}P_S(k|t_l,t_m)M^T_{mq}, \tag{4.7}$$

where the power spectrum of the ionizing sources is given by

$$P_S(k|t_l,t_m) = b_{j,\delta}(t_l)b_{j,\delta}(t_m)P_\delta(k,t_l,t_m) + \bar{n}^{-1}\mathcal{L}(t_l - t_m), \tag{4.8}$$

where $P_\delta(k|t_l,t_m)$ is the linear matter power at times t_l and t_m, and $\mathcal{L}$ is the convolution of the source light curve with itself. For simplicity, we assume quasars sources with top hat light curves with widths of $10,\ 100$, and ∞ Myr. The former two values reflect the range of estimates based on direct and indirect probes (Martini & Weinberg, 2001).

For all of our calculations we will weight the specific photon number intensity by the photoionization cross section, $w_\nu = \sigma(\nu)$, such that we can use the above directly and not also solve for additional weightings. Often the photoionization weighting makes the most physical sense.

However, we do consider a case when it does not, for metal line cooling (where we should weight energies near the ionic binding energies of the prominent ions), and will address the applicability of our models

Figure 4.1 shows the results of the power spectrum of photoionization rate overdensity, δ_Γ, fluctuations at $z = 0.5,\ 1,\ 2,$ and 3 for the different lifetime models. The solid black curves are the density power spectrum, whose value (to order-unity density bias factors) indicates the level of fluctuations in LSS surveys. The dashed blue curves are the density tracing component of the model (which do not differ between lifetime models). The dotted curve is the cross power between the density tracing (clustered) component and the the density, the ionizing background term that often makes the largest imprint galaxy clustering. The amplitude of fluctuations in the radiation background increases with redshift. Even at low redshifts, the fluctuations can be larger than the density fluctuations for the horizon-scale modes that are of much interest for primordial non-gaussianity searches.[5] The importance of ionizing background fluctuations for LSS surveys depends on the bias with which these surveys trace the background fluctuations, b_J. The ensuing sections estimate b_J for several surveys.

4.4 21cm intensity mapping surveys

Many efforts are coming online to detect post-reionization redshifted 21cm emission from the residual H I gas that is trapped in and around galaxies. Namely, the CHIME and HIRAX experiments are targeting diffuse 21cm emission from $z = 0.8 - 2.5$ (Bandura et al., 2014; Newburgh et al., 2016b), and MEERKAT is targeting $z = 0.4 - 1.4$. BINGO and FAST could extend the range of redshifts probed to $z = 0$ (Battye et al., 2012; Bigot-Sazy et al., 2016), and mapping all the way to reionization is also possible. The capstone project is the Square Kilometer Array (Carilli & Rawlings, 2004; Kovetz et al., 2017).

Fluctuations in the ionizing background will modulate the distribution of H I: Regions with

---

[5] The effect of radiation background for modes with $k \lesssim H^{-1}$ should be calculated in full General Relativity for (gauge independent) observables (as has been done for galaxy surveys; Yoo et al. 2009), which has not been done here. However, we do not expect predictions for the size of effects to be altered (see Pontzen 2014).

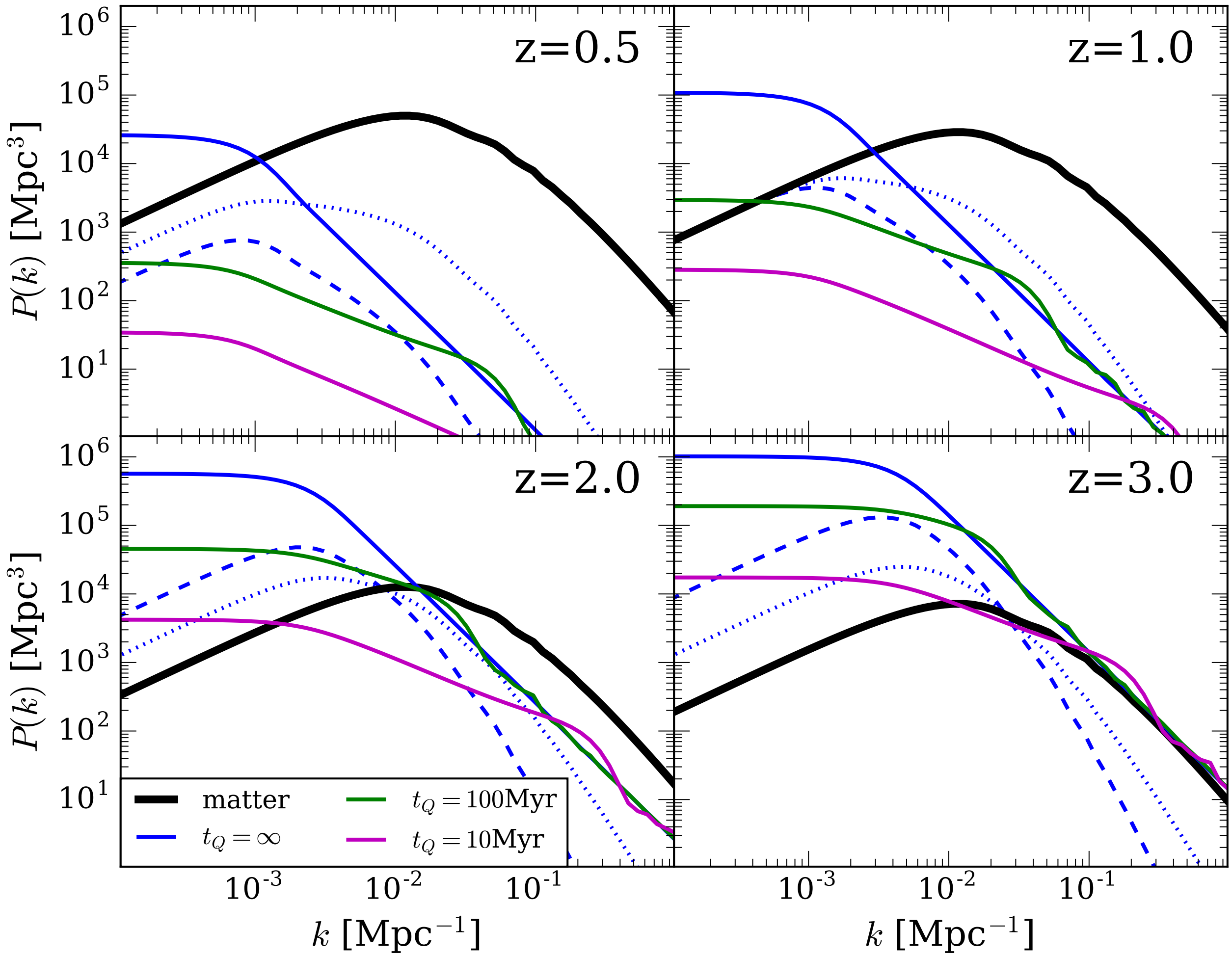

Figure 4.1: Models for the power spectrum of the photoionization rate overdensity, P_Γ, at the specified redshifts. The colored curves show the shot noise contribution to P_Γ for different quasar lifetime models. The dashed blue is the clustered component of P_Γ, which does not depend on the quasar lifetime. For reference, the solid black curve is the matter overdensity power spectrum. The dotted curve is the cross power between the density tracing (clustered) component and the the density, the ionizing background term that often makes the largest imprint galaxy clustering.

a larger ionizing background self-shield at higher densities and, hence, retain less H I. Cosmological simulations post-processed with ionizing radiative transfer have been found to successfully reproduce the H I column density distribution (Altay et al., 2011; McQuinn et al., 2011a; Rahmati et al., 2013). Such simulations can be used to estimate the response of H I to the background by post-processing simulations with different backgrounds and observing the change in H I. We can in-effect do such a calculation by using the physically-motivated fitting formulae in Rahmati et al. (2013) that describe the density dependence of the H I fraction in their radiative transfer simulations. Using these formulae, we find a factor of $x \ll 1$ fractional change in the background results in a factor of $-0.25x$ change in the global amount of neutral hydrogen (at $z = 3$). This estimated response does not depend on redshift to good approximation (being invariant to the extent that the column density distribution is invariant). The details of the Rahmati et al. (2013) formula and this calculation are presented in Appendix A. This response translates to the intensity bias, $b_J = -0.25$ (see eqn. 4.2).

In addition to deriving b_J from the relations in Rahmati et al. (2013), we have two other methods for estimating b_J for 21cm intensity mapping surveys that result in similar values. Each of these methods make different assumptions. In one, we perform radiative transfer on a slab of a given H I column with width corresponding to the Jeans scale at a specified density, assuming a temperature of 10^4 K (see Appendix 4.9.2). This Jeans-scale ansatz is motivated by the arguments in Schaye et al. (2000) and by the densities of absorbers in cosmological simuations (Altay et al., 2011; McQuinn et al., 2011b), and it results in a one-to-one relation between H I column density and density. The motivation for this slab calculation is that it more explicitly tracks the ionization physics that is hidden in the Rahmati et al. (2013) fitting formulae (at the expense of the simplified geometry). We find that a factor of x fractional change in the ionizing background results in a factor of $-0.20\,x$ change in the global amount of neutral hydrogen, consistent with our previous estimate. Finally, one can do a simple estimate assuming that all absorbers have the same power-law profile and self shield at a critical density (Miralda-Escudé et al. 2000; McQuinn et al. 2011b; see Appendix 4.9.3). This model has been found to have some success at reproducing the shape of the observed column density distribution (Zheng & Miralda-Escudé, 2002). For a power-law index that results in an H I column density distribution with $\beta = 1.3(1.5)$ in the optically thin limit, this model results in a response of -0.45 (-0.75) – again suggesting a large response. The estimated value of b_J is redshift independent in the latter two estimates (and this holds to a good approximation in the first estimate based off Rahmati et al. 2013).

In addition to the intensity bias, b_J, to compute the amplitude of fluctuations also requires an estimate of the H I density bias, b_g. At $z = 0.8$, the Switzer et al. (2013) 21cm-galaxy cross-correlation measurement of $\Omega_{\rm HI} b_g = [0.62^{+0.23}_{-0.15}] \times 10^{-3}$ combined with the quasar absorption line measurements of $\Omega_{\rm HI} = 0.5 \times 10^{-3}$ yields $b_g = 1 \pm 0.3$. At $z = 2.1$, DLA clustering measurements find $b_g = 2.0 \pm 0.1$ (Font-Ribera et al., 2012; Pérez-Ràfols et al., 2018). There are currently no measurements of b_g at higher redshifts, thus for our calculations at $z = 3$, we assume $b_g = 2$.

Figure 4.2 shows the expected 21-cm flux power spectrum at $z = 1$ and $z = 2$ with ionizing background fluctuations for models with quasar lifetimes of $t_Q = 100$ Myr and $t_Q = \infty$. We use our most detailed intensity bias based on Rahmati et al. (2013), which yields $b_J = -0.25$. The solid curves are the total contribution to the galaxy clustering power spectrum from intensity fluctuations, whereas the dashed curves are the contribution excluding shot noise (which depends on quasar lifetimes). The residual power spectrum of the models that exclude shot noise scale as approximately k^{-1} as these background fluctuations are tracing density and so the $2T_J P_\delta$ term dominates where $T_J \sim k^{-1}$ at $k \gg \bar{\kappa}_{\rm eff,\sigma}$. This clustering component is comparable to the shot noise at the lowest and highest wavenumbers shown, most notably for the $z \sim 3$ case. The lowest wavenumbershown are difficuult to measure by 21cm efforts due to foreground removal; foreground removal limits HIRAX to measurements at $k \gtrsim 0.03^{-1}$ where the contribution is less than $10^{-3},\ 10^{-2}$ and 0.05 at $z = 1,\ 2$ and 3 (Newburgh et al., 2016a).

4.5 recombination line surveys

Most recombination-line emissions originate from recombinations in the ISM of galaxies that result from ionizing photons from nearby stars. However, at $1 \lesssim z \lesssim 3$ Type I AGN produce about 10% of all ionizing photons, with stars producing the rest (e.g. Haardt & Madau, 2012). Because most if not all of Type I AGN photons escape their host galaxies, but those of stellar origin likely do

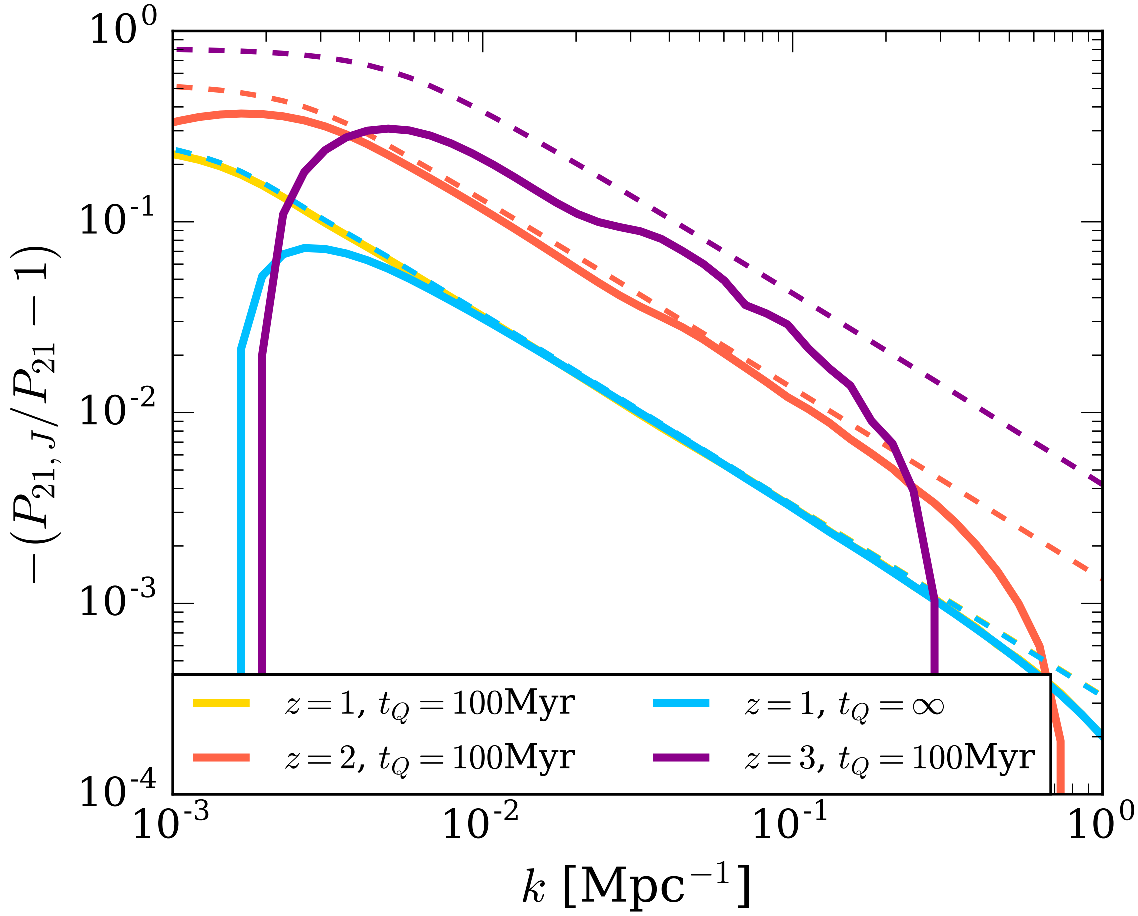

Figure 4.2: Predictions for the fractional impact of ionizing background fluctuations on the angularly-averaged power spectrum of the diffuse 21cm intensity, computed using $b_J = -0.25$. The solid curves are the negative of the total fractional contribution to the power from intensity fluctuations, and the dashed are the same but excluding the shot noise contribution to background fluctuations. The shot noise component becomes increasingly important with increasing redshift and increasing quasar lifetime. Note, foreground removal in 21cm experiments will likely prevent measurements at $k \lesssim 0.03$ Mpc^{-1} (Newburgh et al., 2016a).

not, this suggests that $\sim 10\%$ of recombinations are tied to the ionizing background in the steady state limit in which recombinations are in global balance with emissions (which holds at $z \gtrsim 3$). Large-scale structure surveys that probe recombination lines, such as H I Hα and H I Lyα, could then trace the ionizing background at the 10% level.

There are several upcoming Lyα and Hα surveys whose cosmological determinations could be biased by these fluctuation-tracing recombinations. HETDEX aims to constrain the Cosmology from the clustering of Lyα emitters at $1.9 < z < 3.5$ (Hill et al., 2008), and SPHEREx – a proposed NASA Medium-class explorer satellite that is funded for concept studies – aims to detect Hα emission from galaxies with from much of the Cosmic Volume (Doré et al., 2016). HETDEX and SPHEREx will undertake both 'traditional' galaxy surveys and intensity mapping campaigns (with the latter defined as surveys that map all the emissions and do not locate individual sources). The effect of ionizing backgrounds is largest for intensity mapping surveys as traditional galaxy surveys likely exclude much of the (diffuse) background-sourced recombination radiation (see below).

Both Lyα and Hα emission signals owe mainly to recombinations. To estimate the size of the background-tracing emissions in these lines, let us decompose emissions into an internal component – driven by ionizing photons absorbed before they escape their host ISM and the subsequent recombination – and an external component – driven by ionizing photons in the extragalactic ionizing background,

$$\begin{aligned} j_{\rm rec} &= j_{\rm rec,int} + j_{\rm rec,ext}, \\ &= \bar{j}_{\rm rec,int}(1+\delta_g) + \bar{j}_{\rm rec,int}(1+\delta_g + b_\Gamma \delta_\Gamma), \end{aligned} \tag{4.9}$$

In the first line, $j_{\rm rec,int}$ and $j_{\rm rec,ext}$ are the internal emission coefficient and external (background-sourced) emission coefficient for the desired recombination line. The seconds line expands the two emission sources into an overdensity that traces the sample galaxies, $\delta_g \equiv (b_g + f\mu^2)\delta$ and, for the external coefficient, an overdensity that traces the ionizing background δ_Γ with bias b_Γ. To the extent that the cross sections of absorbers are unchanged by the ionizing background, $b_\Gamma = 1$ – the value we adopt for our calculations.

The internal emission coefficient is proportional to the rate of ionizing photons produced that are absorbed in the ISM (likely close to 100%) and the background sourced proportional to the number of absorptions and reemissions of extragalatic ionizing photons that are picked up by the survey:[6]

$$\bar{j}_{\rm rec,int} = f_{\kappa,g}\bar{\kappa}_\sigma\bar{\Gamma}.$$

The parameter $f_{\kappa,g}$ is the fraction of the fraction of opacity for metagalactic ionizing photons that arises from regions within the survey aperture and not from other systems (see below). This parameter equals unity for intensity mapping surveys.

From Equation 4.9, we can compute the galaxy power spectrum for a luminosity-weighted galaxy clustering measurement and also an intensity mapping survey:

$$\begin{aligned} P_{\rm rec}(k) &= \left[(b_g + f\mu^2) + f_{\rm ext}b_\Gamma T_J\right]^2 P_{\delta_L}(k) \\ &+ f_{\rm ext}^2 b_\Gamma^2 n_J(k,\nu)^{-1}. \end{aligned} \tag{4.10}$$

where, to connect to our previous notation (c.f. eqn. 4.2), $b_J = f_{\rm ext}b_\Gamma$ and we have defined $f_{\rm ext} \equiv \bar{j}_{\rm rec,ext}/\bar{j}_{\rm rec,int}$. We note that at $z \gtrsim 3$, when photons that make it into the background are quickly absorbed and, thus, sourcing recombinations, $f_{\rm ext}$ is given by the fraction of ionizing photons that escape galaxies (including ones hosting AGN) times the fraction of these recombinations the survey picks up $f_{\kappa,g}$. We use the quasar emissivity function of (Khaire & Srianand, 2015) and the UV-only star formation rate from Haardt & Madau (2012) to calculate $f_{\rm ext}$, making the assumption that all ionizing photons escape from quasars, and approximately none make it out of galaxies. We find $f_{\rm ext} = [0.06, 0.07, 0.04]$ at $z = [1, 2, 3]$.

Figure 4.3 shows our estimates for the recombination-line flux power spectrum at $z = 1$, $z = 2$, and $z = 3$ for ionizing background fluctuation models with quasar lifetimes of $t_Q = 100$ Myr and $t_Q = \infty$. These estimates are for the intensity mapping mode in which $f_{\kappa,g} = 1$ so that all recombination photons contribute to the survey. This applies, for example, to the intensity mapping surveys of SPHEREx in Hα and HETDEX in Lyα. For these calculations, we use the

---

[6] In detail both coefficients are also multiplied by the fraction of recombinations that cascade through the desired transition, but this overall coefficient cancels out in our calculations (since it is essentially independent of the properties of the absorbing gas).

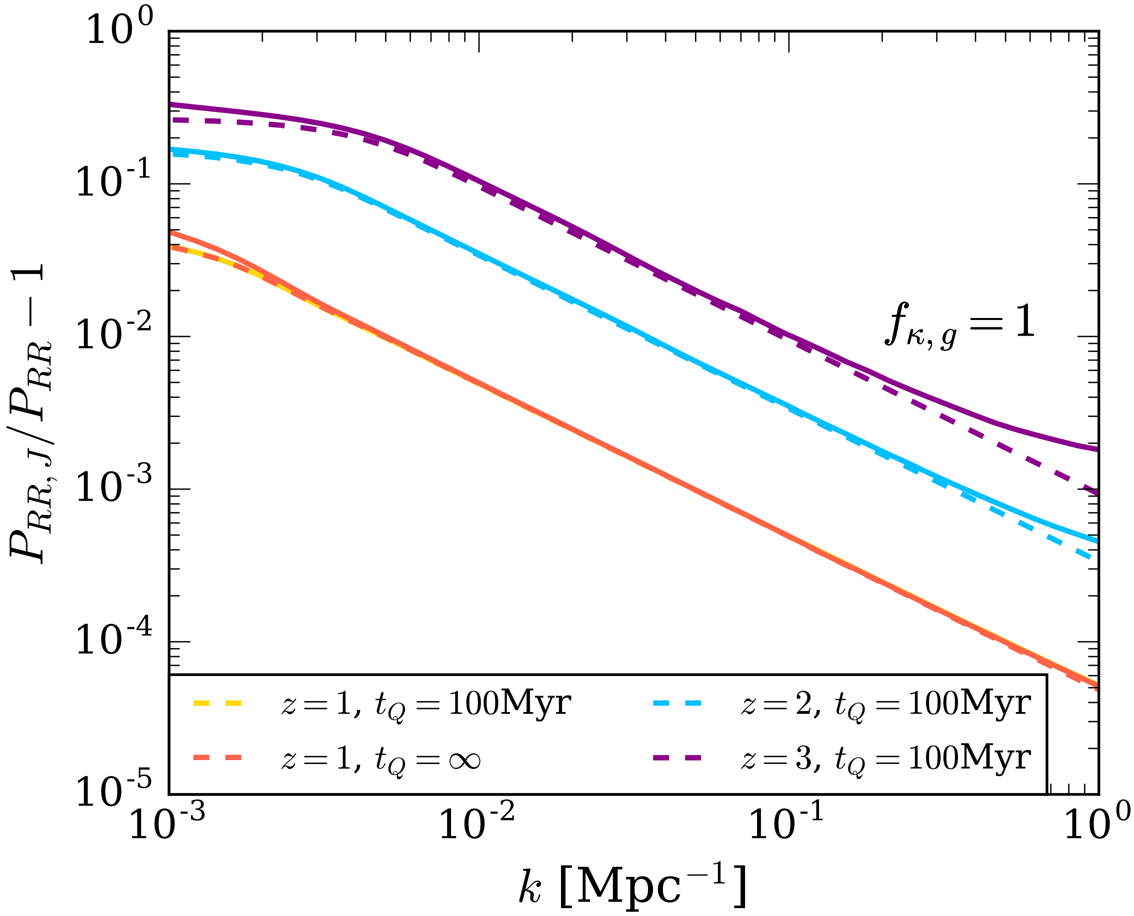

Figure 4.3: Predictions for the impact of ionizing background fluctuations intensity mapping surveys targeting recombination lines (such as H I Lyα and Hα). The solid curves are the total fractional contribution to the angularly-averaged power spectrum from intensity fluctuations, and the dashed is the contribution excluding shot noise. While these estimates are for the intensity mapping mode, the main text considers recombination surveys that selects individual sources (where the effect of backgrounds is smaller).

Lyα intensity bias b_g of $[1.16, 1.19, 1.40]$ for $z = [1, 2, 3]$ as reported in Pullen et al. (2014), and the same bias applies for Hα. We further assume that the sizes of absorbers is not affected by Γ so that $b_\Gamma = 1$, and we use the previously-described calculation that finds $b_J = [0.06, 0.07, 0.04]$ at $z = [1, 2, 3]$. The solid curves are the total contribution to the power spectrum from intensity fluctuations, and the dashed curves show the contribution without shot noise. Note that the intensity bias for recombination radiation is positive, in contrast to our 21cm intensity bias, so the shot noise now has an additive effect. However, the clustered component dominates the power, even somewhat more so than for 21cm surveys because b_J is a bit smaller for recombination surveys. We find that the fractional contribution to the power of intensity fluctuations scales as k^{-1} with normalization ranging from 0.005 to 0.1 at $k = 10^{-2}$Mpc^{-1}.

The fluctuations are smaller for a traditional galaxy survey compared to one in intensity mapping mode, as only a fraction of the recombinations associated with background ionizations occur in the aperture used to measure the light from surveyed galaxies. In this case,

$$f_{\kappa,g} \sim \frac{\sigma_{\rm ins} n_g}{\bar{\kappa}_{{\rm eff},\sigma}}, \tag{4.11}$$

where $\sigma_{\rm ins}$ is the aperture of the instrument and n_g is the number density of surveyed galaxies. For HETDEX, using $\sigma_{\rm ins} = 1.8$ arcsec^2, we find a very small value of $f_{\kappa,g} \sim 1 \times 10^{-4}$ for $z = 2$, $\bar{\lambda}_{\rm MFP} = 240$ pMpc and a Lyα emitter density of $n_g = 9 \times 10^{-5}$ Mpc^{-3}. For the SPHEREx galaxy survey, with $\sigma_{\rm ins} = 38$ arcsec^2, for $z = 1, 2$, $\bar{\lambda}_{\rm MFP} = 650, 240$ pMpc, and $n_g = 1.5 \times 10^{-3}$ Mpc^{-3}, we estimate $f_{\kappa,g} \sim 0.02, 0.03$. Because $f_{\kappa,g}$ is so small, for the galaxy-selecting campaigns of HETDEX and SPHEREx the component of the clustering that traces the background computed in this section will be irrelevant. The imprint from ionizing fluctuations that could be more relevant to these campaigns is discussed in the following section.

4.6 Other galaxy surveys

The ionizing background fluctuations may affect the properties of galaxies in general (and not just their H I fractions and the rate of recombinations, as considered in previous sections). Galaxy properties may be modulated by ultraviolet backgrounds, as the $13.6 - 200$eV background ionizes the gas, affecting the rate at which it can cool, and the ≈ 11eV Lyman-Werner background dissociates molecular hydrogen. The former affect has been observed in cosmological simulations (Efstathiou, 1992; Benson et al., 2002; Hambrick et al., 2009, 2011), though the effect is most significant in $\lesssim 10^{10} M_\odot$ halos. While for the larger galactic halos catalogued in large-scale structure (LSS) surveys the modulating effects from background fluctuations is likely small, a rough estimate for their magnitude is important as we target increasingly subtle cosmological imprints with LSS surveys.

Most properties by which galaxies are selected for LSS surveys are related to the galactic star formation rate or the galactic stellar mass. To estimate the effect of the ionizing background on the star formation rate, we start with the ansatz that the observability of a galaxy is proportional to the cooling time of its halo gas. This ansatz is motivated by the idea that star formation is tied to cooling and condensation in the halo (e.g. Sharma et al., 2012; Voit et al., 2017b; McQuinn & Werk, 2017; Tumlinson et al., 2017). We investigate the cases of galaxies with virial temperatures of 5×10^5, $\sim 10^6$ and 5×10^6K. Such temperatures correspond to $z \sim 0$ halos of approximately $10^{11.5} - 10^{13}$M$_\odot$, which abundance matching techniques find host stellar masses of $\sim 10^{10} - 10^{11}$ M$_\odot$ (Behroozi et al. 2010; Li & White 2009) – typical galaxy masses. To calculate cooling rates, we use that halo-scale gas is likely to have densities near the halo 'virial density' or mean halo gas density ($\bar{\rho}_{\rm halo} = 200\bar{\rho}$). However, this is just a fiducial density. Many of the models that halo gas cooling to star formation find that the density of gas out to the virial radius could be a tenth of the virial density in $T \sim 10^6$K halos (Sharma et al., 2012), although numerical simulations and cirucmgalactic medium observaitons suggest that more gas is around (Fielding et al., 2017; Werk et al., 2014). In addition, the gas that actually cools and condenses, sourcing star formation, might be denser gas that lies closer to galaxies. Thus, we discuss a range of densities centered around the virial density.

We have run a grid of CLOUDY models for virialized halo gas. The cooling rate of gas depends on its temperature T and ionization parameter, U, where $U = \Phi/n_{\rm H}c$. In these estimates, $n_{\rm H}$ is the density of hydrogen nuclei, and Φ is the ionizing photon flux, which is proportional to the photoionization rate, Γ. We use the rates from the Haardt & Madau (2012) model. Because we are concerned with a fractional change in cooling and because metals dominate the cooling rate at these temperatures for both collisionally and photoionized gas, variations in metallicity do not change the results (although we take $Z = 0.3Z_\odot$, consistente with cirucmglalactic medium measurements; Prochaska et al. 2017). For the fiducial ionizing background model, we assume $\Phi = 4.8 \times 10^4$ cm^{-2} s^{-1} at $z = 0.2$ based on Haardt & Madau (2001), and a spectral shape based on Haardt & Madau (2012).

Figure 4.4 shows how the cooling rate changes as a function of ionization parameter based on the CLOUDY-computed rates. The curves represent the specified gas temperatures. The shaded band represents the range of ionization parameters if the halo gas is within a factor of three of the mean halo density, where the mean halo density is roughly defined as $\bar{\rho}_{\rm halo} = 200\bar{\rho}$. This same shaded band applies over all considered redshifts $z = 0.5 - 2$, as the mean halo density changes inversely with photoionization rate at these redshifts such that Φ/n_H is surprisingly flat. The fractional change in the cooling rate of the virial temperature curves in this allowed band range between $\sim 10^{-3}$ and 10^{-1}. (The fractional change is generally small because the ionization state of the gas will be set by collisions and, hence, less shaped by the ionizing background.)

Like the two previous sections, Equation 4.2 describes the power spectrum of galaxies where the crucial piece we aim to calculate is the intensity bias, b_J. Under our assumption that the observability of a galaxy is proportional to the cooling time of its halo gas, then $b_J = d\log\Gamma/d\log U$, the quantity calculated in Figure 4.4. While the exact b_J in this model is dependent on gas temperature and strongly on ionization parameter, let us consider a fiducial model with gas temperature of 10^6 K and an ionization parameter representing gas just around and below the virialized density at $z = 0.5 - 2$, $\log U = -1.3$, such that $b_J = 0.05$. Depending on galaxy properties, b_J could be a factor of several larger or smaller than this value, and our results for the fractional impact on the power spectrum depend linearly on b_J. The clustering bias, b_g is calculated using a Sheth-Tormen halo mass function (Sheth et al., 2001), where b_g is $[1.24, 1.47, 2.12]$ for $z = [0.5, 1.0, 2.0]$ at a virial temperature of 10^6 K corresponding to halo masses of $[1.5 \times 10^{12}, 1.1 \times 10^{12}, 6.2 \times 10^{11}]$ M$_\odot$[7]

---

[7] For 5×10^5 K gas, $b_g = [1.06, 1.23, 1.72]$ at $z = [0.5, 1.0, 2.0]$, corresponding to halo masses of $[5.2 \times 10^{11}, 3.6 \times 10^{11}, 2.1 \times 10^{11}]$ M$_\odot$.

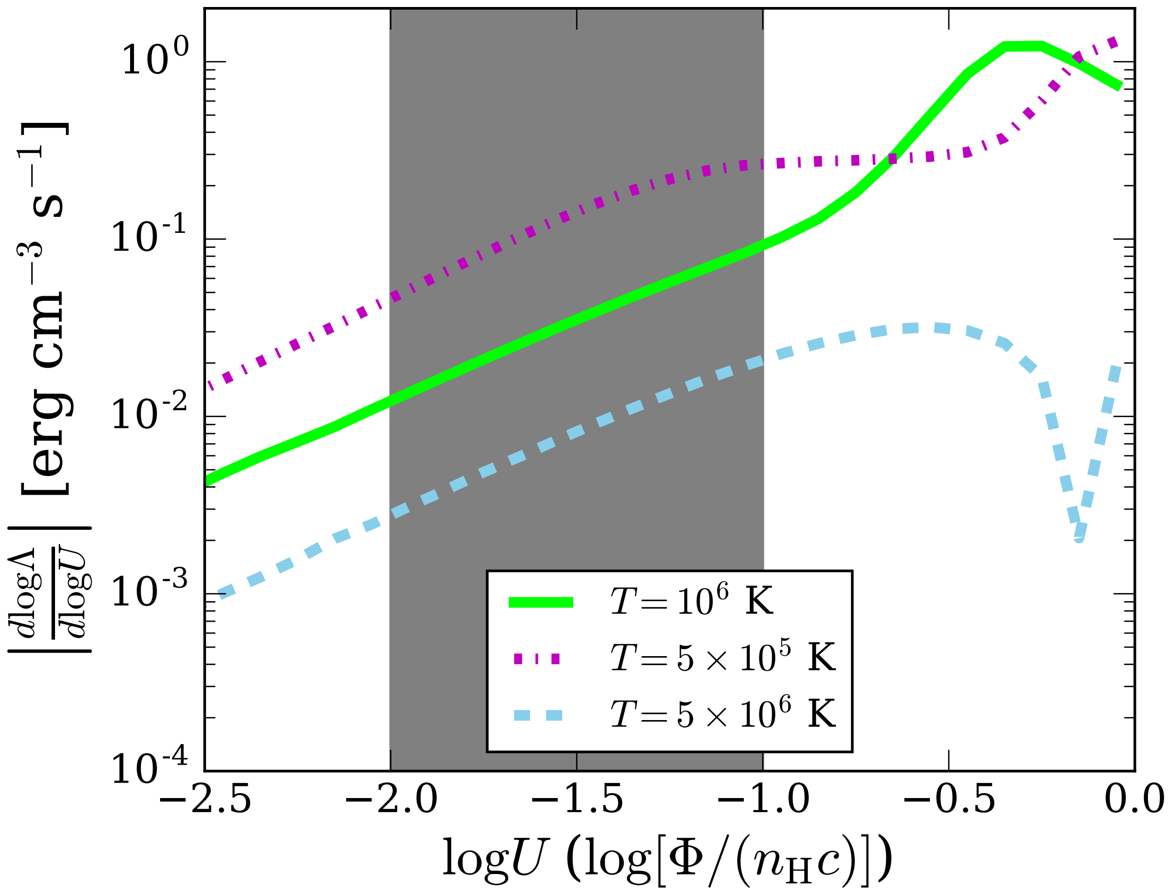

Figure 4.4: The fractional change in the cooling rate with respect to a fractional change in the ionization parameter, which is equal to our intensity bias parameter b_J. The purple, green, and blue curves show this change for gas temperatures of 5×10^5, 10^6 and 5×10^6K, respectively. The grey band brackets the ionization parameters, corresponding to a factor of three less and more than the mean halo gas density of $z = 0.5-2$ halos ($\log U \approx -1.5$ for the mean halo gas density at all of these redshifts).

Figure 4.5 shows the effect of fluctuations on the galaxy flux power spectrum under these choices for b_g and b_J. Because the intensity bias is small, the effect of fluctuations is no more than a couple percent at $k < 10^{-2}$ Mpc^{-1}. However, precision measurements in future surveys (such as searches for primordial non-Gaussianity at the sub-percent level) may still be biased by this small modulation. We estimate the magnitude this contamination could bias cosmology constraints in the following section.

There are a couple caveats with these estimates. First, these estimates are for galaxy selection that is sensitive to star formation rate. If the selection is more sensitive to stellar mass, the background that shapes the cooling is more weighted towards the past, when the fluctuations were larger. Also, in the past, background fluctuations could have a larger effect on cooling because of the lower virial temperatures of the progenitor system. (One could also imagine that if the background were larger in a region, then there would be less cooling at earlier times leading to larger densities and more cooling at later times, altering the response we have estimated.) Second, a galaxy's star formation rate could also be modulated by metagalactic Lyman-Werner ($\sim$ 11eV) backgrounds, which can dissociate molecular hydrogen and hence prevent star formation. The effective mean free path of such backgrounds is smaller than this for ionizing backgrounds ($\sim 0.1H^{-1}$ compared to $\sim H^{-1}$) so that fluctuations in the Lyman-Werner background are larger. However, the Lyman-Werner background inside a molecular cloud is likely to be dominated by galactic star formation (Gnedin, 2010), unlike the background that sets the ionization of the much more extended circumgalactic medium. Thus, the modulation of galactic star formation rates from Lyman-Werner backgrounds is likely to be substantially smaller than from ionizing backgrounds.

4.7 Cosmological parameter biases

Finally, we investigate the robustness of certain cosmological parameter constraints from the galaxy power spectrum with contamination from background fluctuations. We compare the effects of generic models of neutrinos, the spectral index of density fluctuations (n_s), and most notably, primordial non-Gaussianity (f_{NL}) to the impact of fluctuations on the galaxy power spectrum.

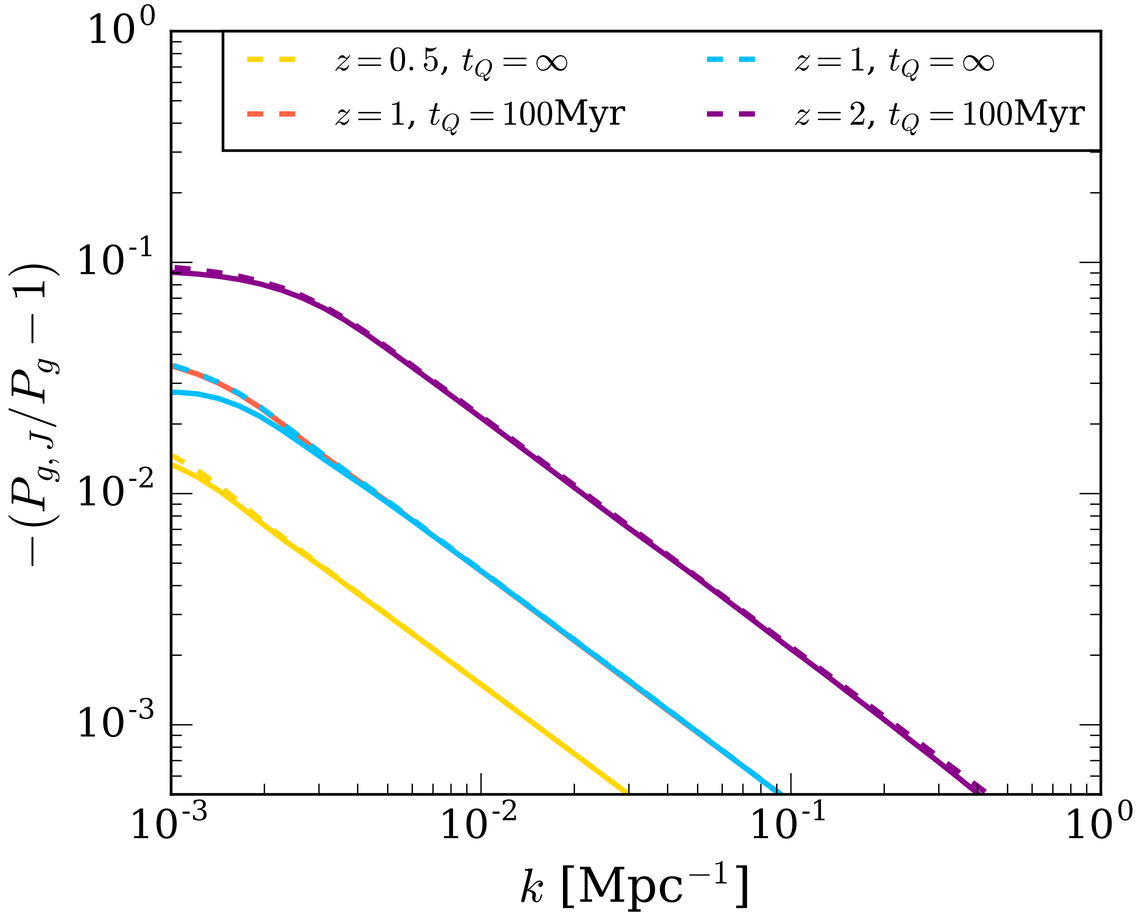

Figure 4.5: Predictions for the fractional change from ionizing background fluctuations on the $z = 0.5$, $z = 1$ and $z = 2$ galaxy power spectrum for $b_J = 0.05$. Unlike in the previous plots, these estimates apply to galaxy surveys of 'typical' galaxies with $T_{\rm vir} \sim 10^6$K and not just to intensity mapping surveys. However, the values are more uncertain as these calculations require assumptions for how galaxy formation is affected by ionizing backgrounds. Our model that connects observability to halo cooling suggests $b_J = [2 \times 10^{-3} - 0.2]$; the amplitude of the fractional change in the power spectrum scales linearly with b_J. The solid curves are the total contribution to the power spectrum from intensity fluctuations, and the dashed is the contribution excluding shot noise.

Because inflation causes quantum fluctuations to expand beyond the horizon scale, the amplitude of curvature fluctuations becomes nearly scale-free. Curvature fluctuations scale to density fluctuations as k^{n_s}, where $n_s = 1$ if completely scale-independent. Because inflation is a finite phase, and the number of e-foldings is finite, n_s must deviate from unity, though CMB measurements indicate that this deviation is small. Currently, Planck provides the tightest bounds of $n_s = 0.9649 \pm 0.0042$ (Planck Collaboration, 2018).

The free-streaming of neutrinos contributes to a damping of perturbation growth. This damping was confirmed when it was determined by neutrino oscillations that neutrinos have a non-zero mass. The total neutrino mass, or sum of all flavors, has been recently constrained by the CMB to be < 0.12 eV (Planck Collaboration, 2018). In this section, we use linear theory predictions of the fractional effect on the total matter power spectrum due to different total neutrino masses from Wagner et al. (2012). We select a model with normal hierarchy and total neutrino mass (a sum over the masses of the flavor eigenstates) of 0.1 eV.

Like n_s, the non-Gaussianity of primordial density perturbations, $f_{\rm NL}$, also reveals the nature inflation. The value of $f_{\rm NL}$, the deviation from linearity, should distinguish between single- and multi-field inflationary models. If primordial non-Gaussianity is detected, the single-field model is ruled out. We model $f_{\rm NL}$ at the critical sensitivity, $f_{\rm NL} \sim 1$, which is established by the non-Gaussianity of second-order perturbations. The scale-dependent correction to the linear density bias is (Matarrese & Verde, 2008; Slosar et al., 2008; Dalal et al., 2008; Desjacques & Seljak, 2010; de Putter & Doré, 2017)

$$b = b_g + 2f_{\rm NL}(b_g - 1)\delta_c \left(\frac{3\Omega_m H_0^2}{2k^2 T(k) D(z)} \right), \tag{4.12}$$

where $\delta_c = 1.686$ and is the threshold density for spherical collapse,[8] H_0 is the Hubble constant, and $D(z)$ is the linear growth function normalized to $(1+z)^{-1}$ when the Universe is matter-dominated.

Figure 4.6 shows the galaxy power spectrum residuals at $z = 1$ of three models of these cosmological effects: neutrinos with a mass of 0.1 eV, $\Delta n_s \pm 0.01$, and $f_{\rm NL} = 1$. We compare these

---

[8] Formally in a matter dominated universe, but still largely holds for ΛCDM to $z = 0$.

residuals with the residuals of the fluctuation models from the previous section, with clustering and shot components and clustering component only. The quasar fluctuations are sourced from our $t_Q = \infty$ model. The shape of the residuals from neutrinos and Δn_s are not degenerate with fluctuations, and thus the effect of fluctuations are easier to disentangle, though would still introduce bias if not modeled. This is not entirely the case for $f_{\rm NL}$, where the change in the shape dependent bias is degenerate with fluctuations.

4.8 Conclusions

Motivated by the principle that the ionizing background is the only non-gravitational astrophysical process that can affect > 1Mpc large-scale structure (LSS) correlations, this paper made estimates for the impact of ultraviolet background fluctuations on various large-scale clustering measurements. In particular, we have focused on efforts that map the diffuse post-reionization 21cm intensity, that select millions of Lyα and Hα emitters, and that survey of the order of Milky Way mass galaxies.

For the diffuse 21cm radiation from all galaxies, a larger ionizing background results in less H I, as the metagalactic background is able to penetrate further into galaxies. While most H I is in damped Lyman-α systems that are self shielded to the ionizing background (and, hence, seemingly well protected from fluctuations), we developed three different estimates that suggest that the response of the H Ibackground is not insignificant, with our two most realistic estimates finding a $0.25\delta\Gamma/\Gamma$ change in the amount of H I, where $\delta\Gamma$ is the infinitesimal change in the background photoionization rate. We further find that this response is relatively constant with redshift.

For surveys whose emission is dominated by recombinations (e.g. Lyα and Hα), a larger ionizing background results in an increase in recombination emission, as the number of recombinations is tied to the number of photoionizations. When intensity mapping so that all such photons are detected, the intensity bias is roughly the ratio of ionizing photons that make it into the background to those that are produced in total. For $z = [1, 3]$, we find a factional response of $[0.06, 0.04] \times \delta\Gamma/\Gamma$, resulting in a fractional change in power of $\sim [0.005, 0.1](k/[10^{-2}\text{pMpc}^{-1}])^{-1}$ at $z = [1, 3]$. How-

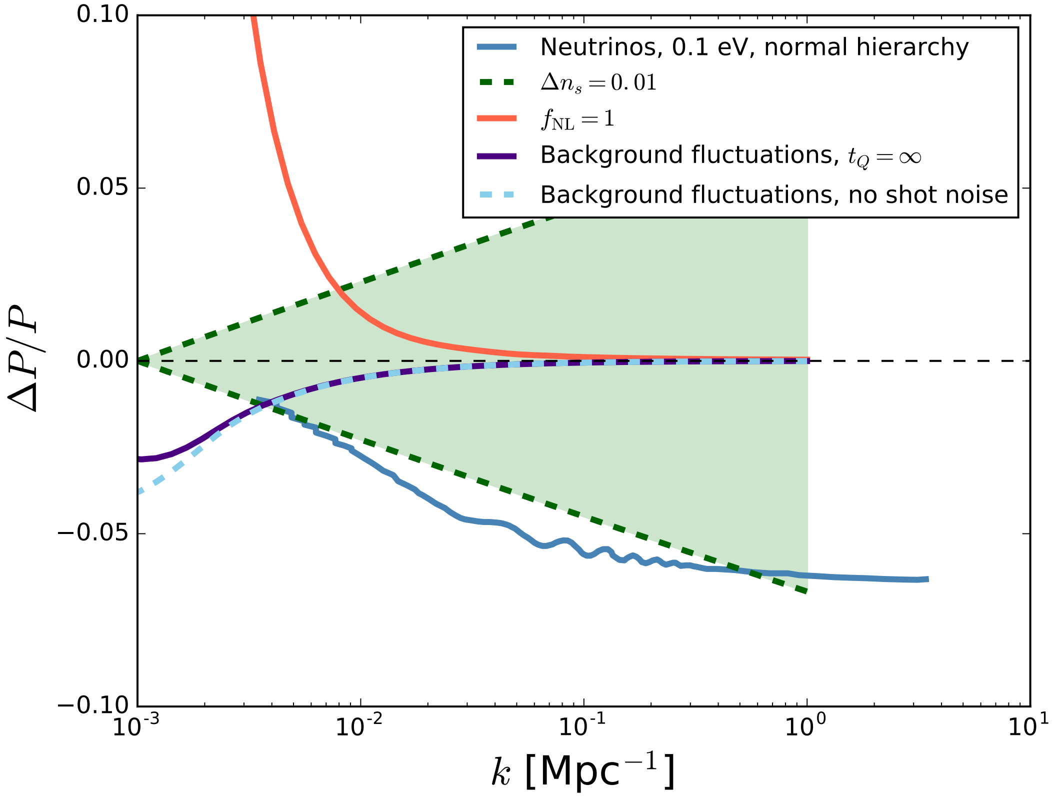

Figure 4.6: Residuals of different cosmological effects on the galaxy power spectrum at $z = 1$. The purple curve shows the residuals of our model from Section 4.6 with background fluctuations sourced by quasars with infinite lifetimes. The light blue dashed curve shows the same model, excluding shot noise. The fractional effect on power from neutrinos with a total mass over all flavor eigenstates of 0.1 eV is shown in darker blue, $\Delta n_s = 0.01$ is shown as the green band, and $f_{\mathrm{NL}} = 1$ is shown in orange.

ever, for the campaigns that correlate individual galaxy positions (rather than intensity mapping the diffuse background), we find that the fraction of fluctuation-tracing recombinations that will occur within the aperture of the instrument will be too small to detect. Our estimates are relevant for HETDEX and SPHEREx, which aim to both pursue traditional galaxy survey as well as intensity mapping surveys.

Finally, we considered how a standard galaxy survey that selects its galaxies based on a property related to their star formation rate (or possible stellar mass) could be modulated by ionizing backgrounds. Following work that connects the cooling rate in galactic halos to the star formation rate, we adopted the ansatz that the star formation rate is proportional to the cooling rate of halo gas. Considering motivated ranges for the density of gas in halos (centered around 200 times the mean density), we found a fractional response in the star formation rate of $\sim 0.01 - 0.1 \delta\Gamma/\Gamma$ for gas at 10^6 K, and a resulting fractional change in the galaxy clustering power spectrum of $\sim [10^{-3}, 10^{-2}](k/[10^{-2}\mathrm{pMpc}^{-1}])^{-1}$. Somewhat smaller virial temperatures result in a larger effect and larger result in a smaller, and the fractional impact increases with redshift owing to the ionizing background fluctuations being larger. Because these calculations relied on the simple ansatz that galaxy observability scales with the cooling of halo gas (whose properties are also uncertain), this estimate is far more uncertain than our estimates for 21cm and recombination radiation surveys.

For typical responses, the modulation from ionizing backgrounds is generally dominated by the cross correlation between the traditional galaxy clustering signal and the density-tracing component of intensity fluctuations, resulting in a contribution that typical scales as k^{-1} on wavenumbers larger than the inverse of the photon mean free path. We also considered the stochastic contribution to intensity fluctuations from the rareness of the sources. We found that the stochastic term can matter if (1) if $b_J \gtrsim 0.1$ resulting in a large coupling to intensity fluctuations and (2) quasars with > 100 Myr lifetimes are the dominant contributor to the ionizing background. Our estimates suggest that the coupling may only be large enough for the stochastic term to matter for 21cm intensity mapping surveys and if quasars dominate the background.

The effect of ionizing backgrounds is the only astrophysical contaminant of cosmological correlations on $\gtrsim 1\mathrm{pMpc}$ scales (as winds from galaxies only travel a limited distance).[9] We compared the size of the predicted effects to benchmark cosmological parameter constraints targeted by forthcoming large-scale structure surveys, finding that neutrino mass and scalar spectral index, n_s, are not degenerate with the effect of fluctuations. Searches for primordial non-Gaussianity from scale-dependent bias in the galaxy power spectrum could be biased by fluctuations in the ionizing background at the level of $\Delta f_{\rm NL} \sim -0.3$.

We would like to thank Anson D'Aloisio for helpful discussions.

4.9 A. Models for the response of H I to a change in the ionizing background

In this appendix, we outline our three methods for computing the response of H I to a change in the ionizing background. These methods are used in § 4.4.

4.9.1 Model based on results of Rahmati et al. (2013)

This method uses the H I column density distribution from cosmological simulations post-processed with ionizing radiative transfer in Rahmati et al. (2013). Because their simulations capture the LSS, detailed properties of halo gas, feedback processes, as well as detailed radiative transfer with complicated geometries, their fitting formulae capture physics that cannot be accounted for in simplified models. Rahmati et al. (2013) calculated how the H I in these simulations attenuates the ionizing background, finding that the photoionization rate as a function of density is given by the fitting formula

$$\frac{\Gamma_{n_{\rm H}}}{\Gamma_{\rm bk}} = 0.98\left[1+\left(\frac{n_{\rm H}}{n_{\rm H,SS}}\right)^{1.64}\right]^{-2.28} + 0.02\left[1+\left(\frac{n_{\rm H}}{n_{\rm H,SS}}\right)\right]^{-0.84}, \tag{4.13}$$

where $\Gamma_{\rm bk}$ is the background photoionization rate incident upon the absorber, $\Gamma_{n_{\rm H}}$ is the photoionization rate which it self shields to, and $n_{\rm H,SS}$ is the density of the IGM that starts to self-shield.

---

[9] Galactic feedback can affect low wavenumbers in the galaxy power spectrum, but this is from the large-scale manifestation of small-scale behavior that is captured by the coefficients in the effective perturbation theory of large-scale structure (Lewandowski et al., 2015).

This density threshold is given by setting $\tau_{\rm HI} = 1$ and using the following relation from Schaye (2001):

$$N_{\rm HI} \sim 2.3 \times 10^{13} {\rm cm}^{-2} \left(\frac{n_{\rm H}}{10^{-5}{\rm cm}^{-3}}\right)^{3/2} \left(\frac{T}{10^4{\rm K}}\right)^{-0.26} \left(\frac{\Gamma}{10^{-12}{\rm s}^{-1}}\right)^{-1} \left(\frac{f_g}{0.16}\right)^{1/2}, \quad (4.14)$$

which is derived by relating the size and density of absorbers by assuming they are the Jeans length. Evaluating for $N_{\rm HI} = 4 \times 10^{17}$, this gives

$$n_{\rm H,SS} = 6.7 \times 10^{-3} \frac{\sigma_{\rm eff}}{2.49 \times 10^{-18}~{\rm cm}^{-2}} T_4^{0.17} \Gamma_{12}^{2/3}~~{\rm cm}^{-3}. \quad (4.15)$$

Thus, given a density for an absorber, one can calculate how the absorber self-shields in response to a given ionizing background.

Finally,Rahmati et al. (2013) presents a distribution of systems in simulations that are optically thin. Conveniently, the column density distribution at these columns does not change substantially with redshift (Prochaska et al., 2010) though simulations suggest a steepening mildly at very high redshifts. Note that self-shielding changes this scaling, but an optically thin simulation shows a similar power-law through all columns. To calculate the self-shielded neutral fraction, $X_{\rm HI,SS}$, we utilize Equation 4.13 to calculate the photoionization rate. Using the ratio of the shelf-shielded to the optically thin neutral fraction, we determine how changes in the background alter the self-shielding threshold and, subsequently, how changes in the photoionization rate affect the neutral fraction. Figure 4.7 shows an optically thin column density distribution function from Rahmati et al. (2013) at $z = 3$ (dotted curve) and our calculation for the self-shielding column density distribution function using the Rahmati et al. (2013) fitting formulae (red curve). The green curve shows how the column density distribution function changes when the global photoionization rate is doubled.

Using the optically thin column density distribution in Rahmati et al. (2013), a gas temperature of 10^4 K, and ionizing background photoionization rate of $\Gamma = 10^{-12}~{\rm s}^{-1}$, we calculate the bias as the change in mean cosmic number density of H I dictated by the magnitude of the ionizing background as a function of the photoionization rate and redshift,

$$b_J = \frac{d}{d\Gamma}\left(\int dN_{\rm HI}^{\rm NSS} f^{\rm NSS}(N_{\rm HI}) N_{\rm HI}(N_{\rm HI}^{\rm NSS}|\Gamma, z)\right) \tag{4.16}$$

where $f^{\rm NSS}$ is the column density distribution with no self-shielding.

4.9.2 Photoionized slab model

Our second method to calculate the H I intensity bias models absorbers as semi-infinite slabs. This method does not incorporate the complex 3D geometry of self-shielding systems that is encoded into the Rahmati et al. (2013) fitting formulae, but is an intuitive and simpler physical model. These slabs are modeled as infinite in extent and their width is set by the Jeans length. We set the density $n_{\rm H}$ as given by Equation 4.14 for a given column and temperature to be $T = 10^4$K. We perform 1D radiative transfer calculations with the incident radiation oriented perpendicular to the slab, with one ray incident from both sides and the two rays summing to a total incident photoionization rate of $\Gamma_{\rm bk}$. The incident background spectrum is modeled as a simple power law of the form $J_\nu \propto (\nu/\nu_0)^{-\alpha}$, where $\alpha = 1$ with a cutoff at 4 Ry, motivated by the shape of ionizing background models above 1 Ry (Haardt & Madau, 2012; Upton Sanderbeck et al., 2016). The radiative transfer divides the slab into cells, attenuating the rays as they traverse cells by their neutral fraction during the previous iteration, casting one ray after the other. In each cell, we assume the gas within the cell is in photoionization equilibrium to calculate the neutral fraction that will be used for subsequent iterations. This calculation is then iterated until the neutral fraction of the slab has converged.

This calculation yields a mapping between our initial "no self-shielding" $N_{\rm HI}^{\rm NSS}$ and $N_{\rm HI}^{\rm SS}$, just as in our calculation based on Rahmati et al. (2013). Again using the optically thin column density distribution of Rahmati et al. (2013) we can then transform to the optically thick using this calculation, and estimate the response of the H I abundance. The final results of this slab model calculation yields approximately a 20% change in the amount of H I when the photoionization rate is increased by a factor of 2.

This model and that in § 4.9.1 assumed the size of the absorber is the Jeans length (Schaye et al., 2000). The Jeans length is only an approximate scale and so, even to the extent this assumption

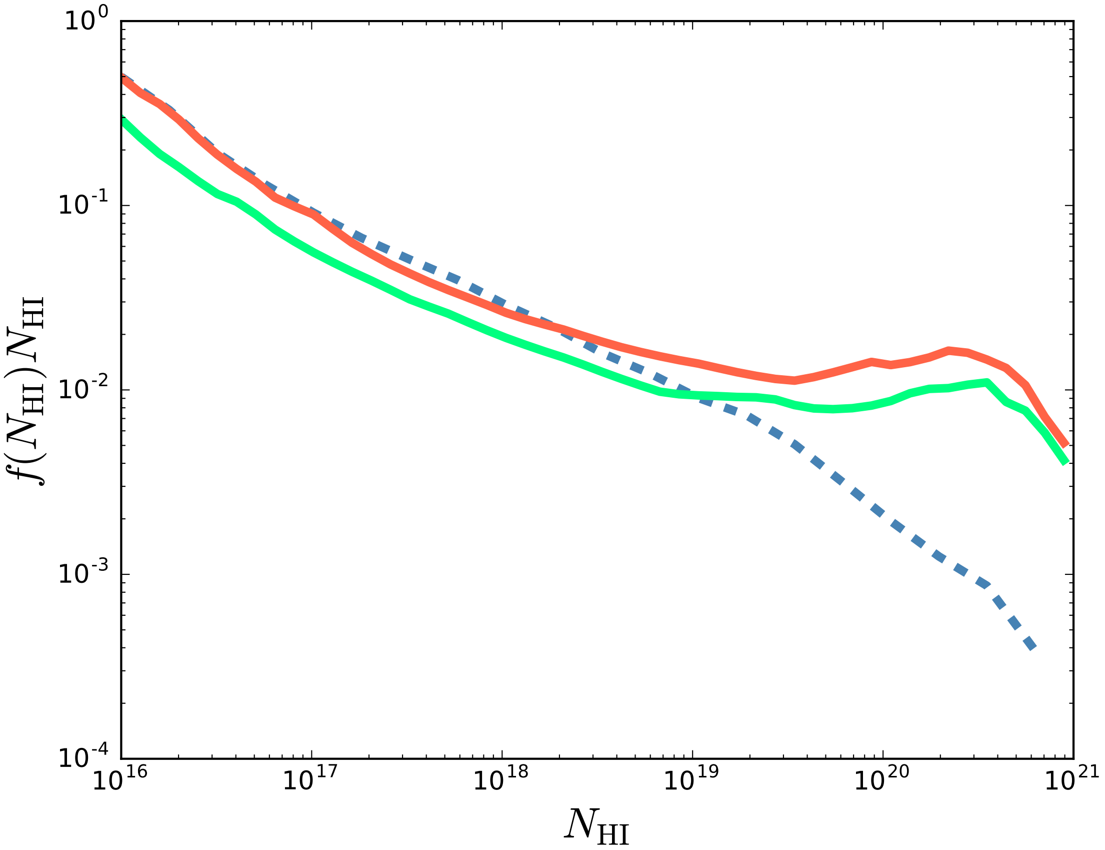

Figure 4.7: Column density distribution functions at $z = 3$ for two cases that with self-shielding (solid curves) and one that is optically thin (dashed). The red curve shows the case where the photoionization rate is doubled from the reference photoionization rate ($\Gamma_{\rm bk} = 1 \times 10^{-12}$ s^{-1}).

holds, it should only hold to an order unity factor. To estimate the sensitivity of our models to this ansatz, we vary the size of absorbers and find that the H I bias changes negligibly ($\sim 1\%$) when varying the sizes of absorbers within a factor of two.

4.9.3 Model based on a critical density for self shielding and power-law profiles

Finally, a rough estimate for the impact of ionizing background fluctuations on the amount of H I can be obtained from modeling the self-shielding absorbers as having a single power-law profile and a specific density $\Delta_{\rm SS}$ above which the gas self shields (Miralda-Escudé et al., 2000; Furlanetto & Oh, 2005; McQuinn et al., 2011b). Unlike the previous two approaches, this method does not rely on numerical simulations or the Schaye et al. (2000) model for the density of absorbers. In addition, the approximation that self-shielding occurs at a critical density reasonably agrees with what is found in simulations (McQuinn et al., 2011b), and this power-law model has some success at reproducing the column density distribution of Lyman-limit systems and DLAs (Zheng & Miralda-Escudé, 2002).

In this model, the photoionization rate sets the value of $\Delta_{\rm SS}$ via the relation $\Gamma \propto \Delta_{\rm SS}^{(7-\gamma)/3}$, where γ is the power-law index of the gas density distribution $P(\Delta)$ at $\Delta \gg 1$, where Δ is in units of the cosmic mean density (see McQuinn et al., 2011b). The mass in HI is proportional to $\int_{\Delta_{\rm SS}}^{\infty} d\Delta P(\Delta) \sim \Delta_{\rm SS}^{1-\gamma} \sim \Gamma^{\frac{3(1-\gamma)}{7-\gamma}} \sim \Gamma^{-3/2(1-\beta)}$, where β is the spectral index of the column density distribution at optically thin columns (γ and β are easily related in this model). Thus, the overdensity in H I is related to the overdensity in Γ via $\delta_{\rm HI} = -3/2(1-\beta)\delta_\Gamma$ meaning that $b_J = 3/2(1-\beta)$ in equation (4.2). For $\beta = \{1.3, 1.5, 1.7\}$, the range consistent with observations at $N_{\rm HI} \sim 10^{17}{\rm cm}^{-2}$, we find $\{-0.45, -0.75, -1.05\}$. This response is qualitative agreement with the $-[0.2 - 0.3]$ yielded by our other methods, again suggesting the response is large. The response is likely somewhat weaker than this model predicts because this model does not capture the self-shielding transition well, showing a more abrupt break in the column density distribution (Zheng & Miralda-Escudé, 2002).

Chapter 5

CONCLUSIONS

5.1 Summary

While at first glance, the three previous chapters have three seemingly independent stories, they are enfolded in the same collection of questions pertaining to the evolution of matter in the Universe. How and when was the ionizing background born? How did it affect the evolution of the IGM, galaxies, and AGN? What is the nature of these sources of ionizing photons?

In Chapter 2, we modeled the temperature of the intergalactic medium after reionization. We presented a semi-analytical model with a multi-zone approach that more accurately captures the inhomogeneous thermal processes of the IGM during patchy reionization than previous models. We found that recent temperature measurements over $z = 1.6 - 4.8$ are consistent with our models where He II reionization occured at $z = 3 - 4$ and was sourced by quasars. We found He II reionization scenarios with a significantly more extended duration are inconsistent with the measurements. We found that the models of hydrogen reionization that were ruled out by the measurements were low redshift and high temperature scenarios. For instance, we found that models in which the IGM was heated to $30,000$ K with hydrogen reionization occurring over $6 < z < 9$, were inconsistent with the temperature measurements. We also constrained the extent to which alternative (non-photoheating) heating could affect the thermal state, such as heating from TeV blazars, cosmic rays, and other nonstandard mechanisms. We found a maximum of 1 eV of additional heat could be injected per baryon by $z = 2$, and $\lesssim 0.5$ eV at $z > 3$ above standard models with photoheating.

In Chapter 3, we modeled the extreme ultraviolet and soft X-ray background. The EUV and soft X-ray slice of the electromagnetic spectrum sets the ionization state of most metals in the intergalactic and circumgalactic media, and thus shapes the cooling rate of cosmic gas. Despite their astrophysical importance, the extreme UV and soft X-ray are problematic to observe, especially from extragalactic sources, because of Galactic absorption. We modeled the contribution and uncertainties from quasars, X-ray binaries, interstellar gas, circumgalactic gas, virialized gas, and super soft X-ray sources, using empirical inputs and theoretical estimates. Previous models assume quasars are the dominate source to the extreme UV and soft X-ray background, but we argue that there is up to an oder-of-magnitude uncertainty in their contribution at certain energies. We found that hot intrahalo gas, a previously neglected source in ionizing background models, likely emits a notable fraction of this radiation at low redshifts. We also found that emission from the interstellar and circumgalactic media may contribute at the tens-of-percent level at all redshifts we consider. We found that corrections for many circumgalactic and intergalactic metal absorption lines that fall within the extreme UV and soft X-ray are on the order of $\sim 0.3 - 1$ dex due to our estimated uncertainties in the angular-averaged background intensity. Finally, we estimated that in this band, local galactic emissions roughly equate the cosmic background radiation at $r_{\rm prox} = 10 - 100$ kpc from star-forming galaxies.

In Chapter 4, we investigated the effect of ionizing background fluctuations on galaxy clustering. We estimated that background fluctuations have a fractional effect of $\sim 0.01 - 0.1(k/[10^{-2}{\rm Mpc}^{-1}])^{-1}$ on the power spectrum of 21cm intensity mapping at $z \sim 1 - 2$. We found that for Hα and Lyα intensity mapping surveys this effect is $\sim [0.005 - 0.1](k/[10^{-2}{\rm Mpc}^{-1}])^{-1}$ at $z \sim 1 - 3$, though this effect is much smaller for Hα or Lyα emitter surveys that target sources. We made an estimate how on fluctuations in ionizing background alter the cooling rate of halo gas, and thus affect galaxy observability, and found a maximum fractional effect of $\sim 0.03(k/[10^{-2}{\rm Mpc}^{-1}])^{-1}$ at $z = 1$ for low-redshift galaxy surveys in general. We determined that the effect of ionizing background fluctuations are likely smaller than the threshold to meaningfully detect cosmological parameter effects. We focused specifically on primordial non-Gaussianity, finding that ionizing backgrounds could result in a bias of $\Delta f_{\rm NL} \sim 0.3$ for power spectrum measurements.

5.2 Future Work

A large part of the goal of my thesis work has been to improve our understanding of the ionizing background and its uncertainties. Unfortunately, the tools available to the field to produce ionizing background models presently do not yet reflect these advances. Currently, there is no flexible, public tool to model the ionizing background or its uncertainties. In the near future, I plan to construct a code that will model the ionizing background after reionization. Importantly, this code will quantify uncertainties in the ionizing background, filling a void in the ionizing background literature. Ultimately, this code will be made open-source and posted on an online repository, such as *GitHub*, so that it will be accessible to the field. Much of the groundwork for this software has already been constructed in bits and pieces for the work presented in this thesis.

One such way to improve on previous models is to be able to customize the free parameters of the ionizing background. Ideally, the model inputs will be the spectrum of the sources, the HI column density distribution, and the emissivity history of quasars, galaxies, and other sources. The output of the code will be a set of background models plotted against observational constraints. These constraints will be observational estimates of HI and HeII photoionization rates; metal line measurements on the hardness of the background; and low-redshift X-ray background measurements. Our future code will allow the user to vary the inputs within the bounds of uncertainty to quantify the sources of uncertainty.

This code will add new elements to our background calculation that have not been considered in prior calculations. Some possible improvements include

Better models for quasar spectra and galaxy spectra: In previous models, quasar spectra are modeled with a power-law, but this ignores the multitude of lines in the UV regime of these spectra. Previous models also ignore the effect of the frequency-dependent escape fraction of ionizing photons ($f_{\rm esc}(\nu)$) on the emerging spectrum of galaxies. Also, the ionizing spectrum of a stellar population is sensitive to parameters such as the stellar IMF as well as the binary fraction (Stanway et al., 2016), and these dependencies have not been investigated.

Absorption from metals and dust: These have been ignored in previous studies as only hydrogen and helium absorption has been included. While we suspect this is likely a good approximation, we would like to investigate it in more detail.

Contributions of more unconventional sources such as small AGN and hot halo gas: It is still of significant debate what dominates the ionizing background across cosmic time. It is believed that quasars supply the majority of ionizing photons at $z < 3$ and galaxies at $z > 3$, though certain models have called this into question (Madau & Haardt, 2015). Other sources of ionizing photons, such as the ISM, CGM, and hot virialized gas, have also been historically neglected in ionizing background models (though see Chapter 3) and may have significant effects on the photoionization state of local gas.

5.3 Closing Remarks

Our cosmic history is interwoven into the physics of the ionizing background and the matter between galaxies. From the light of the first stars and galaxies, to the formation of our own planet, the photons and matter that fill the sea of space only punctuated by islands of light have guided the evolution of our cosmic habitat. With the exciting new generation of upcoming telescopes and the steady improvement of numerical capabilities, it has been a wonderful time to witness and be a part of the growth of this field.

BIBLIOGRAPHY

Abel, T., & Haehnelt, M. G. 1999, ApJL, 520, L13

Ackermann, M., Ajello, M., Albert, A., et al. 2012, PRD, 85, 083007

Allen, M. G., Groves, B. A., Dopita, M. A., Sutherland, R. S., & Kewley, L. J. 2008, ApJS, 178, 20

Altay, G., Theuns, T., Schaye, J., Crighton, N. H. M., & Dalla Vecchia, C. 2011, ApJL, 737, L37

Arnaud, M., & Evrard, A. E. 1999, MNRAS, 305, 631

Bandura, K., Addison, G. E., Amiri, M., et al. 2014, in , Vol. 9145, Ground-based and Airborne Telescopes V, 914522

Barkana, R., & Loeb, A. 2001, physrep, 349, 125

Baskin, A., Laor, A., & Stern, J. 2014, MNRAS, 438, 604

Battye, R. A., Brown, M. L., Browne, I. W. A., et al. 2012, ArXiv e-prints, arXiv:1209.1041

Bechtold, J., Czerny, B., Elvis, M., Fabbiano, G., & Green, R. F. 1987, ApJ, 314, 699

Becker, G. D., Bolton, J. S., Haehnelt, M. G., & Sargent, W. L. W. 2011, MNRAS, 410, 1096

Becker, G. D., Bolton, J. S., Madau, P., et al. 2015, MNRAS, 447, 3402

Behroozi, P. S., Conroy, C., & Wechsler, R. H. 2010, ApJ, 717, 379

Belczynski, K., Kalogera, V., Rasio, F. A., et al. 2008, ApJS, 174, 223

Benson, A. J., Lacey, C. G., Baugh, C. M., Cole, S., & Frenk, C. S. 2002, MNRAS, 333, 156

Bigot-Sazy, M.-A., Ma, Y.-Z., Battye, R. A., et al. 2016, in Astronomical Society of the Pacific Conference Series, Vol. 502, Frontiers in Radio Astronomy and FAST Early Sciences Symposium 2015, ed. L. Qain & D. Li, 41

Boera, E., Murphy, M. T., Becker, G. D., & Bolton, J. S. 2014, MNRAS, 441, 1916

Bolton, J. S., Becker, G. D., Haehnelt, M. G., & Viel, M. 2014, MNRAS, arXiv:1308.4411

Bolton, J. S., Becker, G. D., Raskutti, S., et al. 2012, MNRAS, 419, 2880

Borgani, S., Rosati, P., Tozzi, P., et al. 2001, ApJ, 561, 13

Boroson, B., Kim, D.-W., & Fabbiano, G. 2011, ApJ, 729, 12

Boyle, B. J., Shanks, T., Croom, S. M., et al. 2000, MNRAS, 317, 1014

Broderick, A. E., Chang, P., & Pfrommer, C. 2012, ApJ, 752, 22

Brorby, M., Kaaret, P., Prestwich, A., & Mirabel, I. F. 2016, MNRAS, 457, 4081

Bruzual, G., & Charlot, S. 2003, MNRAS, 344, 1000

Cantalupo, S. 2010, MNRAS, 403, L16

Carilli, C. L., & Rawlings, S. 2004, , 48, 979

Cassisi, S., Iben, Jr., I., & Tornambè, A. 1998, ApJ, 496, 376

Cen, R., & Ostriker, J. P. 1999, ApJ, 514, 1

Chang, P., Broderick, A. E., & Pfrommer, C. 2012, ApJ, 752, 23

Chen, H.-L., Woods, T. E., Yungelson, L. R., Gilfanov, M., & Han, Z. 2014, MNRAS, 445, 1912

—. 2015, MNRAS, 453, 3024

Chen, H.-W., Lanzetta, K. M., Webb, J. K., & Barcons, X. 1998, ApJ, 498, 77

Chevalier, R. A., & Clegg, A. W. 1985, Nature, 317, 44

Cirelli, M., Iocco, F., & Panci, P. 2009, JCAP, 10, 9

Compostella, M., Cantalupo, S., & Porciani, C. 2013, MNRAS, 435, 3169

Conroy, C., & Gunn, J. E. 2010, ApJ, 712, 833

Croft, R. A. C. 2004, ApJ, 610, 642

Croft, R. A. C., Di Matteo, T., Davé, R., et al. 2001, ApJ, 557, 67

Croom, S. M., Smith, R. J., Boyle, B. J., et al. 2004, MNRAS, 349, 1397

Czerny, B., & Elvis, M. 1987, ApJ, 321, 305

Dalal, N., Doré, O., Huterer, D., & Shirokov, A. 2008, PRD, 77, 123514

D'Aloisio, A., McQuinn, M., & Trac, H. 2015, ApJL, 813, L38

D'Aloisio, A., Upton Sanderbeck, P. R., McQuinn, M., Trac, H., & Shapiro, P. R. 2017, MNRAS, 468, 4691

Davé, R., Cen, R., Ostriker, J. P., et al. 2001, ApJ, 552, 473

Davis, S. W., Woo, J.-H., & Blaes, O. M. 2007, ApJ, 668, 682

de Putter, R., & Doré, O. 2017, PRD, 95, 123513

Della Ceca, R., Scaramella, R., Gioia, I. M., et al. 2000, A&A, 353, 498

Desjacques, V., & Seljak, U. 2010, Classical and Quantum Gravity, 27, 124011

Dexter, J., & Agol, E. 2011, ApJL, 727, L24

Dijkstra, M., Gilfanov, M., Loeb, A., & Sunyaev, R. 2012, MNRAS, 421, 213

Done, C., Davis, S. W., Jin, C., Blaes, O., & Ward, M. 2012, MNRAS, 420, 1848

Doré, O., Werner, M. W., Ashby, M., et al. 2016, ArXiv e-prints, arXiv:1606.07039

Efstathiou, G. 1992, MNRAS, 256, 43P

Fan, X., et al. 2006, AJ, 132, 117

Fardal, M. A., Giroux, M. L., & Shull, J. M. 1998, AJ, 115, 2206

Faucher-Giguère, C.-A., Lidz, A., Zaldarriaga, M., & Hernquist, L. 2009, ApJ, 703, 1416

Faucher-Giguère, C.-A., Prochaska, J. X., Lidz, A., Hernquist, L., & Zaldarriaga, M. 2008, ApJ, 681, 831

Ferland, G. J., Porter, R. L., van Hoof, P. A. M., et al. 2013, RMXAA, 49, 137

Fielding, D., Quataert, E., McCourt, M., & Thompson, T. A. 2017, MNRAS, 466, 3810

Fiore, F., Puccetti, S., Grazian, A., et al. 2012, A&A, 537, A16

Font-Ribera, A., Miralda-Escudé, J., Arnau, E., et al. 2012, JCAP, 11, 059

Fragos, T., Lehmer, B. D., Naoz, S., Zezas, A., & Basu-Zych, A. 2013, ApJL, 776, L31

Fumagalli, M., Haardt, F., Theuns, T., et al. 2017, MNRAS, 467, 4802

Furlanetto, S. R. 2009, ApJ, 700, 1666

Furlanetto, S. R., & Oh, S. P. 2005, MNRAS, 363, 1031

—. 2008, ApJ, 681, 1

—. 2009, ApJ, 701, 94

Furlanetto, S. R., Zaldarriaga, M., & Hernquist, L. 2004, ApJ, 613, 16

Garzilli, A., Bolton, J. S., Kim, T.-S., Leach, S., & Viel, M. 2012, MNRAS, 424, 1723

Gaspari, M., Ruszkowski, M., & Oh, S. P. 2013, MNRAS, 432, 3401

Georgantopoulos, I., Stewart, G. C., Shanks, T., Boyle, B. J., & Griffiths, R. E. 1996, MNRAS, 280, 276

Giallongo, E., et al. 2015, A&A, 578, A83

Gilfanov, M., Grimm, H.-J., & Sunyaev, R. 2004, MNRAS, 347, L57

Gnedin, N. Y. 2010, ApJL, 721, L79

Gnedin, N. Y., & Hollon, N. 2012, ApJS, 202, 13

Gontcho, S. G. A., Miralda-Escudé, J., & Busca, N. G. 2014, ArXiv:1404.7425, arXiv:1404.7425

Greiner, J. 2000, New Astronomy, 5, 137

Grevesse, N., Asplund, M., Sauval, A. J., & Scott, P. 2010, , 328, 179

Grimes, J. P., Heckman, T., Strickland, D., & Ptak, A. 2005, ApJ, 628, 187

Grimm, H.-J., Gilfanov, M., & Sunyaev, R. 2003, MNRAS, 339, 793

Gunn, J. E., & Peterson, B. A. 1965, ApJ, 142, 1633

Guo, Q., White, S., Boylan-Kolchin, M., et al. 2011, MNRAS, 413, 101

Haardt, F., & Madau, P. 1996, ApJ, 461, 20

Haardt, F., & Madau, P. 2001, in Clusters of Galaxies and the High Redshift Universe Observed in X-rays, ed. D. M. Neumann & J. T. V. Tran, 64

—. 2012, ApJ, 746, 125

Haehnelt, M. G., & Steinmetz, M. 1998, MNRAS, 298, L21

Hambrick, D. C., Ostriker, J. P., Johansson, P. H., & Naab, T. 2011, MNRAS, 413, 2421

Hambrick, D. C., Ostriker, J. P., Naab, T., & Johansson, P. H. 2009, ApJ, 705, 1566

Helsdon, S. F., & Ponman, T. J. 2000, MNRAS, 315, 356

Hickox, R. C., & Markevitch, M. 2006, ApJ, 645, 95

Hill, G. J., Gebhardt, K., Komatsu, E., et al. 2008, in Astronomical Society of the Pacific Conference Series, Vol. 399, Panoramic Views of Galaxy Formation and Evolution, ed. T. Kodama, T. Yamada, & K. Aoki, 115

Hiss, H., Walther, M., Hennawi, J. F., et al. 2017, ArXiv e-prints, arXiv:1710.00700

Holden, B. P., Stanford, S. A., Squires, G. K., et al. 2002, AJ, 124, 33

Hopkins, P. F., Richards, G. T., & Hernquist, L. 2007, ApJ, 654, 731

Hornschemeier, A. E., Heckman, T. M., Ptak, A. F., Tremonti, C. A., & Colbert, E. J. M. 2005, AJ, 129, 86

Hui, L., & Gnedin, N. Y. 1997, MNRAS, 292, 27

Hui, L., & Haiman, Z. 2003, ApJ, 596, 9

Inoue, A. K., & Kamaya, H. 2008, ArXiv e-prints, arXiv:0810.5614

Jeltema, T. E., Binder, B., & Mulchaey, J. S. 2008, ApJ, 679, 1162

Johnson, S. D., Chen, H.-W., & Mulchaey, J. S. 2015, MNRAS, 449, 3263

Kahabka, P., & van den Heuvel, E. P. J. 1997, Ann. Rev. Astron.& Astrophys. , 35, 69

Kaiser, N. 1987, MNRAS, 227, 1

Khaire, V., & Srianand, R. 2015, MNRAS, 451, L30

Kollmeier, J. A., Weinberg, D. H., Oppenheimer, B. D., et al. 2014, ApJL, 789, L32

Komatsu, E., et al. 2011, ApJS, 192, 18

Kovetz, E. D., Viero, M. P., Lidz, A., et al. 2017, ArXiv e-prints, arXiv:1709.09066

Kulkarni, S., Sahu, D. K., Chaware, L., Chakradhari, N. K., & Pandey, S. K. 2014, New Astronomy, 30, 51

Kundu, A., Maccarone, T. J., & Zepf, S. E. 2007, ApJ, 662, 525

Lacki, B. C. 2013, ArXiv e-prints, arXiv:1304.6142

Lamberts, A., Chang, P., Pfrommer, C., et al. 2015, ArXix:1502.07980, arXiv:1502.07980

Lanzetta, K. M., Bowen, D. V., Tytler, D., & Webb, J. K. 1995, ApJ, 442, 538

Laor, A., Fiore, F., Elvis, M., Wilkes, B. J., & McDowell, J. C. 1997, ApJ, 477, 93

Laurent, P., Eftekharzadeh, S., Le Goff, J.-M., et al. 2017, JCAP, 7, 017

Lehmer, B. D., Alexander, D. M., Bauer, F. E., et al. 2010, ApJ, 724, 559

Lehmer, B. D., Tyler, J. B., Hornschemeier, A. E., et al. 2015, ApJ, 806, 126

Leitherer, C., Schaerer, D., Goldader, J. D., et al. 1999, ApJS, 123, 3

Lewandowski, M., Perko, A., & Senatore, L. 2015, JCAP, 5, 019

Li, C., & White, S. D. M. 2009, MNRAS, 398, 2177

Lidz, A., Faucher-Giguère, C.-A., Dall'Aglio, A., et al. 2010, ApJ, 718, 199

Lidz, A., Hopkins, P. F., Cox, T. J., Hernquist, L., & Robertson, B. 2006, ApJ, 641, 41

Lidz, A., & Malloy, M. 2014, ApJ, 788, 175

Lidz, A., McQuinn, M., Zaldarriaga, M., Hernquist, L., & Dutta, S. 2007, ApJ, 670, 39

Linden, T., Kalogera, V., Sepinsky, J. F., et al. 2010, ApJ, 725, 1984

Lusso, E., Worseck, G., Hennawi, J. F., et al. 2015, MNRAS, 449, 4204

Madau, P., & Fragos, T. 2017, ApJ, 840, 39

Madau, P., & Haardt, F. 2015, ApJL, 813, L8

Madau, P., Haardt, F., & Rees, M. J. 1999, ApJ, 514, 648

Mantz, A. B., Allen, S. W., Morris, R. G., et al. 2017, MNRAS, 472, 2877

Markevitch, M. 1998, ApJ, 504, 27

Martini, P., & Weinberg, D. H. 2001, ApJ, 547, 12

Matarrese, S., & Verde, L. 2008, ApJL, 677, L77

McCourt, M., Sharma, P., Quataert, E., & Parrish, I. J. 2012, MNRAS, 419, 3319

McDonald, P., Miralda-Escudé, J., Rauch, M., et al. 2001, ApJ, 562, 52

McDonald, P., Seljak, U., Cen, R., Bode, P., & Ostriker, J. P. 2005, MNRAS, 360, 1471

McGreer, I. D., Mesinger, A., & D'Odorico, V. 2015, MNRAS, 447, 499

McGreer, I. D., Jiang, L., Fan, X., et al. 2013, ApJ, 768, 105

McKee, C. F., & Ostriker, J. P. 1977, ApJ, 218, 148

McQuinn, M. 2009, ApJL, 704, L89

—. 2012, MNRAS, 426, 1349

—. 2014, ApJL, 780, L33

—. 2016, Ann. Rev. Astron.& Astrophys. , 54, 313

McQuinn, M., Hernquist, L., Lidz, A., & Zaldarriaga, M. 2011a, MNRAS, 415, 977

McQuinn, M., Lidz, A., Zaldarriaga, M., et al. 2009, ApJ, 694, 842

McQuinn, M., Oh, S. P., & Faucher-Giguère, C.-A. 2011b, ApJ, 743, 82

McQuinn, M., & Upton Sanderbeck, P. 2015, ArXiv e-prints, arXiv:1505.07875

McQuinn, M., & Werk, J. K. 2017, ArXiv e-prints, arXiv:1703.03422

McQuinn, M., & Worseck, G. 2014, MNRAS, 440, 2406

Meiksin, A., & Madau, P. 1993, ApJ, 412, 34

Meiksin, A., & White, M. 2004, MNRAS, 350, 1107

Meiksin, A. A., & McQuinn, M. 2018, in prep.

Mineo, S., Gilfanov, M., & Sunyaev, R. 2012a, MNRAS, 419, 2095

—. 2012b, MNRAS, 426, 1870

Miniati, F., & Elyiv, A. 2013, ApJ, 770, 54

Miniati, F., Ferrara, A., White, S. D. M., & Bianchi, S. 2004, MNRAS, 348, 964

Mirabel, I. F., Dijkstra, M., Laurent, P., Loeb, A., & Pritchard, J. R. 2011, A&A, 528, A149

Miralda-Escudé, J., Haehnelt, M., & Rees, M. J. 2000, ApJ, 530, 1

Miralda-Escudé, J., & Rees, M. J. 1994, MNRAS, 266, 343

Morales, M. F., & Wyithe, J. S. B. 2010, Ann. Rev. Astron.& Astrophys. , 48, 127

Mulchaey, J. S., Davis, D. S., Mushotzky, R. F., & Burstein, D. 2003, ApJS, 145, 39

Münch, G., & Zirin, H. 1961, ApJ, 133, 11

Naoz, S., Noter, S., & Barkana, R. 2006, MNRAS, 373, L98

Newburgh, L. B., Bandura, K., Bucher, M. A., et al. 2016a, in , Vol. 9906, Ground-based and Airborne Telescopes VI, 99065X

Newburgh, L. B., Bandura, K., Bucher, M. A., et al. 2016b, in , Vol. 9906, Ground-based and Airborne Telescopes VI, 99065X

Nielsen, M. T. B., & Gilfanov, M. 2015, MNRAS, 453, 2927

Nomoto, K., Saio, H., Kato, M., & Hachisu, I. 2007, ApJ, 663, 1269

Osterbrock, D. E., & Ferland, G. J. 2006, Astrophysics of gaseous nebulae and active galactic nuclei

Owen, R. A., & Warwick, R. S. 2009, MNRAS, 394, 1741

Pacucci, F., Mesinger, A., Mineo, S., & Ferrara, A. 2014, MNRAS, 443, 678

Patil, M. K., Pandey, S. K., Sahu, D. K., & Kembhavi, A. 2007, A&A, 461, 103

Pen, U.-L. 1999, ApJL, 510, L1

Pérez-Ràfols, I., Font-Ribera, A., Miralda-Escudé, J., et al. 2018, MNRAS, 473, 3019

Planck Collaboration. 2018, ArXiv e-prints, arXiv:1807.06209

Planck Collaboration, Ade, P. A. R., Aghanim, N., et al. 2015, ArXiv e-prints, arXiv:1502.01589

Pontzen, A. 2014, PRD, 89, 083010

Pontzen, A., Bird, S., Peiris, H., & Verde, L. 2014, ApJL, 792, L34

Pratt, G. W., Croston, J. H., Arnaud, M., & Böhringer, H. 2009, A&A, 498, 361

Prochaska, J. X., Madau, P., O'Meara, J. M., & Fumagalli, M. 2014, MNRAS, 438, 476

Prochaska, J. X., O'Meara, J. M., & Worseck, G. 2010, ApJ, 718, 392

Prochaska, J. X., Weiner, B., Chen, H.-W., Mulchaey, J., & Cooksey, K. 2011, ApJ, 740, 91

Prochaska, J. X., Werk, J. K., Worseck, G., et al. 2017, ApJ, 837, 169

Puchwein, E., Bolton, J. S., Haehnelt, M. G., et al. 2015, MNRAS, 450, 4081

Puchwein, E., Pfrommer, C., Springel, V., Broderick, A. E., & Chang, P. 2012, MNRAS, 423, 149

Pullen, A. R., Doré, O., & Bock, J. 2014, ApJ, 786, 111

Rahmati, A., Schaye, J., Pawlik, A. H., & Raičevic, M. 2013, MNRAS, 431, 2261

Ranalli, P., Comastri, A., & Setti, G. 2003, A&A, 399, 39

Raskutti, S., Bolton, J. S., Wyithe, J. S. B., & Becker, G. D. 2012, MNRAS, 421, 1969

Reimers, D., Kohler, S., Wisotzki, L., et al. 1997, A&A, 327, 890

Rephaeli, Y., Gruber, D., & Persic, M. 1995, A&A, 300, 91

Ricotti, M., Gnedin, N. Y., & Shull, J. M. 2000, ApJ, 534, 41

Robertson, B. E., Ellis, R. S., Dunlop, J. S., McLure, R. J., & Stark, D. P. 2010, Nature, 468, 49

Robertson, B. E., Ellis, R. S., Furlanetto, S. R., & Dunlop, J. S. 2015, ApJL, 802, L19

Rorai, A., Hennawi, J. F., & White, M. 2013, ApJ, 775, 81

Ross, N. P., Shen, Y., Strauss, M. A., et al. 2009, ApJ, 697, 1634

Rudie, G. C., Steidel, C. C., & Pettini, M. 2012, ApJL, 757, L30

Rybicki, G. B., & Lightman, A. P. 1979, Radiative processes in astrophysics

Samui, S., Subramanian, K., & Srianand, R. 2005, International Cosmic Ray Conference, 9, 215

Schaye, J. 2001, ApJ, 559, 507

Schaye, J., Theuns, T., Rauch, M., Efstathiou, G., & Sargent, W. L. W. 2000, MNRAS, 318, 817

Scheuer, P. A. G. 1965, Nature, 207, 963

Scott, J. E., Kriss, G. A., Brotherton, M., et al. 2004, ApJ, 615, 135

Serra, P., Trager, S. C., Oosterloo, T. A., & Morganti, R. 2008, A&A, 483, 57

Shakura, N. I., & Sunyaev, R. A. 1973, A&A, 24, 337

Shapiro, P. R., Giroux, M. L., & Babul, A. 1994, ApJ, 427, 25

Sharma, P., McCourt, M., Parrish, I. J., & Quataert, E. 2012, MNRAS, 427, 1219

Sharma, P., Roy, A., Nath, B. B., & Shchekinov, Y. 2014, MNRAS, 443, 3463

Sheth, R. K., Mo, H. J., & Tormen, G. 2001, MNRAS, 323, 1

Sheth, R. K., & Tormen, G. 1999, MNRAS, 308, 119

Shull, J. M., Stevans, M., & Danforth, C. W. 2012, ApJ, 752, 162

Shull, M., France, K., Danforth, C., Smith, B., & Tumlinson, J. 2010, arxiv:1008.2957, arXiv:1008.2957

Sironi, L., & Giannios, D. 2014, ApJ, 787, 49

Slosar, A., Hirata, C., Seljak, U., Ho, S., & Padmanabhan, N. 2008, JCAP, 8, 031

Songaila, A., & Cowie, L. L. 2010, ApJ, 721, 1448

Spitzer, Jr., L. 1956, ApJ, 124, 20

Stanway, E. R., Eldridge, J. J., & Becker, G. D. 2016, MNRAS, 456, 485

Stevans, M. L., Shull, J. M., Danforth, C. W., & Tilton, E. M. 2014, ApJ, 794, 75

Stocke, J. T., Keeney, B. A., Danforth, C. W., et al. 2013, ApJ, 763, 148

Strickland, D. K., Heckman, T. M., Weaver, K. A., & Dahlem, M. 2000, AJ, 120, 2965

Suarez, T., & Pontzen, A. 2017, ArXiv e-prints, arXiv:1706.02716

Swartz, D. A., Ghosh, K. K., Tennant, A. F., & Wu, K. 2004, ApJS, 154, 519

Switzer, E. R., Masui, K. W., Bandura, K., et al. 2013, MNRAS, 434, L46

Telfer, R. C., Zheng, W., Kriss, G. A., & Davidsen, A. F. 2002, ApJ, 565, 773

Theuns, T., Bernardi, M., Frieman, J., et al. 2002a, ApJL, 574, L111

Theuns, T., Schaye, J., Zaroubi, S., et al. 2002b, ApJL, 567, L103

Theuns, T., & Zaroubi, S. 2000, MNRAS, 317, 989

Theuns, T., Zaroubi, S., Kim, T.-S., Tzanavaris, P., & Carswell, R. F. 2002c, MNRAS, 332, 367

Thornton, K., Gaudlitz, M., Janka, H.-T., & Steinmetz, M. 1998, ApJ, 500, 95

Trac, H., Cen, R., & Loeb, A. 2008, ApJL, 689, L81

Tüllmann, R., Pietsch, W., Rossa, J., Breitschwerdt, D., & Dettmar, R.-J. 2006, A&A, 448, 43

Tumlinson, J., Peeples, M. S., & Werk, J. K. 2017, Ann. Rev. Astron.& Astrophys. , 55, 389

Tumlinson, J., Thom, C., Werk, J. K., et al. 2011, Science, 334, 948

—. 2013, ApJ, 777, 59

Upton Sanderbeck, P. R., D'Aloisio, A., & McQuinn, M. J. 2016, MNRAS, 460, 1885

Upton Sanderbeck, P. R., McQuinn, M., D'Aloisio, A., & Werk, J. K. 2017, ArXiv e-prints, arXiv:1710.07295

van de Voort, F., & Schaye, J. 2013, MNRAS, 430, 2688

Voit, G. M., & Donahue, M. 2015, ApJL, 799, L1

Voit, G. M., Ma, C. P., Greene, J., et al. 2017a, ArXiv e-prints, arXiv:1708.02189

Voit, G. M., Meece, G., Li, Y., et al. 2017b, ApJ, 845, 80

Wagner, C., Verde, L., & Jimenez, R. 2012, ApJL, 752, L31

Warwick, R. S., & Roberts, T. P. 1998, Astronomische Nachrichten, 319, 59

Werk, J. K., Prochaska, J. X., Tumlinson, J., et al. 2014, ApJ, 792, 8

Werk, J. K., Prochaska, J. X., Cantalupo, S., et al. 2016, ApJ, 833, 54

Wik, D. R., Lehmer, B. D., Hornschemeier, A. E., et al. 2014, ApJ, 797, 79

Wilkins, S. M., Trentham, N., & Hopkins, A. M. 2008, MNRAS, 385, 687

Willott, C. J., Delorme, P., Reylé, C., et al. 2010, AJ, 139, 906

Woods, T. E., & Gilfanov, M. 2013, MNRAS, 432, 1640

—. 2016, MNRAS, 455, 1770

Worseck, G., Prochaska, J. X., Hennawi, J. F., & McQuinn, M. 2014, ArXiv e-prints, arXiv:1405.7405

Worseck, G., Prochaska, J. X., McQuinn, M., et al. 2011, ApJL, 733, L24

Yan, R., & Blanton, M. R. 2012, ApJ, 747, 61

Yoo, J., Fitzpatrick, A. L., & Zaldarriaga, M. 2009, PRD, 80, 083514

Yukita, M., Hornschemeier, A. E., Lehmer, B. D., et al. 2016, ApJ, 824, 107

Zaldarriaga, M. 2002, ApJ, 564, 153

Zaldarriaga, M., Hui, L., & Tegmark, M. 2001, ApJ, 557, 519

Zaroubi, S. 2013, in Astrophysics and Space Science Library, Vol. 396, The First Galaxies, ed. T. Wiklind, B. Mobasher, & V. Bromm, 45

Zel'dovich, Y. B. 1970, A&A, 5, 84

Zhang, Z., Gilfanov, M., & Bogdán, Á. 2012, A&A, 546, A36

Zheng, Z., & Miralda-Escudé, J. 2002, ApJL, 568, L71

VITA

Phoebe Rae Upton Sanderbeck was born on November 1st, 1989 in San Francisco, CA. She graduated with high honors from Brandeis University in 2011 with a Bachelor of Science in physics, minoring in mathematics. She will continue her work as a postdoctoral scholar in the Physics & Astronomy Department at the University of California, Riverside.